AD-A212 049

WRDC-TR-89-4051

KINETIC PROCESSES IN ADVANCED ALLOYS

Dr. K. C. Russell
Professor
Department of Materials Science and Engineering
Department of Nuclear Engineering
Massachusetts Institute of Technology
Cambridge, MA 02139

June 1989

Final Report for the Period 7 September 1986 - 30 September 1987

MATERIALS LABORATORY
WRIGHT RESEARCH AND DEVELOPMENT CENTER
AIR FORCE SYSTEMS COMMAND
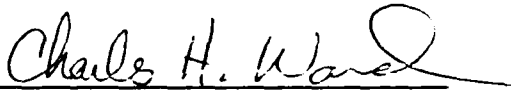WRIGHT-PATTERSON AIR FORCE BASE, OH 45433-6533

DTIC
S ELECTE
SEP 0 7 1989
B D

89 9 06 073

REPORT DOCUMENTATION PAGE	Form Approved OMB No. 0704-0188

1a. REPORT SECURITY CLASSIFICATION UNCLASSIFIED	1b. RESTRICTIVE MARKINGS N/A

2a. SECURITY CLASSIFICATION AUTHORITY N/A	3. DISTRIBUTION/AVAILABILITY OF REPORT
2b. DECLASSIFICATION/DOWNGRADING SCHEDULE N/A	Approved for public release; distribution is unlimited.

4. PERFORMING ORGANIZATION REPORT NUMBER(S)	5. MONITORING ORGANIZATION REPORT NUMBER(S) WRDC-TR-89-4051

6a. NAME OF PERFORMING ORGANIZATION Dept of Matl's Sci & Eng MIT	6b. OFFICE SYMBOL (If applicable)	7a. NAME OF MONITORING ORGANIZATION Materials Laboratory (WRDC/MLLS) Wright Research and Development Center

6c. ADDRESS (City, State, and ZIP Code) Room 13-5066 77 Massachusetts Ave Cambridge MA 02139	7b. ADDRESS (City, State, and ZIP Code) Wright-Patterson AFB OH 45433-6533

8a. NAME OF FUNDING/SPONSORING ORGANIZATION	8b. OFFICE SYMBOL (If applicable)	9. PROCUREMENT INSTRUMENT IDENTIFICATION NUMBER F33601-87-M-3028

8c. ADDRESS (City, State, and ZIP Code)	10. SOURCE OF FUNDING NUMBERS			
	PROGRAM ELEMENT NO.	PROJECT NO.	TASK NO	WORK UNIT ACCESSION NO.
	62102F	2418	02	07

11. TITLE (Include Security Classification)

Kinetic Processes in Advanced Alloys

12. PERSONAL AUTHOR(S)
Russell, Kenneth C.

13a. TYPE OF REPORT Final	13b. TIME COVERED FROM 860907 TO 870930	14. DATE OF REPORT (Year, Month, Day) 890630	15. PAGE COUNT 91

16. SUPPLEMENTARY NOTATION

17. COSATI CODES			18. SUBJECT TERMS (Continue on reverse if necessary and identify by block number)
FIELD	GROUP	SUB-GROUP	Miedema, Titanium, Intermetallic, Rapid Solidification,
11	6	3	Thermodynamics, Dispersoid.
N	6	4	

19. ABSTRACT (Continue on reverse if necessary and identify by block number)

A study was made of kinetic processes in advanced alloys, in particular prediction of terminal solid solubility extension and grain size in rapidly solidified alloys, and dispersoid formation, stability, and interaction with interfaces.

Existing criteria for predicting terminal solid solubility extension were found inadequate. A new criterion based on the Miedema coordinates of electron potential and density was found to have excellent predictive power for Al-based alloys and to show promise for Mg-based and Ti-based alloys.

A simple model was developed which for the first time allows easy prediction of grain size in rapid massive solidification of alloys. The model is in agreement with most existing data on massively solidified RS pure metals and alloys.

Equations are derived for stability of compound dispersoid particles against coarsening and against dragging by grain bounderies. Good agreement was found with experimental

20. DISTRIBUTION/AVAILABILITY OF ABSTRACT ☒ UNCLASSIFIED/UNLIMITED ☐ SAME AS RPT. ☐ DTIC USERS	21. ABSTRACT SECURITY CLASSIFICATION UNCLASSIFIED
22a. NAME OF RESPONSIBLE INDIVIDUAL Lt Charles H. Ward	22b. TELEPHONE (Include Area Code) (513) 255-1307	22c. OFFICE SYMBOL WRDC/MLLS

DD Form 1473, JUN 86	Previous editions are obsolete.	SECURITY CLASSIFICATION OF THIS PAGE

Block 19. (Continued)

measurements on Ti-based alloys and Ti_3Al-based alloys.

In-situ formation of a high number density of fine dispersoid particles is found in large part incompatible with subsequent thermal stability.

Simple expressions derived for thermodynamic quantities needed for calculations in the report will find a wide range of uses.

FOREWORD

This report describes an effort under the auspices of the Structural Metals Branch, Metals and Ceramics Division (MLL) Materials Laboratory, Wright Research and Development Center, Wright-Patterson Air Force Base, OH. Dr. Russell's effort was supported by contract number F 33601-87-M-3028, "Improve Theories for Solid Solubility Extension by Rapid Solidification, for Dispersoid Precipitation and Coarsening, and for Grain Size Prediction After Rapid Solidification."

Research reported was performed in the period 7 September 1986 to 30 September 1987. The report was released by the author in October 1988.

The author acknowledges many helpful discussions with members of the WRDC/MLLS technical staff, and Dr. F.H. Froes in particular for his support of this project.

iii

Accession For	
NTIS GRA&I	☑
DTIC TAB	☐
Unannounced	☐
Justification	

By	
Distribution/	
Availability Codes	
Dist	Avail and/or Special
A-1	

TABLE OF CONTENTS

TABLE OF CONTENTS (Cont'd)

LIST OF ILLUSTRATIONS

LIST OF ILLUSTRATIONS (Cont'd)

LIST OF TABLES

LIST OF SYMBOLS

a	lattice constant
Ap	area of dislocation pipe
b	number of atoms in a molecule
C	composition, usually in mols/m^3
CCT	continuous cooling transformation
D	diffusion coefficient, also diameter of particle or grain
f	volume fraction dispersoid or pores
G	Gibbs free energy, usually per mol
ΔG^*	Gibbs free energy barrier to nucleation
ΔH_{1v}	enthalpy of vacancy formation
ΔH^{trans}	enthalpy to transform nonmetal to metal
HIP	hot isostatically pressed
J	steady state nucleation rate
k	Boltzmann's constant, also partitioning coefficient in solidification
K	coarsening rate constant, also kelvin
L	enthalpy of melting of a solid
n	number of atoms per unit area
n_{ws}	electron density at the Wigner-Seitz boundary
P	a constant
psi	pounds per square inch
Q, Q_5, Q_6	constants
r	particle radius
R	gas constant, hybridization energy
RS	rapidly solidified

$t_{.01}$	time for 1% transformation
T	temperature, either kelvin or fahrenheit
TD	thoria dispersed
TSSE	terminal solid solubility extension
TTT	isothermal transformation
V	volume, also growth velocity
X	composition in atomic fraction
α	a phase, also ratio of diameters, also proportionality sign
β	a phase, also dimensionless velocity
γ	surface energy
Δ	difference
δ	boundary thickness
μ	chemical potential
$\emptyset*$	electron potential
ρ	matter density
ρ_d	dislocation number density
Ω	regular solution constant

Subscripts

A,B	components of solid or liquid
b	refers to boundary
c	continuous cooling reaction
e	equilibrium

Subscripts (Cont'd)

f	formation
I	isothermal reaction
l	liquid or liquidus
m	melting point, matrix, molar
o	reference state
p	particle or pipe
r	reduced, normalized
s	solid, solidus, surface
v	volume or vacancy
x	crystallization, also stoichiometric factor

Superscripts

A	an element
B	an element
e	equilibrium
l	liquid
Nuc	nucleation
r	Value for a particle of radius r
trans	transformation
α	a phase
β	a phase

SECTION I

INTRODUCTION

This report focuses first on the rapid solidification behavior of alloys, then on the formation and behavior of dispersed second phases. The first consideration is to assist in producing alloys which under rapid cooling form a compositionally uniform, fine grained solid. Then, conditions are derived for forming a fine, second phase dispersoid which is stable against coarsening and dragging by migrating grain boundaries. Conditions under which particles or pores will pin a grain boundary are also derived.

Dispersed phases precipitated from the molten alloy are seldom very useful either in strengthening or in limiting grain size in structural materials, as such particles tend to be coarse and heterogeneously distributed. The fine, uniform particle dispersions which may be formed by precipitation from solid solutions are almost always much more beneficial.(1) In addition, many desirable effects may be obtained from solute which is left in solid solution, including increases in strength and modulus, decreased alloy density, and avoidance of undesirable second phases.(2-6) Desirable changes may also be effected in magnetic and electrical properties. The amount of solute which can be retained in solid solution is thus a basic limiting factor in determining a number of important properties of alloys.

There is no unique definition of terminal solid solubility extension (TSSE). A simple, operational definition would define solubility extension as the amount of solute left in solution after the alloy is cooled to room temperature. This solubility is easily determined by lattice parameter measurement. However, such a definition would not include material in solution after solidification is complete, but which precipitated from solid solution during subsequent cooling. A second, conceptually simple but non-operational definition of the extended solubility is the concentration of solute in solid solution the instant that solidification is complete. This solubility depends only on events which take place during melting and solidification. Unfortunately, experimental results are reported in terms of the first definition whereas theoretical analyses use the second.

The importance of TSSE is such that inevitably there have been a number of criteria proposed to predict the conditions of cooling and alloy composition which will give solubility extension. These criteria may be divided into three broad groups: kinetic, thermodynamic, and crystal chemistry. All three criteria involve thermodynamics. It is therefore useful to introduce some of the thermodynamic concepts relevant to TSSE.

Figure 1 shows a simple binary eutectic phase diagram with limited terminal solid solubility and no intermediate phases. Under equilibrium cooling conditions C_α^e is the maximum solute concentration which may be retained in the α phase. One goal of highly nonequilibrium rapid solidification is to defeat this equilibrium limit and retain a greater solute content in solid solution.

1
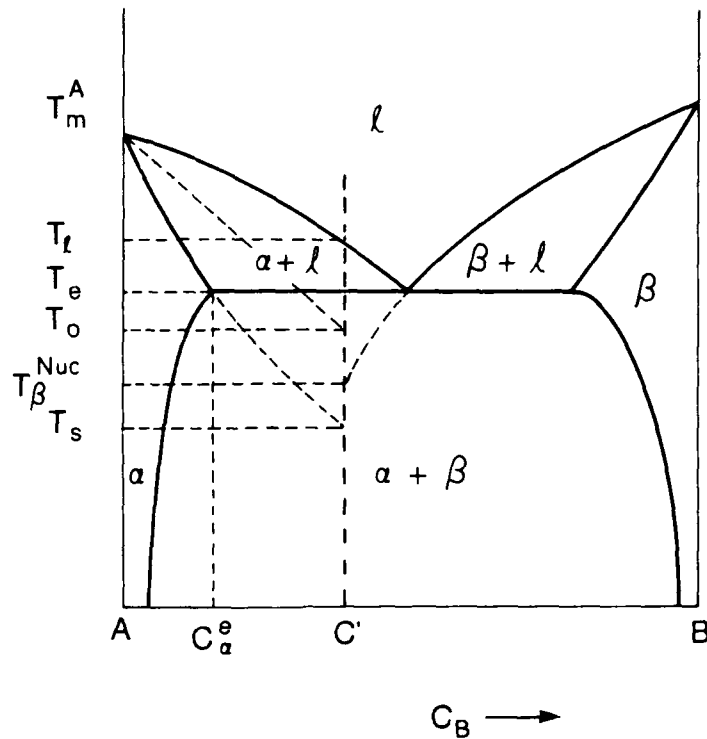
Figure 1   Simple binary eutectic phase diagram showing temperatures relevant to rapid solidification of an alloy of composition C'. See text for definitions of temperatures.

The following temperatures are relevant in solidification of a melt of composition:

$$C' > C_\alpha^e:$$

- T_M^A, the melting point of pure A

- T_l, the liquidus temperature, where the first solid α forms

- T_e, the temperature of the eutectic reaction

- T_0, the temperature at which the free energies of solid and liquid of composition C' are equal. Below T_0, it is thermodynamically possible to have massive solidification, where the solid is uniformly of composition C'.

- T_β^{Nuc}, the temperature where a vertical line at C' intersects the extrapolated β_l liquidus. Below this temperature β phase may form from the liquid .

2

- T_S, the extrapolated α solidus. Although massive solidification of α phase is thermodynamically possible at any temperature below T_0, between T_0 and T_S formation of a mixture of B-poor α and B-rich liquid gives the lowest free energy. Below T_S, α of composition C' has a lower free energy than any combination of α and liquid.

Figure 2 shows schematic free energies corresponding to a simple eutectic phase diagram of the type shown in Figure 1. Figure 2 corresponds to T_l, where the first solid forms from a melt of composition C'. The effect of decreasing temperature may be represented in an approximate way by translating G_l upward with respect to G_α and G_β. The appropriate vertical translation of G_l to give alignment of the intersection of G_l with temperatures shown on the ordinate will give the configurations corresponding to T_l, T_e, T_β^{Nuc} and T_S.
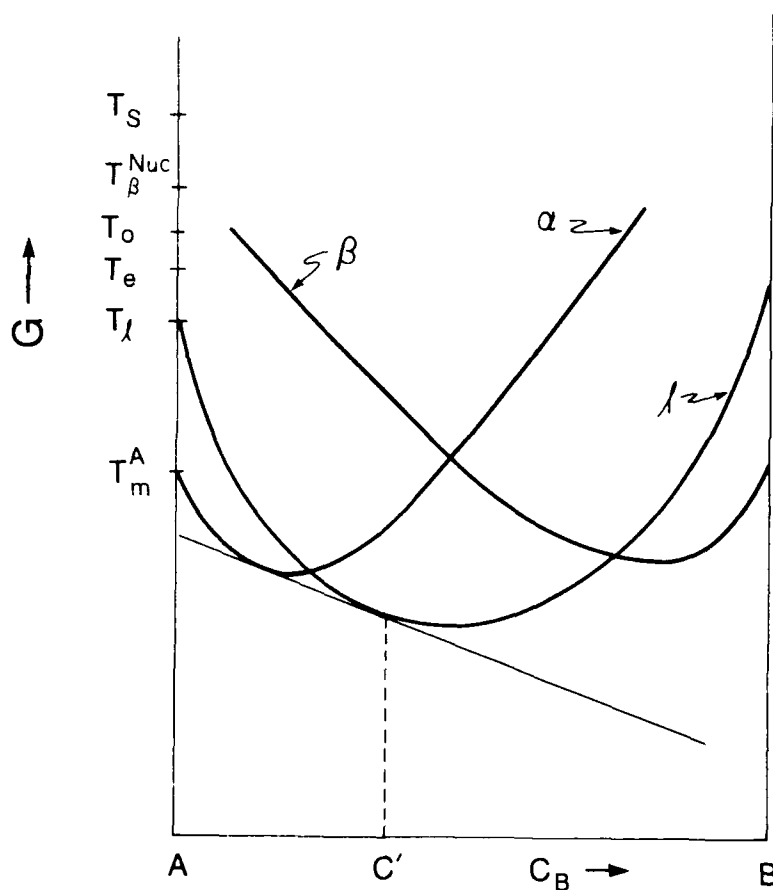
Figure 2   Schematic sketch of free energy of liquid and solid α and β phases which would produce the phase diagram in Figure 1. Shifting G_l upward relative to G_α and G_β corresponds to a lowering of the temperature.

3

At T_l, the tangent to G_l at C' is common to G_α. At T_e, equilibrium between the solid α, liquid, and solid β requires that G_α, G_l, and G_β have a common tangent. At T_o, liquid and α have the same free energy so G_l and G_α intersect at C'. At T_β^{Nuc} it is first possible to nucleate β from liquid, so the tangent to G_l at C' is common to G_β. At T_s, the tangent to G_α at C' is common to G_l, and equilibrium solidification gives α of the same composition as the liquid.

Rapid solidification is often an effective means of producing a fine grained solid. Accordingly, a means of predicting grain size from cooling rate and alloy chemistry is needed. Boswell and Chadwick (7) produced the first theory to predict grain size in rapid solification. They assumed homogeneous nucleation of solid the same compostion of the melt (massive solidification) followed by isotropic crystal growth. This current analysis builds upon their theory to derive an analytical expression for the temperature for the onset of massive solidification in rapid cooling. Improved expressions are derived for the thermodynamic and kinetic quantities involved in nucleation and growth. Finally, an improved method is developed for predicting grain size in rapid solidification.

Modern, high temperature materials are expected to serve at temperatures well over half the absolute melting point, where diffusion in alloys is rapid and nonequilibrium structures tend to quickly relax to near equilibrium. Such common strengthening techniques as cold work, precipitate formation, solid solution additions, and grain size reduction are generally ineffective at such high operating temperatures. Such near equilibrium structures as single crystals or very large grain size materials are often used in such applications. One microstructural modification which is often effective at high temperatures is the introduction of a fine distribution of insoluble dispersoid particles such as carbides, oxides, nitrides, or borides (1,8-11). Equilibrium is thwarted for useful periods of time by the low solubility of the dispersoid in the matrix, which gives vastly slower coarsening rates than would obtain for the phases commonly used in precipitation hardening.

The dispersoid particles are sometimes introduced extrinsically, as by co-comminution of powders of the matrix and dispersoid phases, or by precipitation of the dispersoid on particles of the matrix phase, as is done for thoria-dispersed (TD) nickel. This report focuses on in situ, dispersoid formation in an alloy or intermetallic compound matrix and subsequent dispersoid behavior during processing and service. Coarsening, dragging of particles by the migrating grain boundary, and pinning of the grain boundary by particles or pores are also considered.

Evaluation of the equations derived in this report require knowledge of a range of thermodynamic and kinetic data, much of which is currently unavailable. Expressions are presented herein which allow calculation of these needed ancillary data.

4

SECTION II

THERMODYNAMIC MODELLING

This report models terminal solid solubility extension in rapid solidification, dispersoid formation and stability, and grain size prediction. In each case, modelling requires knowledge of thermodynamic and kinetic parameters which often have not been measured. Free energies of solid and liquid solutions and of intermetallic compounds are required throughout the study. In addition, surface energies and diffusion energies are needed to model nucleation, growth, and coarsening processes.

1. MIEDEMA MACROSCOPIC ATOM MODEL

The models developed in this report require as ancillary data knowledge of phase boundaries and free energies of both stable and metastable phases. Phase boundaries involving only stable phases have in many cases been measured. Determination of metastable phase boundaries, such as extrapolations of the liquidus or solidus curves, must be done on the basis of the free energies of stable and metastable phases. Solid and liquid phase free energy measurements are much less likely to be available than are the associated phase diagrams. Free energies of metastable phases are usually not amenable to measurement; accordingly, determination of such quantitites as T_0, T_β^{Nuc} and T_s (see Figure 1) usually involves modelling of liquid and solid solution thermodynamics.

The ideal thermodynamic model would allow us to calculate accurately the energies from only the properties of the individual atoms. Most solution models fall far short of this ideal. Calculations based on atomic properties alone tend to be highly approximate, and the more accurate models tend to require information on solution energetics which is frequently not available.

This lack of either thermodynamic measurements or an accurate model has for years impeded theoretical studies of such kinetic processes as nucleation, growth, spinodal decomposition, and coarsening, as well as rapid solidification. Fortunately, the "macroscopic atom" model developed over the past decade by Miedema and his co-workers (12-17) comes close to satisfying the stated ideal of an accurate model based on atomic properties only. Miedema's technique gives only the enthalpy; the entropy of the solution or compound may be estimated by one of several techniques to allow calculation of the free energy by the relationship.

$$\Delta G = \Delta H - T\Delta S \qquad (1)$$

Miedema's approach gives mixing enthalpies of binary liquids or enthalpies of formation of binary compounds to an accuracy comparable to that of calorimetry. Mixing enthalpies of solid solutions are obtained to a lower accuracy. However, knowledge of the

5

phase diagram and of the free energy of a coexisting liquid or compound phase allows calculation of the free energy of the solid solution. The model may also be used to calculate surface energies and energies of vacancy formation in liquids and solids.

Figure 3 shows the essentials of Miedema's "macroscopic atom" approach. Elemental A and B are taken to be separated into Wigner-Seitz atomic cells, and then reassembled into the liquid or solid solution or intermetallic compound.
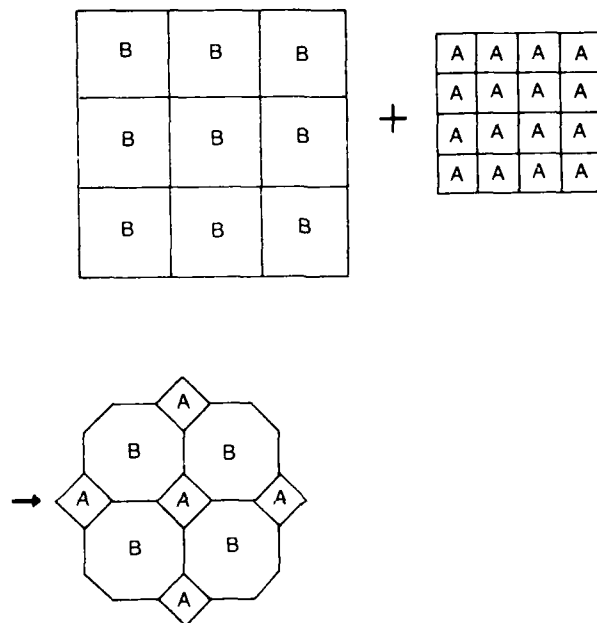
Figure 3   Schematic illustration of Miedema's "macroscopic atom" thermodynamic model. Atoms of elemental A and B are separated at the Wigner-Seitz cell boundary and reassembled into a solid or liquid solution or a compound. The terms in the equation for the enthalpy of mixing are explained in the text.

2. BULK QUANTITIES

In the case of liquid solutions or intermetallic compounds, the enthalpy of mixing is given by

$$\Delta H \alpha - P(\Delta \varnothing^*)^2 + Q(\Delta n_{ws}^{1/3})^2 - R + \Delta H^{trans} \tag{2}$$

where

$\Delta \varnothing^*$ = difference in electron potentials of the elements

6

Δn_{WS} = difference between electron densities of the elements at the Wigner-Seitz cell boundary.

The first two terms contribute to the enthalpy in all cases. Unequal electron densities at the Wigner-Seitz boundary (n_{WS}) must be evened out, which gives a positive contribution to the enthalpy, and unequal electron potentials ($\emptyset^*$) cause charge transfer and a negative enthalpy contribution. The constant R is due to the electron hybridization which occurs when d-valence electrons of transition metals hybridize with s or p valence electrons of polyvalent nontransition elements. R is the order of 1eV/atom (100 kJ/mol) for such alloys, depending somewhat on which nontransition element is involved, and is zero in all other cases. The substantial negative contribution of R to the enthalpy of alloy or compound formation explains why transition metals have a strong tendency to form compounds with such polyvalent nontransition elements as boron, carbon, and nitrogen, while many other metals do not.

The calculation applies only for metallic elements; ΔH^{trans} is the enthalpy required to transform a nonmetallic component (e.g. silicon) into a hypothetical metallic state. The values of $\emptyset^*$ may be adjusted slightly to fit the measured heats of mixing, but n_{WS} is a basic, measurable quantum mechanical quantity. The constants P, Q, and R depend on which groups in the periodic table the alloying elements are from; the ratio P/Q is the same for all solutions and compounds.

Miedema has tabulated enthalpies of mixing for virtually all binary liquids involving metals and for a range of compounds of metals with metals, semimetals, and nonmetals.(12,13) Eq. (2) may be multiplied by an appropriate function of composition to give an equation for enthalpy of mixing vs composition. Miedema has in fact revolutionized the thermodynamic modelling of solutions and compounds involving metals. His results are invaluable in predicting TSSE by RS, as they are in a variety of other fields.

Figure 4 plots $\emptyset^*$ and $n_{WS}^{1/3}$ for most metals and a number of semimetals and nonmetals. Miedema's approach is limited to metals, so the $\emptyset^*$ and n_{WS} for semimetals and nonmetals are for the element in the thermodynamically unstable metallic state. The (positive) enthalpy needed to transform the element from the metallic state must then be added to the enthalpy of mixing. These values are shown in Figure 4. Divalent elemental Eu and Yb are often trivalent in alloys; the appropriate enthalpy of transformation must then be added to the calculated enthalpies of mixing.

The Miedema plot has the following significance for liquid solutions and compounds which do not involve d-electron hybridization or nonmetals.

- Elements lying very near one another will have very similar alloying and compound forming characteristics and near-zero enthalpies of mixing or for compound formation with one another.

7
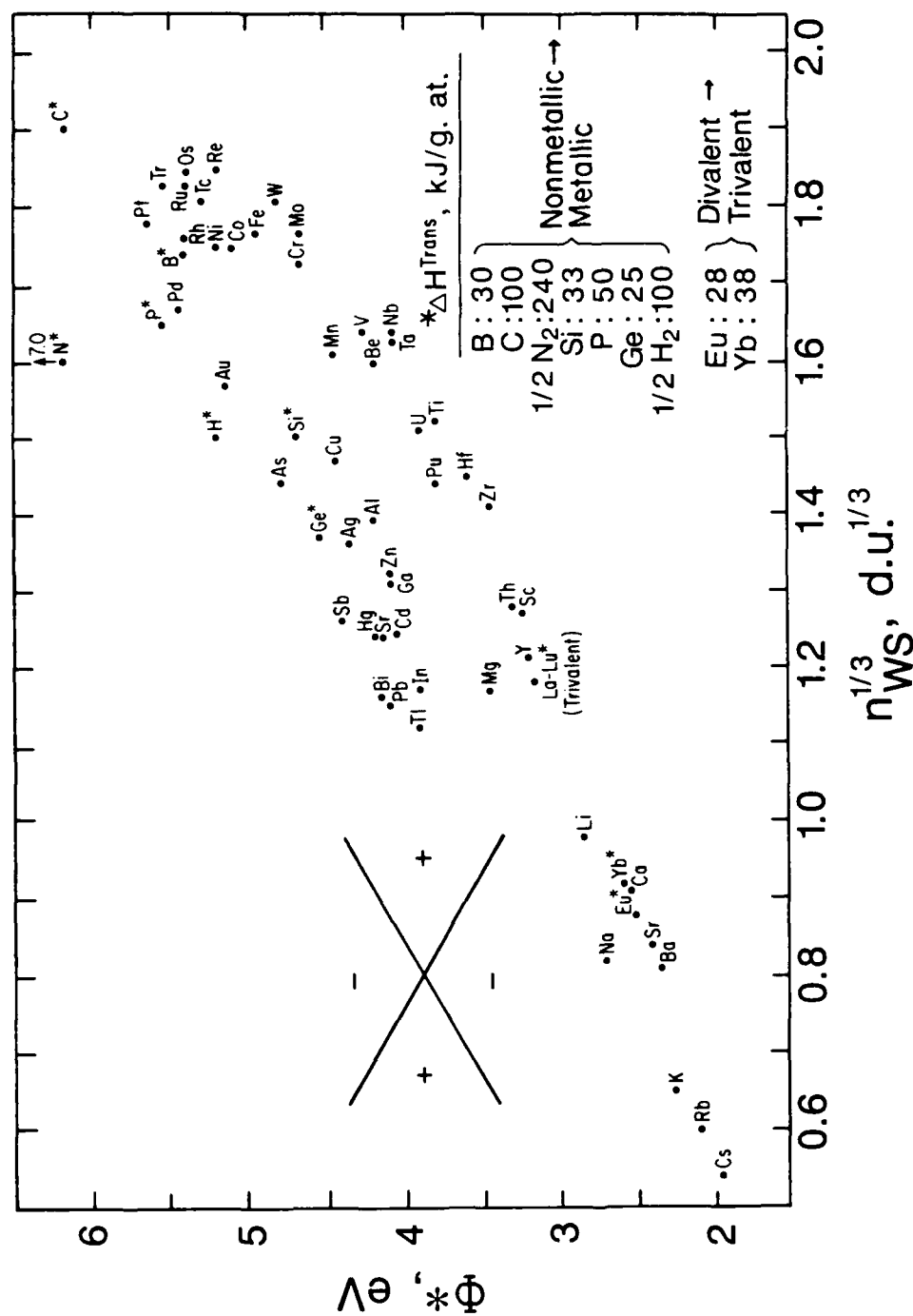
Figure 4   Miedema plot of electron potential vs electron density at the Wigner-Seitz cell boundary. The figure completely characterizes the thermodynamic interaction of binary liquid alloys except for those which involve nonmetals or combinations of transition metals and polyvalent, nontransition metals. Pairs of metals connected by lines of the slope shown will have a near-zero enthalpy of mixing and will form near-ideal liquid solutions and will not form compounds. (After Miedema, et al, (12)).

- Elements which may be connected by lines of the slopes shown at the left side of the plot will have small enthalpies of mixing and form near ideal solutions with complete liquid-phase miscibility.

- Alloys of elements with large horizontal separations will have large positive enthalpies of mixing and tend toward phase separation in both the liquid and solid states.

- Alloys of elements with large vertical separations will have large negative enthalpies of mixing and tend to form compounds.

The hybridization which occurs in alloys of transition metals and polyvalent non-transition metals will tend to make the mixing enthalpies more negative and favor more compound formation.

The Miedema plot is an extremely powerful tool in that it gives a two parameter plot ($\emptyset^*$ and $n_{ws}^{1/3}$) characterizing the alloying behavior of the various elements. That the plot becomes more complicated and must be used with a bit more care in alloys involving electron hybridization or nonmetals is a modest price to pay for the power of this global technique.

3. SOLID SOLUTIONS

Miedema calculated enthalpies of liquid solutions and compounds to the accuracy of calorimetry but was significantly less successful with solid solutions due to difficulty in estimating strain energy. Fortunately the free energy of mixing of a solid solution may be obtained from phase diagram information and the thermodynamics of a coexisting phase for which the free energy has been measured or can be calculated, typically a liquid or intermetallic compound. Figure 5 shows the case for equilibrium between a line compound of free energy ΔG_c, and a solid solution α, of free energy ΔG_α. The co-existing compositions are X_c and X_e, respectively. Assuming the regular solution model (18) for simplicity:

$$\Delta G_\alpha = \Omega_\alpha X(1-X) + RT[X \ln X + (1-X)\ln(1-X)] \qquad (3)$$

where the regular solution coefficient, Ω_α, is also the partial molar enthalpy of mixing of B in A. The standard states are pure, solid A and B. The regular solution model has known shortcomings, but is usually adequate for relatively dilute α, say $X \lesssim 1$. ΔG_c may be obtained from Miedema's calculated enthalpies by adding a term for entropy of compound formation.

9
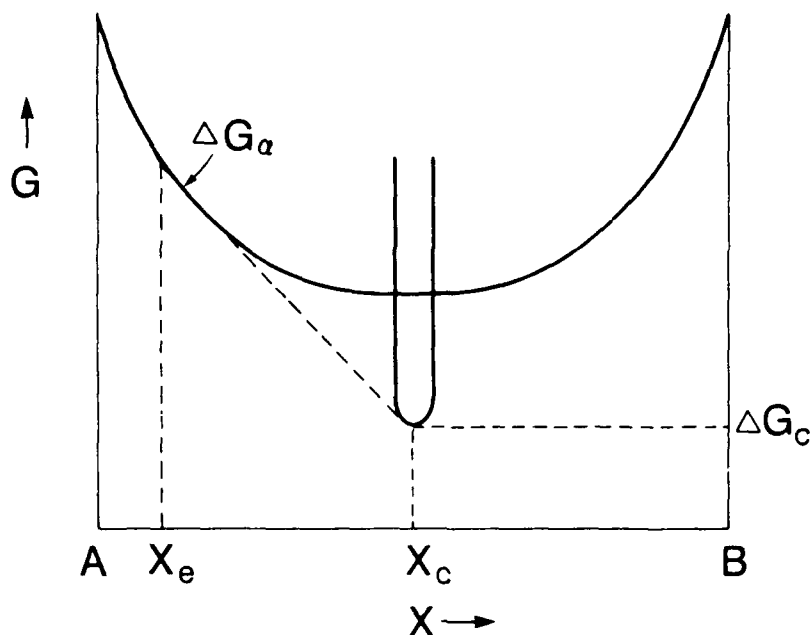
Figure 5   Schematic figure showing equilibrium between a solid solution, α, and a compound, C. The regular solution coefficient, Ω_α, may be obtained from G_c and the coexisting compositions X_e and X_c.

Equilibrium requires a common tangent to ΔG_c at X_c and ΔG_α at X_e. Then:

$$\Omega_\alpha = \Delta G_c - RT[X_c \ln X_e + (1-X_c)\ln(1-X_e)][X_e^2 - 2X_c X_e + X_c]^{-1} \qquad (4)$$

or for the case of dilute α:

$$\Omega_\alpha = \Delta G_c / X_c - RT\ln X_e \qquad (5)$$

The thermodynamic properties of solid α may thus be calculated in terms of quantities which may easily be measured or calculated.

The second case, that of α of compositon X_e in equilibrium with a liquid of composition X_l is shown in Figure 6. ΔG_l is assumed to be known, at least in the vicinity of X_e, either from measurement or from calculation.

We again assume a regular solution and take pure solid A and B as the standard states. Then we may write for liquid and solid:

10
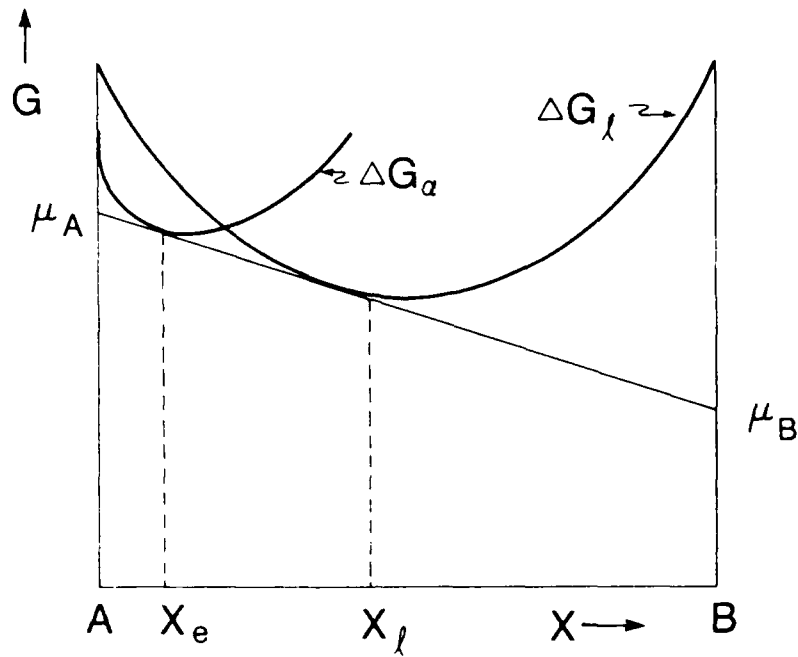
Figure 6   Schematic figure showing equilibrium between a liquid and a solid.
The regular solution constant, of α, Ω_α , may be obtained from G_l
and the coexisting compositions X_α and X_l.

$$\mu_B^l = \Omega_l \, (1\text{-}X_l)^2 + RT \, \ln X_l + \Delta\mu_B^o \tag{6a}$$

$$\mu_B^\alpha = \Omega_\alpha (1\text{-}X_\alpha)^2 + RT \, \ln X_\alpha \tag{6b}$$

where

$$\Delta\mu_B^o = L_B \, (T_m^B\text{-}T)/T_m^B \tag{7}$$

and L_B ($>O$) is the heat of fusion of B and T_m^B is the melting point of B. Equating the
chemical potential of B in coexisting liquid and α phases and assuming dilute solutions
gives:

$$\Omega_\alpha = \Omega_l + \Delta\mu_B^o + RT \, \ln(X_l / X_\alpha) \tag{8}$$

11

Now Ω_α may be calculated easily from Ω_l (obtained from Miedema's formulation), the partitioning coefficient, $k = C_\alpha/C_l$, and the melting temperature and enthalpy of fusion of pure B. Eq. (8) leads to the surprising conclusion that for Ω_α to be temperature independent for dilute, regular solutions, k must be a function of temperature.

The technique just described, combined with phase diagram information which is usually available and Miedema's calculation of enthalpies of liquids and compounds can provide a fairly complete picture of the thermodynamics of any phase of interest.

4. UNDERCOOLED MELTS

This section derives equations for T_0, the temperature at which solid and supercooled liquid of the same composition have the same free energy, and for ΔG_v, the driving force for massive solidification. A regular solution model is assumed for convenience. In addition, the heat capacity of the solid and liquid alloy is assumed to be the same as that of the equivalent amounts of elemental melts. The calculation could readily be extended to a more complex solution model.

We consider one mol of alloy, with atomic fractions of A and B of X_A and X_B, respectively. Calculations are based on the cycle shown in Figure 7. The free energy change for cooling and solidifying the alloy (Step 4) is equal to the sum of the changes of Steps 1 through 3.

The free energy change for un-mixing in Step 1 is

$$\Delta G_1 = -\Omega_l X_A X_B - RT(X_A \ln X_A + X_B \ln X_B)$$
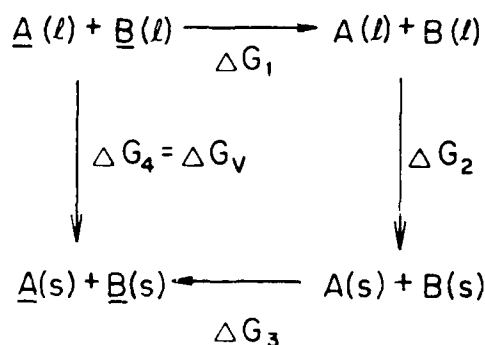
Figure 7   Cycle used for calculating T_0 for a molten alloy.

In the second step, pure A and B solidify.

$$\Delta G_2 = -X_A L_A \Delta T_A - X_B L_B \Delta T_B$$

where L_A, L_B are the (positive) heats of fusion,

$$\Delta T_A = (T_M^A - T)/T_M^A$$

$$\Delta T_B = (T_M^B - T)/T_M^B$$

T_M^A and T_M^B are the melting points of A and B, respectively. In the third step, the solid elements are combined to form the α solid solution.

$$\Delta G_3 = \Omega_\alpha X_A X_B + RT(X_A \ln X_A + X_B \ln X_B)$$

We then take $\Delta G_v = \Delta G_4 = \Delta G_1 + \Delta G_2 + \Delta G_3$ to obtain:

$$\Delta G_v = (\Omega_\alpha - \Omega_l) X_A X_B - X_B L_B \Delta T_B - X_A L_A \Delta T_A \tag{9}$$

The mixing entropy terms have cancelled

At T_0, the highest temperature at which massive solidification may occur, $\Delta G_4 = 0$, and

$$T_0 = [(\Omega_l - \Omega_\alpha)X_A X_B + X_A L_A + X_B L_B] (X_A L_A/T_M^A + X_B L_B/T_M^B)^{-1} \tag{10}$$

The ratio of heat of fusion to absolute melting point is approximately constant for most metals, being about 10J/mol·K. In that case, Eq. (10) may be simplified to give:

$$T_0 = T_M^A X_A + T_M^B X_B - T_M^A (\Omega_\alpha - \Omega_l) X_A X_B/L_A \tag{10a}$$

A low T_0 for a given solvent is thus favored by a large value of $(\Omega_\alpha - \Omega_l)$ and by a low melting solute. We may obtain a simple expression for a ΔG_v as a function of the supercooling below T_0.

$$\Delta G_v = \Delta H_v(T_0 - T)/T_0$$

Taking $\Delta H_v = (\Omega_l - \Omega_\alpha) X_A X_B + X_A L_A + X_B L_B$ and substituting Eq. (10a) for T_0 in the denominator, we find,

$$\Delta G_v = (X_A L_A/T_M^A + X_B L_B /T_M^B)(T-T_0) \tag{11}$$

Eqs. (10,11) provide remarkably simple expressions for T_0 and ΔG_v. Only the properties of the elements and the supercooling below T_0 are involved.

We now consider the factors which govern T_0 and ΔG_v. In the case of an ideal solution, $\Omega_l = \Omega_\alpha = 0$, and T_0 is the composition weighted average of the melting points of elemental A and B. Deviations from this simple condition are produced by $\Omega_l - \Omega_\alpha \neq O$. Having $\Omega_\alpha \gg \Omega_l$ sharply depresses T_0. The reason, of course, is that $\Omega_\alpha \gg \Omega_l$ implies that the alloy is more stable as a liquid than as a solid: T_0 is therefore depressed.

Examination of Eq (11) for ΔG_v shows that the properties of the liquid and solid alloys enter only implicitly, through T_0. As noted earlier, L/T_m is approximately a constant for all metallic elements, so that:

$$\Delta G_v = L_A \, (T-T_0)/T_M^A \tag{12}$$

Such metalloids as Si and Ge are likely to have values of L/T_m different from that characteristic of metals. For metal-metalloid alloys the longer expressions for T_0 and ΔG_v must therefore be used, (Eqs (9,10)).

The solidification behavior of alloys of metals and metalloids (e.g., Al-Si and Al-Ge) is of considerable interest. In that the expressions derived earlier, apply to metal-metal solutions, we here derive expressions for T'_m and L' for metalloids in the fictitious metallic state. The prime is used to denote quantities calculated for the metallic state.

Let us take Si as an example and indicate the metallic, nonmetallic and liquid phases by Si(m), Si(nm) and Si(l), respectively. All three phases are for simplicity assumed to have the same heat capacity.

The transformation Si(l) $\rightarrow$ Si(m) may be accomplished by the steps: Si(l) $\rightarrow$ Si(nm) $\rightarrow$ Si(m). Enthalpy is a state function, so

$$L'_{Si} = L_{Si} - \Delta H^{trans}$$

where ΔH^{trans} is the enthalpy for the transformation Si(nm) $\rightarrow$ Si(m). Miedema has calculated ΔH^{trans} for Si, Ge, and other non-metallic elements. In that Si (nm) is the stable solid phase, L'_{Si}: is considerably less than L_{Si}

We may calculate T'_m from the following processes:

1. Si (l) $\rightarrow$ Si (nm) at T'_m: $\Delta G_1 = L_{Si}(T'_m - T_m)/T_m$

2. Si (nm) $\rightarrow$ Si (m) at T'_m: $\Delta G_2 = \Delta H^{trans}$

3. Si (m) $\rightarrow$ Si(l) at T'_m: $\Delta G_3 = 0$

Since the three steps form a complete cycle and $\Delta G_1 + G_2 + G_3 = 0$

$$T'_m = T_m (1 - \Delta H^{trans}/L_{Si}) \qquad (13)$$

Eq. (13) shows that the melting point of the metastable metallic element is depressed below that of the stable non-metal by an amount proportional to $\Delta H^{trans}/L$. When the ratio of enthalpies is unity, the solid metal would be stable against melting only at absolute zero. Eq. (13) allows us to use Eqs. (9,10) to calculate T_0 and ΔG_v for solidification of metal-metalloid solutions. The regular solution constants may be calculated by the method of Miedema taking the metalloid to be in the fictitious metallic state.

Manipulation of Eq. (13) gives :

$$L'/T'_m = L/T_m \qquad (14)$$

The ratio of enthalpy of melting to melting point is thus the same for metallic and non-metallic forms of the element. This ratio is usually different for metals and nonmetals. So we should not take the ratio L'/T'_m as equal to that for normal metals. Accordingly, the long equations (9,10) must be used in calculating T_0 and ΔG_v for metal-metalloid melts.

5. SURFACE ENERGIES

Energies of interfaces involving only fluid phases are readily measured to a high degree of accuracy. Measurement of energies of interfaces involving solid phases is difficult and often inexact. A theoretical model for the energies of such interfaces is highly desirable.

Surface energy is the work needed to expand surface area and as such is inherently related to interatomic forces. Consequently, such material parameters as the heat of fusion or evaporation, hardness, elastic modulus, and melting temperature provide a rough guage of the surface energy (19,20).

Even though there is no perfect model, several theoretical approaches have been introduced for the calculation of the solid-vacuum (21-25), liquid-vacuum (26,27) solid-liquid, (28-34), and solid-solid (32) interfacial energies. In some cases theoretical values of surface energies show good agreement with experimental values. However, almost all the models deal with pure metal systems. So far, only a few models have been presented for liquid metal-compound systems. In this section, the models of Miedema and Warren are reviewed briefly.

The "macroscopic atom" model developed over the past decade by Miedema and his coworkers (26,32) and described in Section II.1 provided for the first time an accurate energetic model based on atomic properties only which may be used to calculate surface energies.

The liquid-vacuum surface energy γ_1, is sometimes taken as proportional to the enthalpy of vaporization of the liquid, ΔH_{vap}. Indeed, a roughly linear relationship exists

15

between γ_1 and ΔH_{vap}. Miedema noted, however, that ΔH_{vap} depends in part on the properties of the free atoms in the gasous state. Certain gaseous atoms, in particular Hg, have very stable electron configurations which lead to anomalously low ΔH_{vap}. Atoms at the liquid-vacuum interface do not have this low energy electron configuration, so the proportionality between ΔH_{vap} and γ_1 is destroyed. The value of n_{ws} is a much more accurate measure of the degree of disruption of the electron gas on creating a surface. Miedema found significantly better proportionality between γ_1 and n_{ws} than with ΔH_{vap}. Surface energies of the divalent metals (such as Hg) with anomalous heats of vaporization are no longer exceptions.

Subsequently, Miedema showed that there was little difference between solid-vacuum and liquid-vacuum surface energies, and that in fact $\gamma_s/\gamma_1 = 1.13$ for all pure metals. He refined his surface energy model to better account for the number of valence electrons per atom to obtain:

$$\gamma_s = \text{const } n_{ws}^{5/3} / (\emptyset^* - 0.6\text{eV})^2 \tag{15}$$

Eq. (15) may then be used with confidence to obtain γ_s or γ_1 for any metallic element.

Miedema and den Broeder calculated solid-liquid surface energies for one and two component metallic systems. The calculation is predictably more complex than it was for liquid-vapor and solid-vacuum surface energies. For a one component system, the atoms in the first atomic layer in contact with the melt are increased in enthalpy by a fixed fraction of the enthalpies of fusion so that

$$\gamma_{sl}^{I} = 2.5 \times 10^{-9} \, L/V^{2/3} \tag{16}$$

where V is the molar atomic volume of the solid. To this is added an entropic term, S^*, due to the added disorder in the surface layer:

$$\gamma_{sl}^{II} = S^* \, T_m/V^{2/3} \tag{17}$$

where $S^* = 0.52 \times 10^{-7}$ J/K.

Then

$$\gamma_{sl} = \gamma_{sl}^{I} + \gamma_{sl}^{II} \tag{18}$$

Somewhat surprisingly, the Miedema and den Broeder values for γ_{sl} fit the empirical Skapski (22) relation:

$$\gamma_{sl} = \gamma_s - \gamma_1 \tag{19}$$

fairly accurately.

Using Miedema's values for γ_s and γ_l,

$$\gamma_{sl} = 0.13 \ \gamma_s. \tag{20}$$

For binary interfaces of solid metal A against liquid metal B,

$$\gamma_{sl}{}^{AB} = (\gamma_{sl}{}^I)_B + (\gamma_{sl}{}^{II})_B + \gamma_{sl}{}^{III} \tag{21}$$

where $\gamma_{sl}{}^I$ and $\gamma_{sl}{}^{II}$ are given by Eqs. (16) and (17), respectively. The enthalpy term $(\gamma_{sl}{}^I)$ is for the solid A and the enthalpy term $(\gamma_{sl}{}^{II})$ is for liquid B. To these two terms is added a chemical term due to interactions between A and B atoms:

$$\gamma_{sl}{}^{III} = 2.5 \times 10^{-9} \ \Delta H/V \tag{22}$$

where ΔH is the heat of solution of A in B or of B in A in the liquid phase. Since $\Delta H_A/V_A$ and $\Delta H_B/V_B$ are slightly different, an averaged value is used. The heat of solution may be easily calculated by Eq. (2).

Miedema's model for γ_{sl} is easily extended to the case of massive solidification of alloys.

$$\gamma_{sl}{}^I = 2.5 \times 10^{-9} \ [L_A X_A/V_A{}^{2/3} + L_B X_B/V_B{}^{2/3}] \tag{23}$$

Then:

$$\gamma_{sl}{}^{II} = S* \left[\frac{T_m^A X_A}{V_A^{2/3}} + \frac{T_m^B X_B}{V_B^{2/3}} \right] \tag{24}$$

and

$$\gamma_{sl}{}^{III} = 0.$$

In Warren's treatment (33), a thermodynamic model of the solid-liquid metallic interface in a binary system is extended to a pseudo-binary system which is composed of a metallic liquid and a stable solid carbide or oxide phase. This model assumes that a finite value of the interfacial energy exists because a region in the neighborhood of the interface is disturbed from the bulk equilibrium states of both solid and liquid. Disturbances in the chemical composition and structure are treated as separate contribution.

The chemical contribution of the interface atoms to the interfacial energy is taken to be the difference between equilibrium molar free energy, G_5 in Figure 8, of the atoms in an equilibrium two-phase mixture without an interface, and G_6, their energy when forced exist together as a liquid of composition X' in a two atomic layer interface. Then the chemical contribuion to the interfacial energy per unit area, $\gamma_{sl(c)}$, becomes

$$\gamma_{sl(c)} = n \, (G_6 - G_5) / N \qquad (25)$$

where N is Avogadro's number and n is the number of interface atoms per unit area, which is equal to the sum of the solid molecules and liquid atoms at the interface, $n_s + n_l$. For simplicity and as a rough approximation, the disturbed region is considered to extend over only two atomic layers. Assuming a simple cubic arrangement of atoms, then
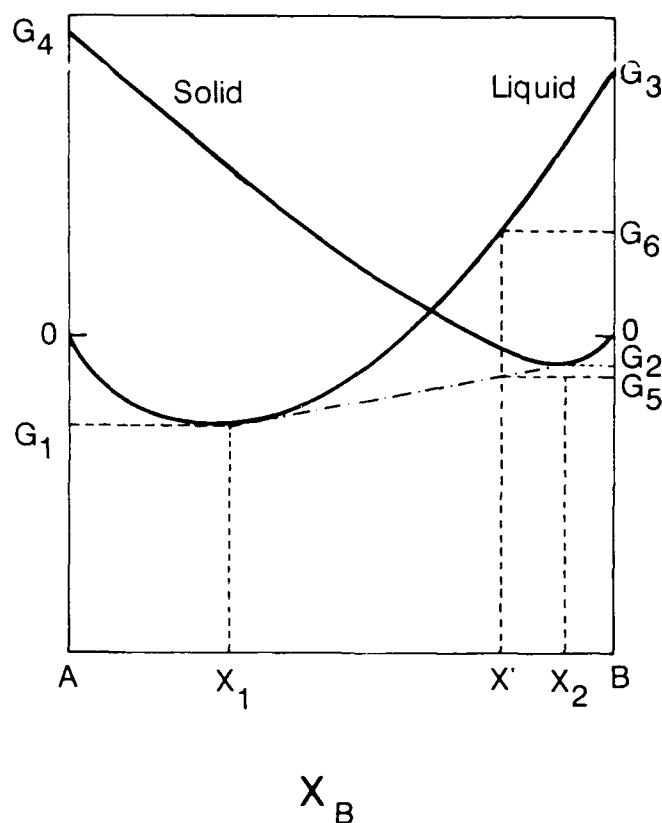
Figure 8   Free energy vs composition for the pseudobinary A-B, where A is a metal and B is a compound.

$$n_s = (N/V_s)^{2/3} \qquad (26)$$

where V_s is the effective molar volume of atoms in the solid. The effective molar volume V_s, is given by

$$V_s = X_2 V_B b^{1/2} + (1 - X_2) V_A \qquad (27)$$

18

where V_B is the molar volume of the compound B, b is the number of atoms in the molecules, and V_A is the molar volume of liquid A. Similarly,

$$n_1 = (N/V_1)^{2/3} \qquad (28)$$

where V_1 is the average molar volume of atoms in liquid and given by

$$V_1 = X_1 V_B b^{1/2} + (1 - X_1) V_A \qquad (29)$$

If the solubility of B in A is low, then G_5 approaches zero, giving

$$\gamma_{sl(c)} = nG_6/N \qquad (30)$$

with

$$G_6 = G_3 (X')^2 + RT [X' \ln X' + (1-X') \ln(1-X')] - RT [X' (1-X')] \ln X_1 \qquad (31)$$

where G_3 is the free energy of fusion of the solid B and to a good approximation can be written as

$$G_3 = L_B (T_m^B - T)/T_m^B \qquad (32)$$

where L_B is the latent heat of fusion and T_m^B is the melting temperature of B. When measured values are not available, the heat of fusion for cubic ionic solids can be estimated from the following empirical relationship:

$$L_B = 25T_m^B \qquad (33)$$

where L_B is in J/mol, and T_m^B in K. The interface composition is given by

$$X' = (n_1 X_1 + n_s X_2)/(n_1 + n_s) \qquad (34)$$

Eq. (34) shows that X' is relatively insensitive to changes in X_1; therefore, $\gamma_{sl(c)}$ is directly proportional to $- \ln X_1$.

The structural contribution to γ_{sl} can be calculated from the empirical relationship:

$$\gamma_{sl(B)} = kT_M^B /b(V_B/b)^{2/3} \qquad (35)$$

where k is an empirical constant and lies between 5×10^{-4} and 8×10^{-4}, when $\gamma_{sl(B)}$ is given in J/m^2.

When adequate thermodynamic data are not available for the systems of interest, they may be calculated by the methods in Section II.

6. DIFFUSION IN LIQUIDS

Diffusion coefficients in pure liquid metals are usually the order of 10^{-9} m^2/s at the melting point. Diffusivities in molten supercooled alloys must be much lower, or rapid quenching could not give either massive solidification or glass formation. In that massive solidification which usually takes place at temperatures far below the liquidus, calculation of nucleation and growth rates requires accurate values of the diffusion coefficient in highly supercooled liquid.

Faber (35) has noted that the enthalpy of vacancy migration in liquids is zero. Atomic motion thus requires only creation of a hole, or vacancy large enough for a neighboring atom to fit into.

Miedema found a remarkably good correlation between crystallization temperature of metallic glasses and the enthalpy to form a hole the size of the smaller atom in the liquid. Massive solidification is somewhat intermediate between equilibrium solidification and crystallization of glasses; it is thus reasonable to take the atomic mobilities governed by the enthalpy of forming a vacancy the size of the smaller atom.

Volume changes on mixing liquid metals are generally small -- the order of a few percent, at most. Accordingly, partial atomic volumes in the molten alloy will be very nearly equal to the atomic volumes in the respective molten elements.

Following is an outline of the Miedema calculation for vacancy formation in alloys, ΔH_{1v}. Interestingly, ΔH_{1v} is the same for solids and liquids, excluding volume effects. The greater atomic mobilities in liquids are then due to the zero enthalpy of vacancy migration.

Miedema (14,15) gives for the enthalpy of monovacancy formation,

$$\Delta H_{1v} = V_m^{2/3}\, \gamma_s / Q_5 \tag{36}$$

where

V_m = molar volume

γ_s = energy of solid:vacuum interface

$Q_5 = 8.5 \times 10^{-9}$ for nontransition metals

$Q_5 = 7 \times 10^{-9}$ for transition metals.

The enthalpy of vacancy formation in alloys is a weighted average of the values for the elements (14). For a vacancy the size of the B atom,

$$\Delta H_{1v} = C_S^B\, \Delta H_{1v}^B + (1 - C_S^B)\, \left(\frac{V_B}{V_A}\right)^{5/6} \Delta H_{1v}^A \tag{37}$$

where C_S^B is the surface concentration of B around the hole:

$$C_S^B = \frac{C_B V_B^{2/3}}{C_A V_A^{2/3} + C_B V_B^{2/3}}$$

No distinction is made between vacancy formation in liquids and solids. A random solution is assumed, though a similar calculation of ΔH_{1v} may be performed for intermetallic compounds.

It is now possible to calculate the enthalpy of vacancy formation, hence of diffusion, for any liquid alloy. If we take $D_0 = 10^{-4}$ m2/s, the values of D_l for elemental metals at the melting point are approximately an order of magnitude greater than the 10^{-9} m2/s usually measured. It is thus reasonable to take $D_0 \approx 10^{-5}$ m2/s. In any event, D_0 should be about the same for all elements and any uncertainty would cancel out in comparisons of grain size or temperature of crystallization.

7. OTHER ANCILLARY DATA

Mass transport in solids is by diffusion, which may occur either in the matrix, along dislocation lines, or in grain boundaries. Diffusion coefficients have been measured for many solid solution alloys of interest (36). Brown and Ashby (37) present correlations based on crystal structure for activation energies for matrix diffusion which are useful when data are not available.

Fewer measurements have been made of diffusion coefficients in dislocations and interfaces. Where measured values are not available, it is reasonable to estimate the activation energy for diffusion of substitutional solute along dislocations or grain boundaries as about half that for volume diffusion and take the preexponential factor, D_0 as 10^{-4} m2/s (1 cm2/s).

Grain boundaries contain regions of disorder which may accommodate atoms which do not fit well into lattice sites. Atoms which are not very soluble in the matrix thus tend to be strongly absorbed at the boundary. Hondros (38) showed that bulk (C) and boundary (C_b) concentrations are related approximately by

$$C_b/C = 1/X_e \tag{38}$$

where X_e = solubility limit of the element in the matrix, in atomic fraction, at the temperature of interest. Very sparingly soluble elements will thus absorb very strongly at grain boundaries. Similarly, elements with a large matrix solubility will not be strongly adsorbed at the grain boundary.

The reader is referred to <u>Smithell's Metals Reference Book</u> (39) for densities and viscosities of molten metals, to the <u>Handbook of Chemistry and Physics</u> (40) for enthalpies of melting, to Niessen, et al (13) for tables of $\emptyset^*$, $n_{ws}^{1/3}$, ΔH^{trans}, and enthalpies of mixing

and compound formation. Enthalphies of vacancy formation are given by Miedema (15) and values for γ_{sl} are given by Miedema and den Broeder (32). The American Institute of Physics Handbook (41) is a valuable source of physical data.

SECTION III

TERMINAL SOLID SOLUBILITY EXTENSION

A number of criteria have been proposed to predict whether or not TSSE will occur for a given combination of alloy chemistry and cooling rate. Figures 1 and 2 show the phase diagram information and free energies relevant to TSSE.

1. THERMODYNAMIC CRITERIA

Above T_0, the temperature at which solid and liquid of the same composition have the same free energy, massive solidification cannot occur. Formation of solid of the same composition as the liquid would give an increase in free energy and is therefore thermodynamically impossible. Below T_S, the extrapolated solidus, massive solidification leads to the minimum free energy state of the alloy. Solidification to form a two-phase mixture gives a free energy between that of the supersaturated liquid and that of the massively solidified phase. In addition to having a higher free energy than the massively solidified phase, the two-phase mixture requires long range diffusion in the liquid to form. Thus, although not forbidden, formation of a two-phase mixture below T_S is at both a thermodynamic and kinetic disadvantage and seems unlikely.

Between T_0 and T_S, massive solidification is thermodynamically possible, but results in a higher free energy than does formation of the equilibrium two-phase mixture. However, massive solidification occurs without long range diffusion, which is required for equilibrium solidification. Thus, in the temperature region $T_S<T<T_0$, massive solidification has a kinetic advantage and thermodynamic disadvantage vis-à-vis two-phase equilibrium solidification.

One strong argument against massive solidification above T_S is that it violates local equilibrium, one of the most valued principles of the materials scientist. Local equilibrium requires each component to have the same chemical potential in the liquid as in the solid. Between T_0 and T_S, equilibirum requires that solid and liquid have different compositions, as given by the phase diagram.

However, Baker and Cahn (42) showed that local equilibrium at the interface does not always apply during solidification. Zinc-rich Zn-Cd alloys have a retrograde solidus, i.e. the concentration of Cd in solid in equilibrium with Zn-rich alloys reaches a maximum above the eutectic temperature and then decreases with decreasing temperature. This behavior is in sharp contrast to that shown in Figure 1, where the solidus concentration increases with decreasing temperature.

Baker and Cahn rapidly quenched Zn-Cd alloys of Cd contents greater than the maximum in the soliudus and obtained a single phase solid solution. Because of the retrograde solidus, massive solidification must have taken place in the two-phase region

where local equilibrium could not be attained. The Cd atoms underwent an increase in chemical potential during solidification as they were dragged into the solid phase by the Zn.

Local equilibrium has been observed to apply in many solificiation experiments. It is thus not clear whether the Baker-Cahn result is an anomaly, or whether rapid solidification will frequently violate local equilibrium.

It is useful to note the controversy of a few years ago over local equilibrium in solid state massive transformation. Ultimately, the solid-state massive transformation was found to occur usually, but not always under conditions of local equilibrum at the interface. It remains to be seen whether or not the same is true for massive solidification.

Anantharaman, et al (43) presented a review of rapidly solidified Al-based alloys in which they proposed that solutes with favorable Hume Rothery size factors (within 15% of the solvent) should be amenable to TSSE. They noted, however, that 6 of the 17 such solutes (Au, Sn, Ti, V, Zn, and Zr) had TSSE to 4 a/o or less. They sought a basis for this anomaly in thermodynamic considerations, as reflected in the phase diagram. They noted for simple eutectic systems showing small deviations from ideal solution behavior (such as Figure 1), it should be easy to supercool the liquid below T_0 and obtain massive solidification. For solid solutions with large positive deviations from ideality, however, they noted that even at absolute zero the free energy of the solid might be greater than that of the liquid, rendering massive solidification and TSSE thermodynamically impossible. Anantharaman et al also argued that in some cases TSSE will be limited by nucleation of an adjacent stable or metastable solid phase. They proceeded to develop their ideas f several cases depending on whether the terminal solid solution and adjacent phase are formed eutectically or peritectically. Anantharaman et al thus implicitly assumed that only cooling to T_0 was required for massive solidification, and that violation of local equilibirum was not a consideration.

2. KINETIC CRITERIA

Various authors have attempted to prescribe conditions for segregation-free solidification in terms of various kinetic parameters, particularly liquid and interfacial diffusion coefficients and atomic attachment rates at the solid: liquid interface. The criteria are of two basic types, appealing to either absolute interface stability or solute trapping.

Segregation-free solidification may occur even with equilibrium solute partitioning between liquid and solid if the interface is stable. Such solidification is illustrated in Figure 9. The liquid concentration at the interface rises to C'/k, where k = partition coefficient, and the solid has the same composition as the bulk liquid. At very low velocities, the interface is stable against breakdown giving cells or dendrites with the associated segregation. For most solidification rates, the interface is unstable and solute segregation occurs.

Very high growth rates give a condition known as absolute interface stability. At such growth rates the interface is moving too rapidly for solute diffusion in the liquid to

C

$\frac{C'}{k}$

C'

Solid   Liquid

Distance →
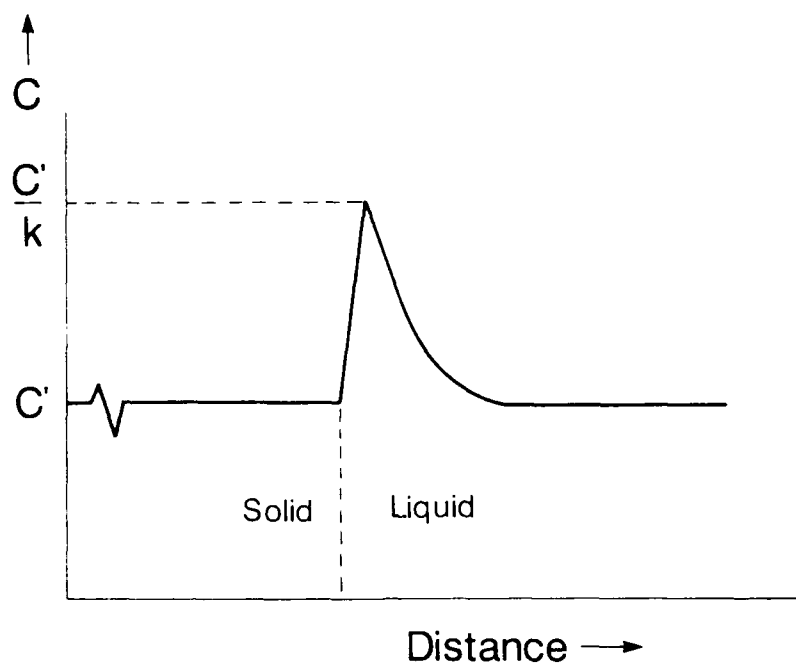
Figure 9   Steady-state segregation-free solidification with equilibrium solute partitioning. Such solidification is possible only below T_S, the extrapolated solidus.

give long wave length instabilities. The solute simply cannot diffuse rapidly enough. At the same time, short wave length instabilities which are kinetically possible give very sharp curvatures which are thermodynamically unstable. The interface is therefore stable, and segregation-free solidification occurs. There is, however, still equilibrium solute partitioning at the interface, as shown in Figure 9.

Midson and Jones (44) proposed absolute interface stability as a criterion of extension of solid solubility. Boettinger, et al (45,46) and Juarez-Islas and Jones (47) discussed the role of absolute stability in producing segregation-free solidification. Boettinger, et al found the velocities needed to give segregation-free solidification in Ag-Cu alloys to be in reasonable agreement with those predicted on the basis of absolute interface stability. They noted that their interface velocities were lower than those usually needed for solute trapping and attributed their result to absolute interface stability.

Juarez-Islas and Jones studied solidification of Al-Mn alloys in a Bridgmann furnace, so that interface velocity could be fixed by the rate of ingot withdrawal. In this experiment interface velocity was measured. The combinations of temperature, composition, and velocities giving segregation-free solidification were in good agreement with the theory of absolute stability.

25

Absolute interface stability thus appears to be a valid criterion for segregation-free solidification in at least some alloy systems. How general the criterion is remains to be seen. There is also a problem in applying the criterion to alloys and quenching processes of practical interest. It is not at all easy to determine whether or not solidification of a particular alloy in some given process will give absolute interface stability. Furthermore, as will be discussed next, while absolute interface stability may be a sufficient condition for segregation-free solidification, it certainly is not a necessary condition.

A common assumption in the modelling of solidification is that the partition coefficient is independent of interface velocity. That is, the combination of temperature and solid and liquid composition at the interface is that given by the phase diagram. Baker and Cahn (42) showed this assumption to not always be true. As discussed earlier, Zn-rich, Zn-Cd alloys have a retrograde solidus, so alloys with more Cd than the solidus maxium cannot be cooled below T_S, the extrapolated solidus. Accordingly, segregation-free solidification with equilibrium solute partitioning in such alloys is impossible. Since Baker and Cahn obtained segregation-free solidification, some mechanism other than absolute interface stability must have been operative. Baker and Cahn appealed to a solute trapping mechanism, whereby Cd atoms are incorporated into the solid, though they undergo an increase in chemical potential in the process. The actual partition coefficient is then unity, resulting in massive solidification.

Boettinger, et al. (45,46) discussed the various theories which give a velocity-dependent partition coefficient. Figure 10 shows the predictions of these theories. In each case, the partition coefficient increases monotonically from the equilibrium value (0.44) to unity as the interface velocity increases. The dimensionless velocity is $\beta = Va_0/D$, where V = velocity, a_0 = lattice constant, and D is a diffusion coefficient, which in the various models ranges from that in the liquid to that in the interface. In all theories the inflection point in k occurs at about $\beta = 1$, where the time for the interface to move one lattice spacing equals the time for an atom to diffuse one lattice spacing in the liquid or in the interface. For higher velocities, the interface simply outruns the diffusing atoms and solute segregation is impossible.

The theories for a velocity dependent partition coefficient are not terribly well developed. In addition, the ancillary data on diffusivities and interface kinetics needed to calculate k are often not available. In addition, as noted by Baker and Cahn, some solidification theories predict that k will decrease with velocity, whereas others predict an increase.

Crystallization of amorphous alloys and TSSE by solute trapping are similar in that both are related to the ease of atom movement in the noncrystalline phase. As such, our knowledge of the former may teach us something about the latter. Buschow (48) and Miedema, et al (14) related the temperatuire of crystallization of glassy alloys to the enthalpy to form a hole in the glassy phase the size of the smaller atom. Vacancies in liquids or glassy alloys are thought to have a near-zero enthalpy of migration (35) so the diffusion coefficient is determined by the hole concentration.
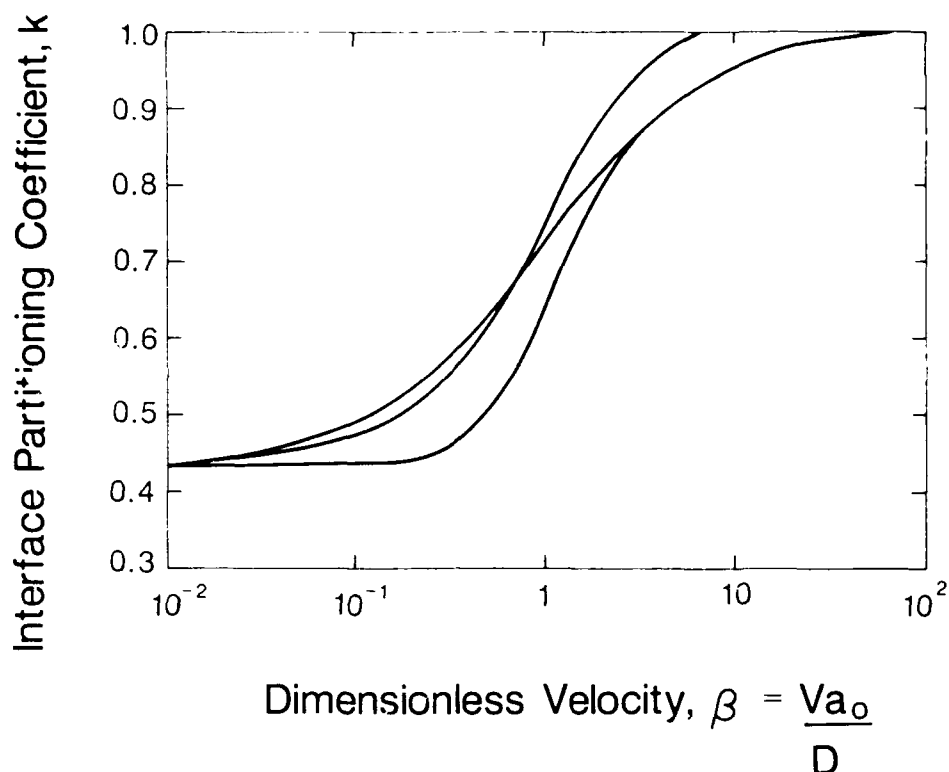
Figure 10 Dependence of partitioning coefficient on dimensionless interface velocity as predicted by various theories. For β ≳1, the solute cannot diffuse rapidly enough to avoid being trapped by the moving interface. (After Boettinger, et al, (45)).

Miedema used his macroscopic atom theory to calculate the enthalpy of hole, or vacancy formation in solid or liquid alloys (15). If the hole concentration has the usual exponential dependence on ΔH_{1v}, the enthalpy of hole formation, then crystallization would occur at a particular ratio of $\Delta H_{1v}/T$. A semi-empirical relation was in fact found to connect T_x, the absolute temperature of crystallization and ΔH_{1v}

$$T_x = 7.5\ \Delta H_{1v} \tag{39}$$

where ΔH_{1v} is kJ/mol holes.

Figures 11 and 12 plot T_x vs ΔH_{1v} for a number of amorphous alloys. The data fit Eq. (39) very well, with some deviation toward crystallization temperatures slightly lower than predicted. The fit is good enough to conclude that the kinetic criterion is adequate in predicting the temperature of crystallization of amorphous alloys.

We might expect that the temperature of crystallization is related in some way to solution thermodynamics, that a stable compound would form even at relatively low temperatures, giving crystallization. Figure 12 also plots the heat of compound formation vs composition for a number of alloy systems. No correlation exists. Meidema, et al

27
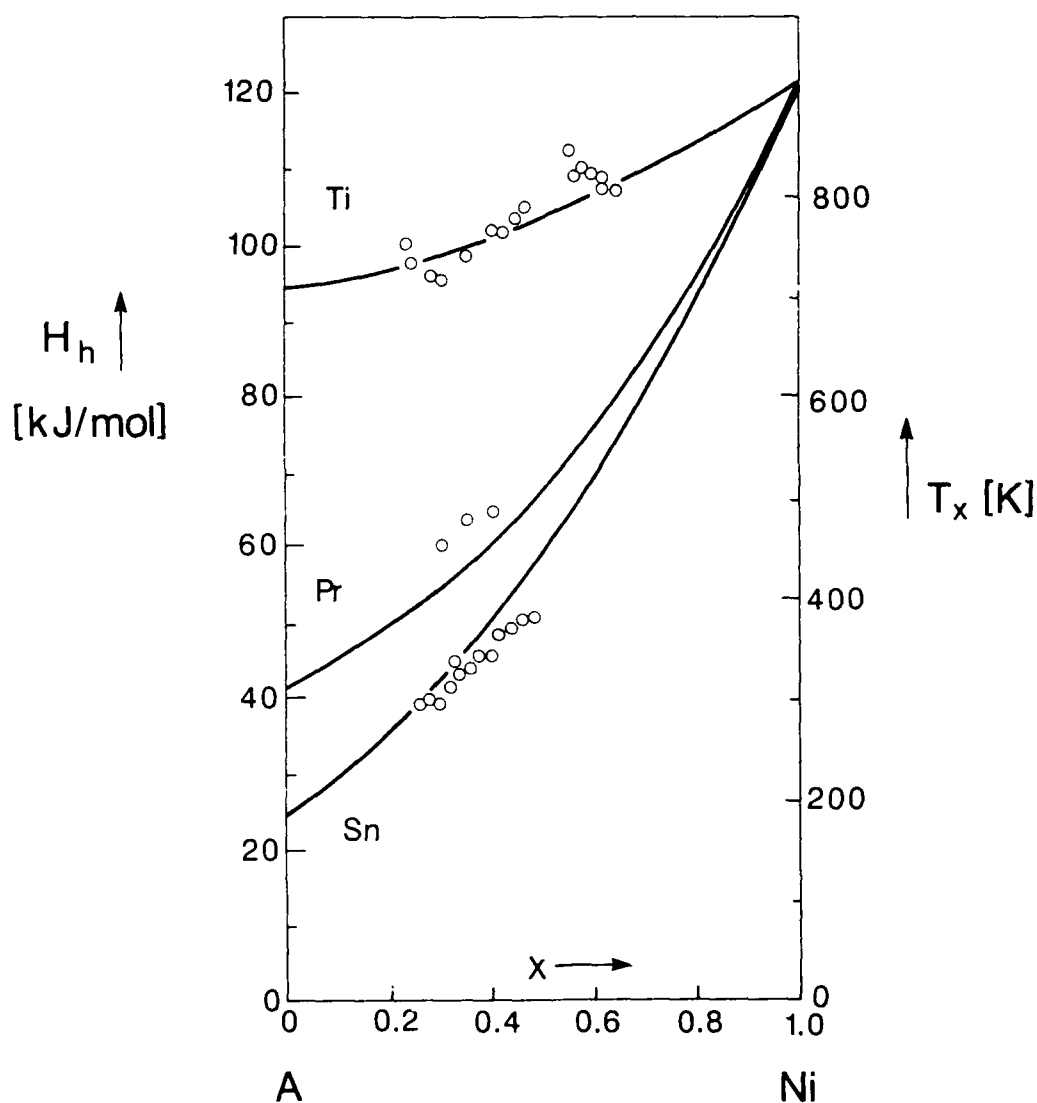
Figure 11   Dependence of the crystallization temperature T_x in various
amorphous alloys $A_{1-x}Ni_x$ on the formation enthalpy of a hole
the size of the smaller atom. (After Miedema, et al, (14)).

found a similar lack of dependence of T_x on the enthalpy of mixing of the liquid alloy, so
solution thermodynamics appear not to play a major role in determining the crystallization
temperature of amophous alloys.

Since solute trapping above T_s requires that solutes not diffuse ahead of the
solid:liquid interface, ΔH_{1v} and the conditions for TSSE may in some cases be related.
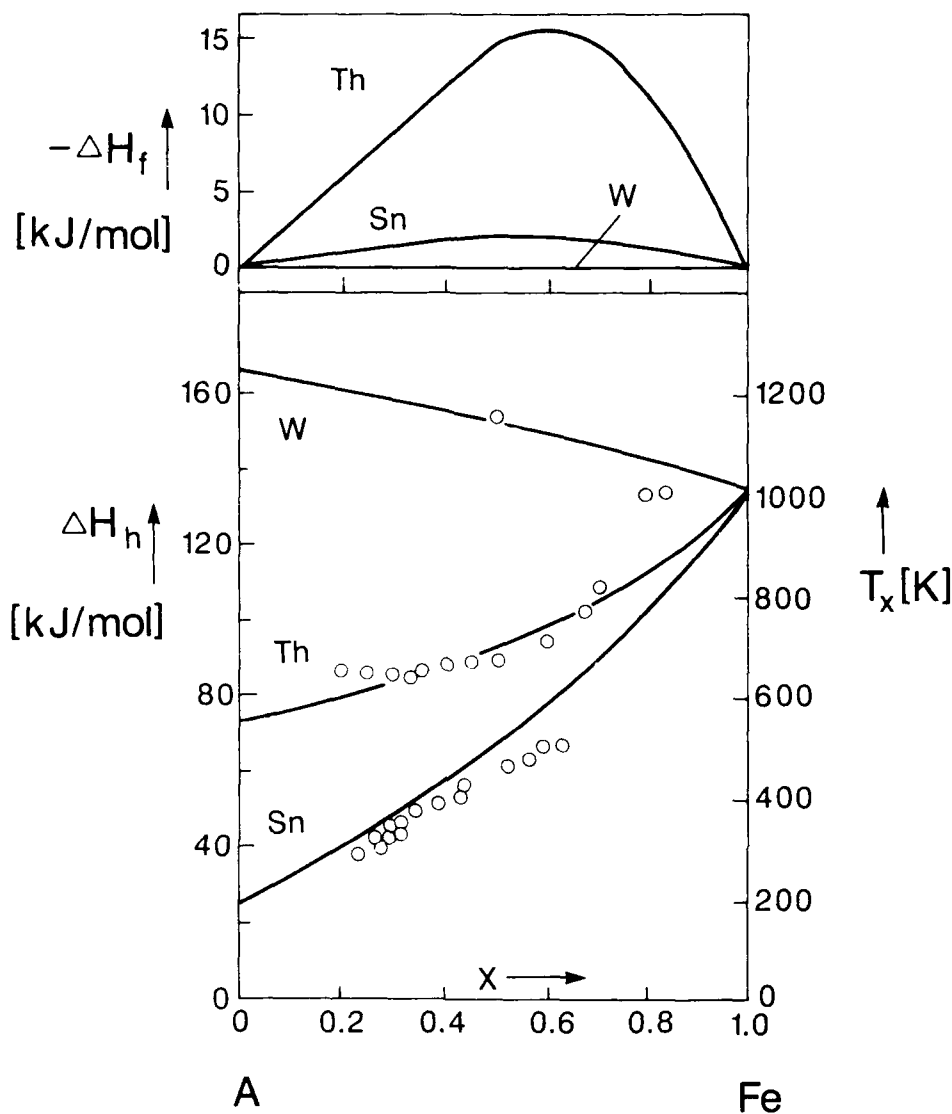
Figure 12 Plot of experimental crystallization temperatures T_x in various $A_{1-x}Fe_x$ amorphous alloys versus the corresponding heats of hole formation in the solid state. The enthalpies of compound formation are also shown for comparison. (After Miedema, et al, (14)).

3. CRYSTAL CHEMISTRY CRITERIA

Several criteria to predict equilibrium solid solubility have been devised in terms of such elemental crystal properties as Wigner-Seitz or Goldschmidt atomic radius, or electronegativity, or in the case of Miedema, electron density at the boundary of the Wigner-Seitz cell and electron potential. These criteria have some predictive power for

equilibrium solubility, and it is reasonable to suspect that they might be useful in predicting nonequilibrium solid solubility under rapid solidification.

Darken and Gurry (49) located the metallic elements on a two dimensional plot of electronegativity and atomic radius. Elements with significant solubility in a host metal tended to be clustered in an elliptical region around the host. The separation of solutes into soluble and insoluble is shown in Figure 13 for an aluminum host. The elements are separated by solubility into three groups of appoximately equal size. The plot of electronegativities and radii is from Chelikowsky (50). Solubilities are from the Metals Handbook (51), Hansen (52), Elliott (53) and Shunk (54). Figure 14 is the same plot, but for RS extended solubility in an aluminum matrix. Solubilities are from Jones (55) and Murray (56) for high cooling rates. In both cases soluble elements are clustered around the Al host, but so are some insoluble elements, while some soluble elements are located well away from the host. In Figure 13, soluble elemens Mn, Cr, and Re are located among the insoluble elements, while highly and moderately soluble elements are well mixed. Much the same kind of mixing is seen in Figure 14 for RS extended solubility. In both cases, the Darken and Gurry coordinates provide valuable guidance as to which elements may or may not be soluble, though leading to the conclusion that coordinates which better characterize solid state solubility are to be desired.
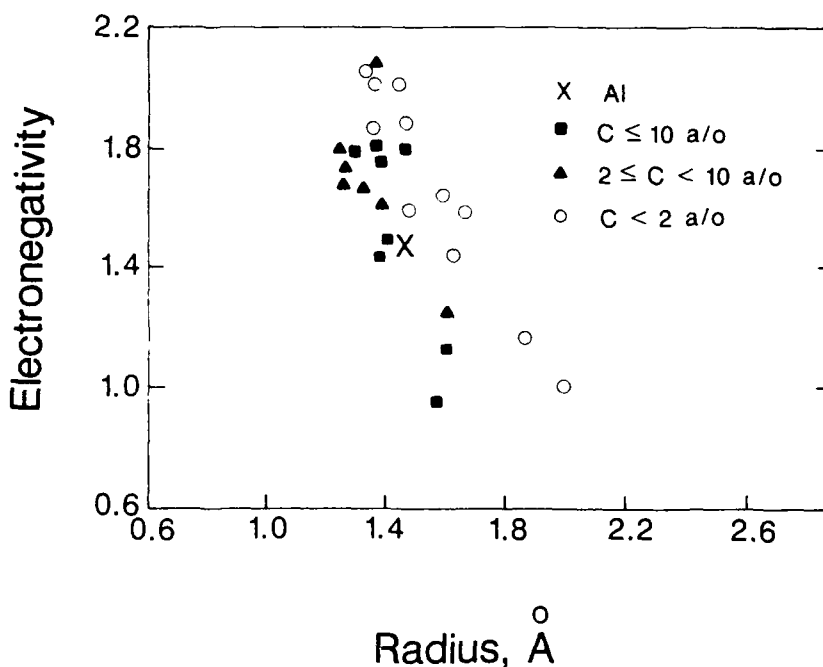
Figure 13   Darken-Gurry plot of electronegativity vs atomic radius
            showing equilibrium solubility in aluminum. Coordinates are
            from Chelikowsky (50). More soluble elements are clustered
            in an ellipitical region around the host Al.

2.2

2.0 (implied)

Electronegativity

1.8

1.4

1.0

0.6

0.6   1.0   1.4   1.8   2.2   2.6

X Al
■ $C_e \leq 0.5$ a/o
▲ $0.05 \leq C_e < 0.5$ a/o
○ $C_e < 0.05$ a/o
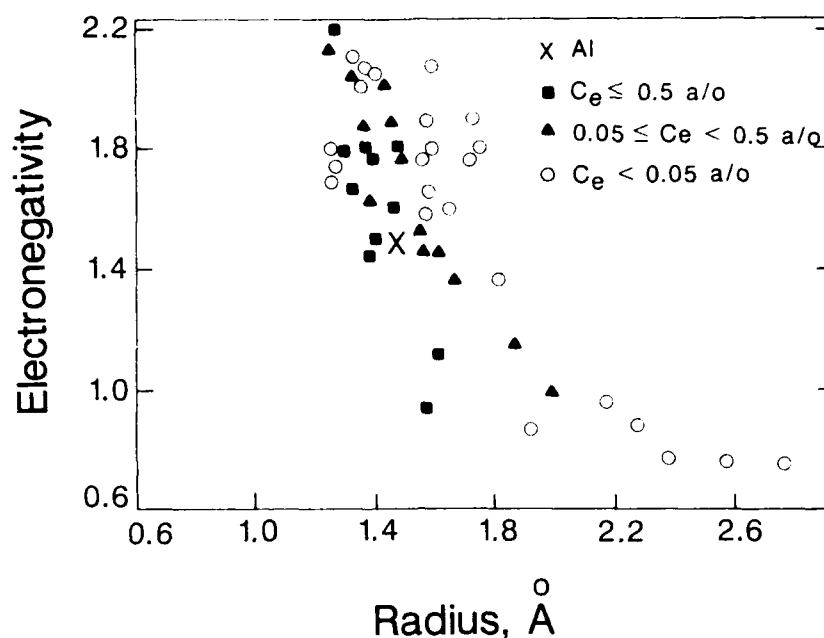
Radius, Å

Figure 14   As for Figure 13, but nonequilibrium solubility under rapid
solidification. Solubilities are from Jones (55) and Murray (56).

In Figures 13 and 14, the Pauling atomic radii are used. Other choices of radius
would give slightly different plots, and depending on the system, slightly better or worse
separation into soluble and insoluble elements.

Jones (57) analyzed equilibrium solid solubility in terms of the Wigner-Seitz atomic
radius and Miedema's values for the heat of solution of the solute in the matrix. In a study
of magnesium as a solvent Jones found a better division between soluble and insoluble
solutes than was obtained by either Darken-Gurry coordinates or the Meidema coordinates
of $\emptyset^*$ and $n_{ws}^{1/3}$.

Jones also found that the plot gave an excellent separation between elements with
high and low equilibrium solubility in aluminum, and proceeded to apply the coordinates to
nonequilibrium solidification. Figure 15 shows his results for equilibrium and Figure 16
for nonequilibrium solidification of Al-based alloys. A reasonable separation between
elements on the basis of solubility is effected in both cases. We should note, however, that
the Darken and Gurry plots and the Miedema plots involve only two crystal chemistry
parameters. Jones plots are of atomic size vs enthalpy of mixing, which involves at least
two crystal chemistry parameters. Thus, the Jones plots involve three parameters to the
other plots' two and would be expected to fit the data better.

Chelikowsky (51) compared the effectiveness of Darken-Gurry and slightly
modified Miedema plots as predictors or equilibrium solubility in divalent hosts. He found
the Miedema coordinates systematically superior, even for Mg-based alloys, where the
Darken-Gurry coordinates are most successful.

31
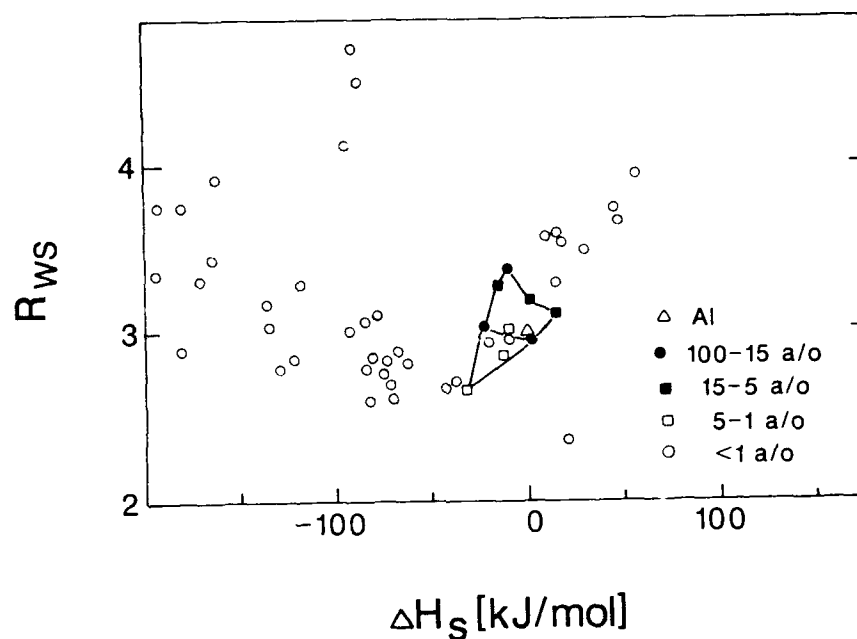
Figure 15   Jones plot of atomic radius vs heat of mixing for equilibrium solid
             solubility in aluminum. The more soluble elements are clustered
             around the aluminum host. (After Jones, (58)).
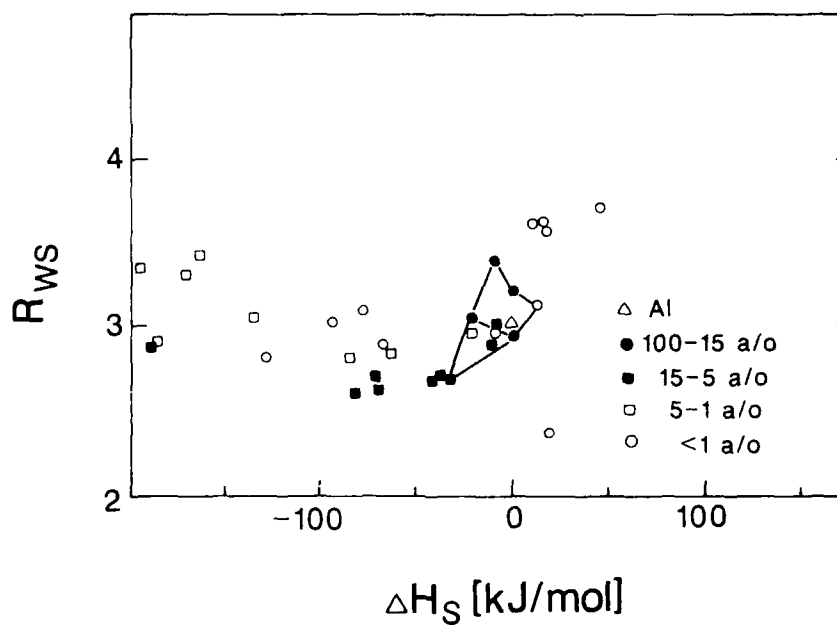
Figure 16   As Figure 15, except nonequilibrium solid solubility in Al. The
             more soluble elements tend to be close to the aluminum host. The
             separation into soluble and insoluble elements is far from perfect.
             (After Jones, (5)).

Figure 17 shows a Miedema plot for equilibrium solubility in aluminum. The solubilities are divided into three approximately equal groups. Solutes with 0.5 a/o or greater solubility are clustered nicely around the host Al. Sparingly soluble solutes, with 0.05 a/o $<$ C_e < 0.5 a/o tend to cluster just farther out, but are mixed in with some insoluble ($C_e < 0.05$ a/o) elements. The Miedema plot thus gives a good, but not perfect separation into the three solubility groups.
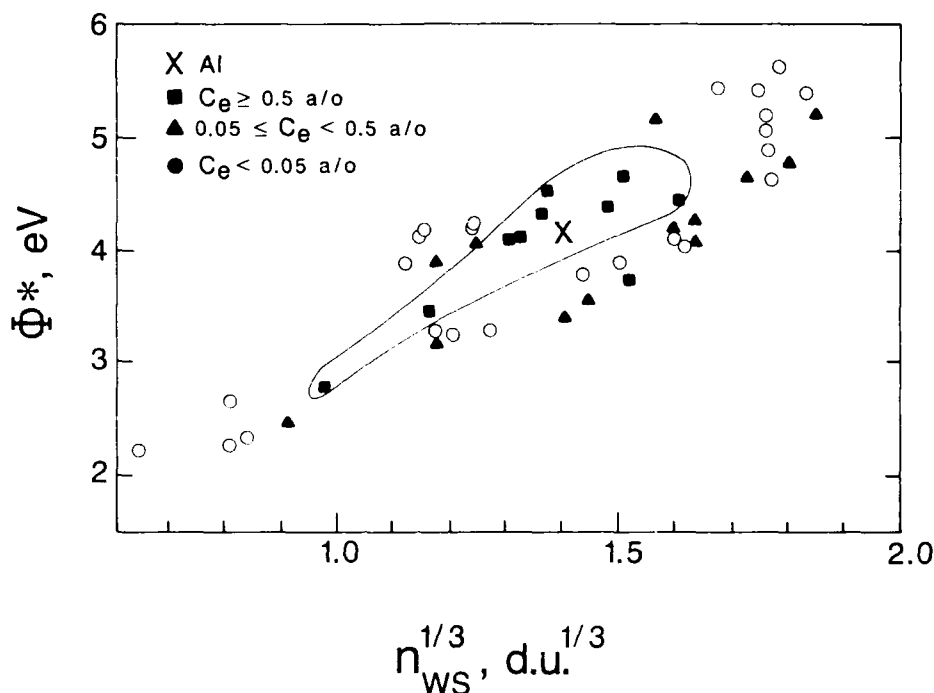
Figure 17   Miedema plot of equilibrium solid solubility in an aluminum host.
Soluble elements are clustered around the host element in a region
of convex curvature. Slightly soluble elements are somewhat
mixed with insoluble elements. A boundary is drawn around
highly soluble elements as an aid to the eye.

The separation is better than that obtained on a Darken-Gurry plot (Figure 13) or on a plot of heat of solution in solvent vs Wigner-Seitz radius (Figure 13). Clearly the Miedema coordinates reflect substantially the fundamental factors governing equilibrium solid solubility.

Chelikowski (51) found that the Miedema coordinates were remarkably successful in predicting nonequilibrium site preference under low temperature ion implantation. Injected ions cannot precipitate out of solution, but may enter solid solution in three different ways: in substitutional sites, or in octahedral or tetrahedral interstitial sites. Figures 18 shows the results for ion implantation in a beryllium host. The injected elements separate without exception into three regions separated by smooth convex borders. This remarkable separation is even better than found by Chelikowsky for equilibrium solubility in Mg or as shown in Figure 15, for equilibrium solubility in Al.
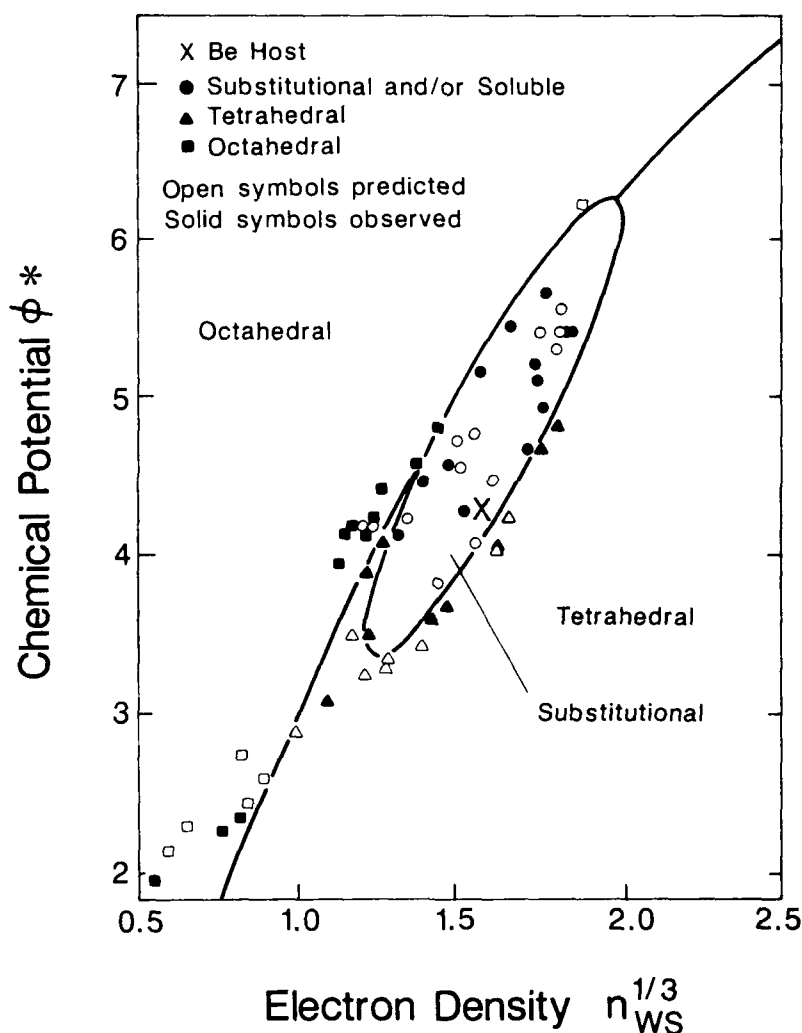
Figure 18   Miedema plot of site preference of implanted solutes in a beryllium host. The plot gives a perfect separation into three regions with smoothly curved borders. (After Chelikowsky, (51)).

34

The success of the Miedema plot in predicting equilibrium solubility and predicting site selection in ion implanted solids and crystallization in metallic glasses suggests its extension to TSSE. Figure 19 shows such a plot, again with the solubilities separated into three comparable groups. The ability of Miedema coordinates to separate the results into three regions is striking, and superior to the other schemes just discussed. The separation is perfect except that cerium with an extended solubility of 1.9 a/o is included with solutes in the 2-10 a/o range. Furthermore, the boundaries of the solubility regions are convex and smoothly curved, unlike the star-shaped boundaries found using other coordinates. Clearly the two Miedema coordinates do an excellent job of characterizing whatever forces govern TSSE in Al.
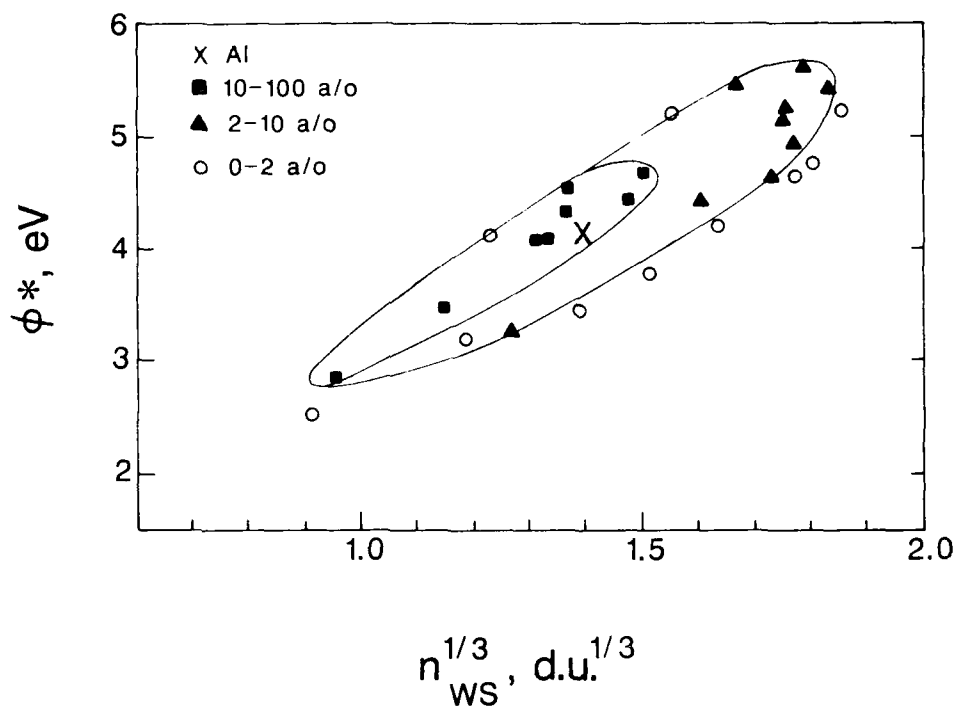
Figure 19   Miedema plot of terminal solid solubility extension in rapidly solidified Al-based alloys. A near-perfect separation into highly soluble, moderately soluble, and relatively insoluble solutes is effected. Boundaries are drawn as an aid to the eye. Solubilities are from Jones (55) and Murray (56).

We may consider the meaning of the clean separation of the elements on the Miedema plot into three regions by two convex contours. First, for illustration, consider the heats of mixing of liquids, and ignore the nonmetals and pairs of metals which have p-d or s-d hybridization. Then for mixing a particular host element with various other elements:

35

$$\Delta H\alpha - P(\Delta\emptyset^*)^2 + Q(\Delta n_{WS}^{1/3})^2 \qquad\qquad (40)$$

Setting ΔH = const, we may solve for some function $f(\Delta\emptyset, \Delta n_{WS}^{1/3}) = 0$ which may be plotted on the $\emptyset^*$, $n_{WS}^{1/3}$ plane. We could not, for example, construct such contours for the heats of mixing of solids because $\Delta\phi^*$ and $\phi n_{WS}^{1/3}$ are not sufficient to determine the solid solubilities. This point is illustrated by Figure 16 where only a very tortuous, nonphysical contour could separate the high and low solubility elements.

Any attempt to construct more contours would result in intersections of contours of different solubility. Such intersections would have elements with the same values of $\Delta\emptyset^*$ and $\Delta n_{WS}^{1/3}$ giving different solid solubilities, which proves that those two variables alone do not determine solid solubility. The smooth, nonintersecting contours for TSSE indicate strongly that for aluminum, at least, the extended solubility under RS is governed by $\Delta\emptyset^*$ and $\Delta n_{WS}^{1/3}$. Why $\Delta\emptyset^*$ and $\Delta n_{WS}^{1/3}$ should have this predictive power for TSSE and what the functional relationship is, is not known.

Figures 20 and 21 present existing TSSE data for Mg- and Ti-based alloys on Miedema plots. Neither system is nearly as well investigated as Al-based alloys, which have long been the standard for rapid solification studies. In the case of Mg-based alloys, Al, Ga, and Y all show large solubilities under rapid solidification, and all are located in an elliptical region near the Mg host on the Miedema plot. In addition, the elements showing lesser solubilities are all outside this region. There are, however, too few data to conclude on the effectiveness of the Miedema coordinates in predicting TSSE under RS for Mg-based alloys.

Figure 21 shows that somewhat the same situation exists for Ti-based alloys. The elements found to exhibit high solubilities under RS are located in an elongated elliptical region around the Ti-host. However, Ti exhibits significant solid solubility for most metals. (52,53,54). The only other RS data set lower limits of 0.5-2 at.% on solubilities of the rare earths under RS. The equilibrium solubilities are in the vicinity of 1 a/o, so it is unclear whether or not RS has significantly increased the solubilities of the rare earths in Ti. As for the Mg-based alloys, the data are too few to make any conclusions regarding the effectiveness of the Miedema coordinates in predicting TSSE under RS. The coordinates might, however, be useful in planning future RS experiments.
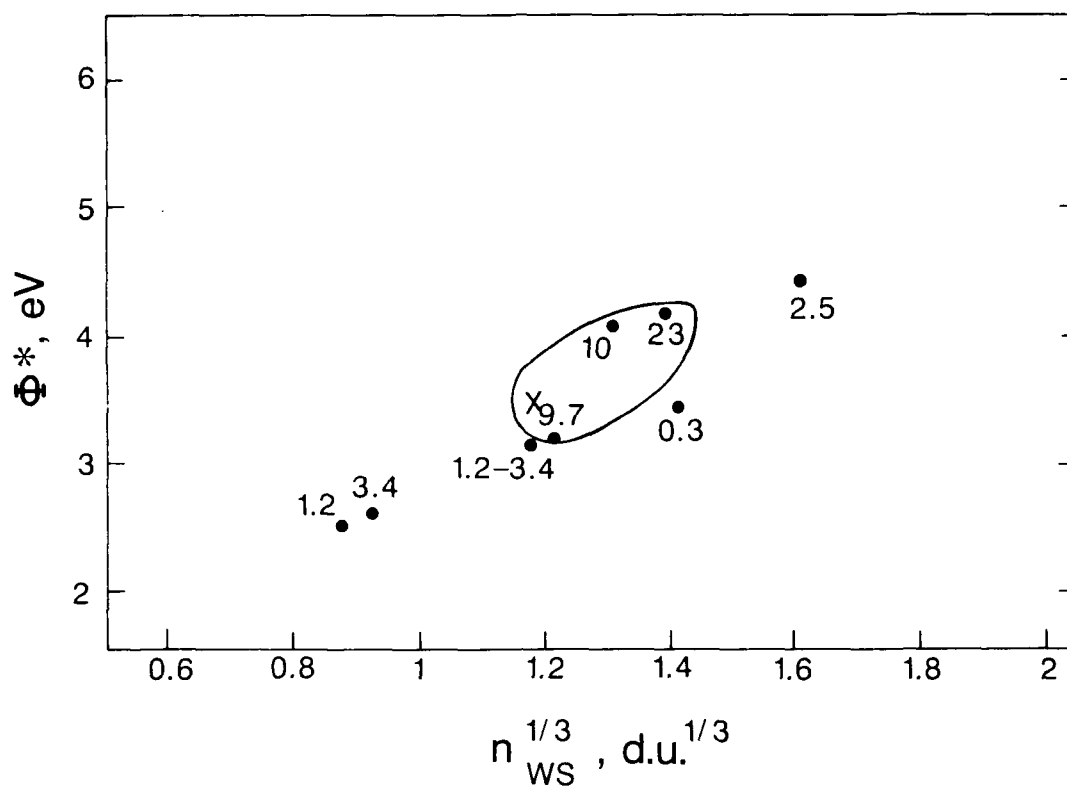
Figure 20   Miedema plot for TSSE in rapidly solidified Mg-based alloys.
The X indicates the Mg solute. There are too few data for a good
test of the criterion. (Data from Ref. 4).
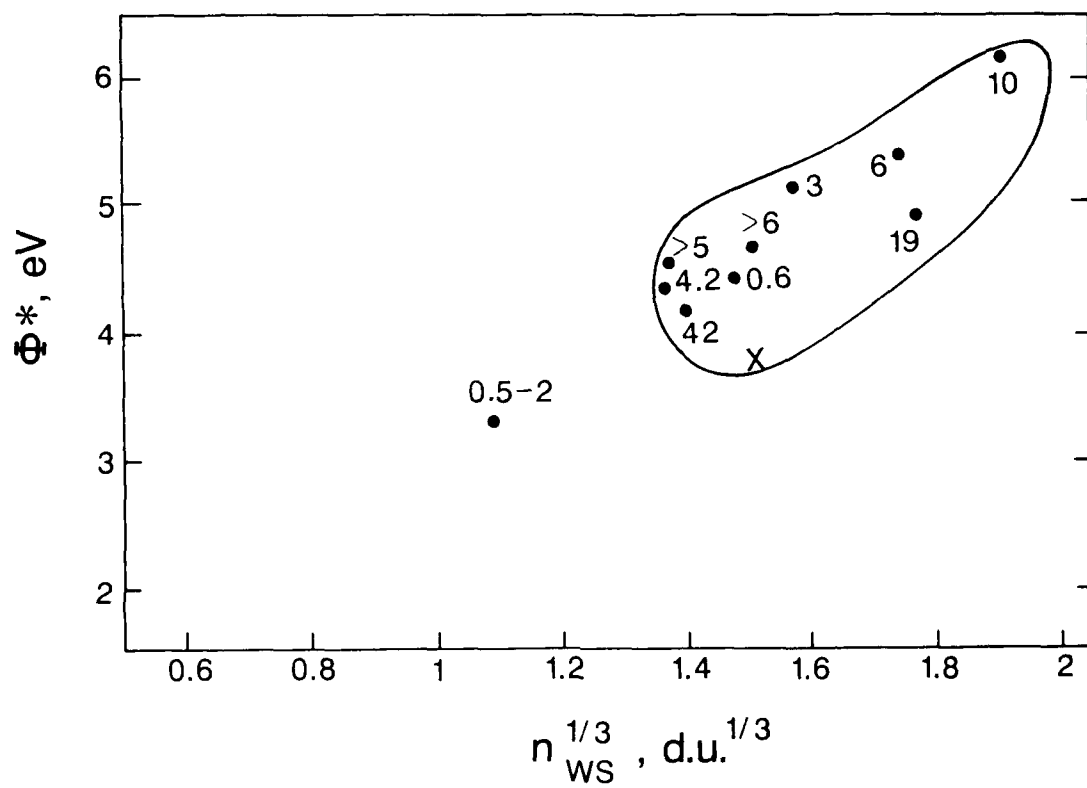
Figure 21   Same as Figure 20, except for Ti-based alloys. (Data from Ref. 4).

SECTION IV

GRAIN SIZE PREDICTION IN RAPIDLY SOLIDIFIED ALLOYS

The calculations in this section use the grain size prediction technique of Boswell and Chadwick (7) as a starting point. The calculation for grain size after massive solification begins with the Uhlmann (58) expression for fraction solidified, x:

$$x = 1 - \exp(-\pi J V^3 t^4 / 3) \qquad (41)$$

where
J = steady-state nucleation rate of solid
V = growth velocity
t = time

Homogenous nucleation of massive solidification and isothermal, isotropic growth are assumed. However, solidification during rapid quenching is hardly an isothermal process. Boswell and Chadwick used the technique developed by Grange and Kiefer (59) to calculate fraction transformed during continuous cooling on the basis of isothermal transformation kinetics.

1. KINETICS OF SOLIDIFICATION

Isothermal transformation kinetics are characterized by the so-called T-T-T diagram, shown schematically as Figure 22. The figure uses temperature and time as coordinates, with the latter usually plotted on a log scale. The contours of constant fraction transformed are plotted here: 1% and 99%. Normally such diagrams are obtained empirically. Given analytical expressions for nucleation and growth rates, however, the diagram may be calculated. According to Eq. (41), $t_{.99} = 5t_{.01}$, so once initiated, the transformation goes to completion very rapidly.

In the present case fraction transformed varies as the product of nucleation rate (J) times the growth rate (V) cubed (Eq. 41). The growth rate decreases rapidly with decreasing temperature, whereas the nucleation rate is zero at T_0, and increases rapidly with decreasing temperature. The result is the characteristic "C" - curve (Figure 22).

Isothermal transformation curves apply only to cases where the sample is quenched instantaneously from a high temperature then held at a constant reaction temperature. More usually the sample is cooled continuously during transformation. Such is certainly the case for rapid solidification, where heat transfer to a cold substrate initially gives an approximately constant cooling rate. Release of latent heat will of course slow the cooling rate, and possibly even give a temperature rise.

39

T_o

T

1% Transformation

99% Transformation

Log t
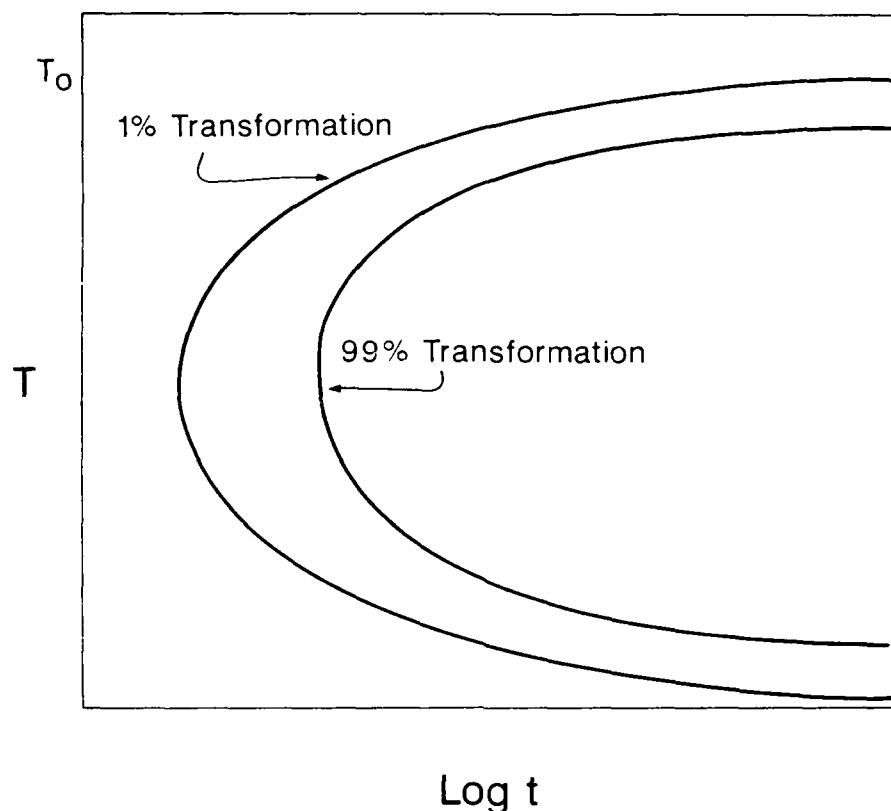
Figure 22   Schematic isothermal transformation diagram showing lines
for 1% and 99% completion of reaction.

Grange and Kiefer (59) wrote a classic paper showing how to calculate a
continuous cooling transformation curve (CCT) from the corresponding TTT curves.
Figure 23 shows the TTT diagram with an assumed cooling curve. In the Grange-Kiefer
technique, the cooling curve is broken into a number of small segments. The fraction
transformed during cooling from, say T_I to T_c during the time interval $t_c - t_I$ is assumed
equal to the amount which would have transformed isothermally on holding $t_c - t_I$ sec. at a
temperature $(T_c + T_I)/2$. The CCT curve is thus shifted downward and to the right from the
isothermal transformation curve.

In that TTT curves are usually obtained experimentally, the CCT curve is obtained
graphically. In the present case of massive solidification at large undercoatings, one may
reasonably assume homogeneous nucleation and an isotropic, size-independent growth rate
to calculate the TTT curves. The calculation of the 1% line is particularly straightforward
since the solid particles will be growing independently of one another. The time for 1%
isothermal transformation may be obtained from Eq. (41) as:

$$t_{.01} = \left(\frac{3}{100\pi \, JV^3} \right)^{1/4} \tag{42}$$
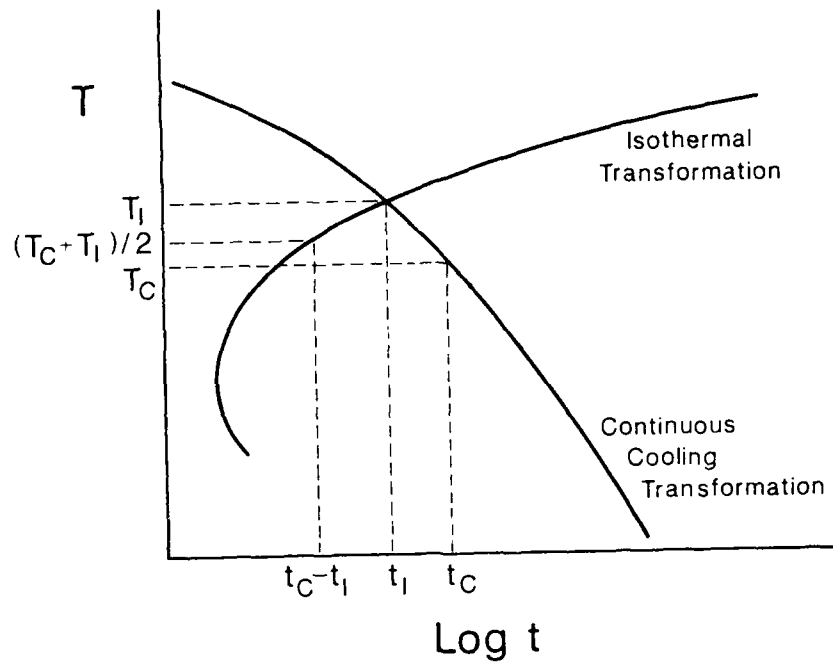
Figure 23   Schematic plot illustrating Grange-Kiefer technique for obtaining a continuous cooling transformation diagram from an isothermal diagram.

The corresponding point on the CCT curve will lie at coordinates $(t_c\ T_c)$ such that $(t_c - t_I)$ and $(T_c + T_I)/2$ lie on the isothermal curve. The cooling curve for the sample intersects the 1% TTT line at t_I, T_I. Time and temperature during continuous cooling are related by the cooling rate, $\dot{T}$:

$$T_c = T_I - \dot{T}\,(t_c - t_I) \tag{43}$$

which gives

$$(T_c + T_I)/2 = T_I - \dot{T}\,(t_c - t_I)/2 \tag{44}$$

Then:

$$(t_c - t_I) = \left(\frac{3}{100\pi\ J V^3}\right)^{1/4} \tag{45}$$

where J and V are to be evaluated at $(T_c + T_I)/2$

Equation (45) may then be solved by iteration to determine the time and temperature (t_c, T_c) at which 1% of the liquid has solidified during continuous cooling. Boswell and Chadwick showed that from this point on, solidification proceded nearly isothermally.

41

The nucleation rate increases rapidly with decreasing temperature. Accordingly, we may assume that most crystal nuclei form at a temperature very near T_c, the maximum undercooling. The grain size may then be calculated as

$$\bar{d} = \left(\frac{V}{J}\right)^{1/4} \tag{46}$$

where V and J are evaluated at T_c.

The steady-state rate of homogeneous massive solidification may be written as:

$$J = \frac{D_l}{a^5} \exp(-\Delta G^* / kT) \tag{47}$$

where

$$\Delta G^* = \frac{16\pi\gamma_{sl}^3}{3kT\,\Delta G_v^2} \tag{48}$$

and D_l = liquid diffusivity
   a = lattice spacing
   γ_{sl} = solid: liquid interfacial energy
   ΔG_v = thermodynamic driving force for massive solidification.

The growth rate in massive solidification is given by:

$$V = \frac{D_l}{a}\left(1 - exp\left(-L\left(\frac{T-T_o}{RT_oT}\right)\right)\right)$$

For the usual case of the substantial undercoolings below T_o needed to obtain homogeneous nucleation, we may write:

$$V \approx D_l/a \tag{49}$$

All the ancillary data needed to calculate J and V may be obtained from expressions presented earlier in Section II. The grain size in massive solidification during continuous cooling may then be calculated for any alloy and cooling rate of interest.

Combining Eqs (42, 47, 49) gives

$$t_{.01} = \frac{a^2}{3D_l}\exp(\Delta G^*/4kT)$$

Using Eq (48) for ΔG^* and taking

$$D_l = 10^{-5}\exp(-\Delta H_{lv}/kT) \quad (m^2/s)$$

and $a^2 \approx 10^{-19}\, m^2$

gives to good approximation:

$$\ln t_{.01} = \frac{4\gamma^3 T_0^2 V_m^2}{kTL_m^2(T-T_0)^2} + \frac{\Delta H_{1v}}{RT} - 33.4 \qquad (50)$$

The calculation of $t_{.01}$ uses the experimental result that for most metals $\Delta G^*/kT = 60$ at $T_r \approx 0.8$, $(T_r = T/T_0)$ that $D_l \approx 10^{-9}$ m^2/s at T_m, and that $\Delta H_{1v}/kT_m \cong$ const. Then the generic calculation is performed for a pure metal, and a metal with alloy addition reducing T_0 to $0.8T_m$ and 0.6 T_m. The alloy additions are assumed not to change L_M, γ_{sl}, and ΔH_{1v}.

Figure 24 shows the results of the calculation. Alloy additions are seen to shift the TTT curves strongly downward and to the right. Cooling trajectories are shown for quenches from T_0 at a rate of $10^3 T_m$/s, which corresponds to 2×10^6 K/s for Ti-based alloys and about 10^6 K/s for Al-based alloys.
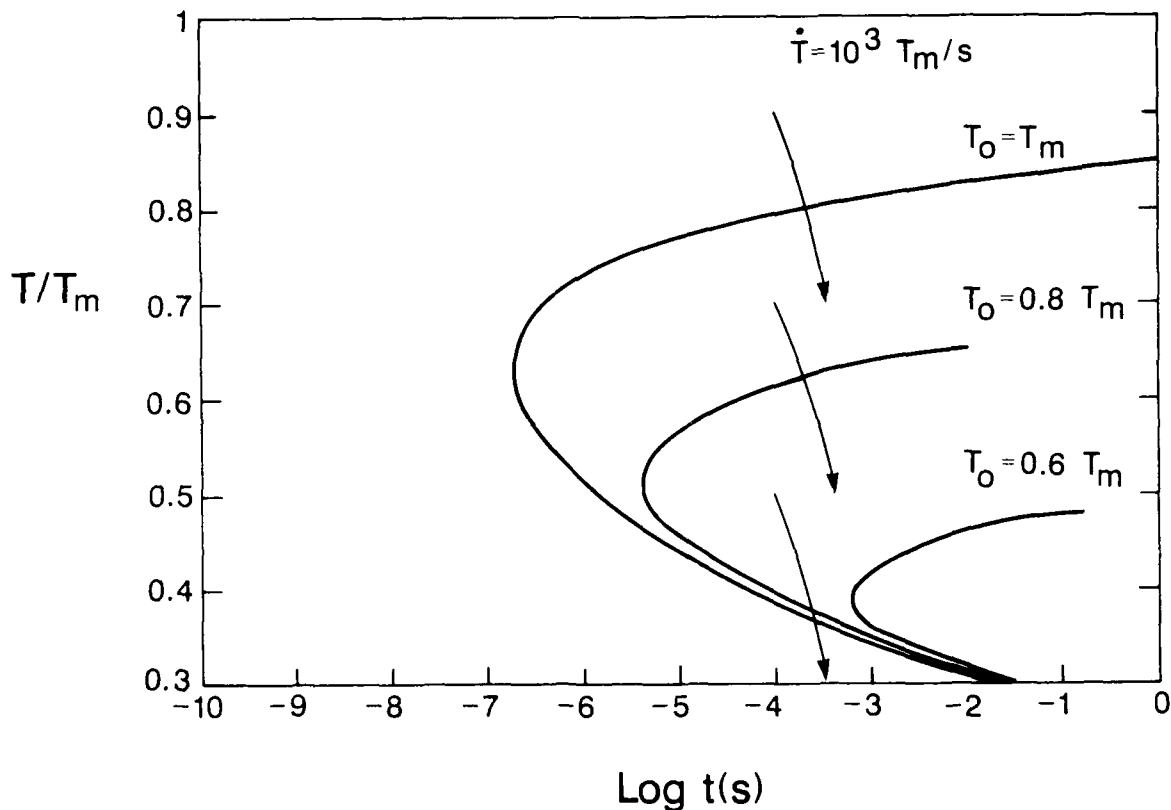
Figure 24   Isothermal transformation diagram for 1% solidification for metal
in pure state and with alloy additions which reduce T_0 to 0.8 T_m
and 0.6 T_m.

The quench totally misses the nose of the lowest TTT curve, so that a glass should be formed. The cooling trajectories are nearly perpendicular to the $t_{.01}$ curves for $T_o = T_m$ and $T_o = 0.8\,T_m$. We noted earlier that once initiated, solidification proceeds very rapidly. As such, very nearly $T_c = T_I$ and $t_c = t_I$, and solidification may be assumed to occur at T_I, where the cooling trajectory intersects the 1% transformation line on the TTT curve. The Grange and Kiefer calculation of T_c and t_c is necessary only when the cooling trajectory is nearly tangent to the TTT curve.

We may combine Eq(s) (46, 47, 49) for $\bar{d}$, J and V to obtain

$$\bar{d} = a \exp\left(\frac{\Delta G^*}{4kT_c}\right) \tag{51}$$

The diffusion coefficient thus affects $\bar{d}$ only implicitly through T_c. Figure 25 plots $\bar{d}/a$ vs T_r. Since $\Delta G^*/kT$ scales as T_r, a plot of Log $\bar{d}/a$ vs T_r is the same for all alloys which have $\Delta G^*/kT = 60$ at $T_r = 0.8$.

Figure 25 shows that Log $\bar{d}$ increases rapidly with T_r. The larger $\bar{d}$ will probably not be observed because heterogeneous nucleation will produce many grains. The noses of all three TTT curves lie at about $T_r = 0.65$, where Log $\bar{d}/a \approx 2.6$, or $\bar{d} \approx 0.1\mu m$, which is the minimum grain size obtainable through continuous cooling.

Figure 26 plots Log $\bar{d}/a$ vs $\dot{T}$. Pure Al must be quenched at a nonphysically high rate of $\dot{T} > 10^9$ K/s to obtain a $0.1\mu m$ grain size. Quenching an Al-based alloy with $T_o = 0.8T_m$ material at 10^9 K/s will give the $0.1\mu m$ grain size, whereas a quench of just over 10^5K/s gives $0.1\mu m$ grains in the $T_o = 0.6\,T_m$ material.

Figure 26 also shows that $\bar{d} = 6 \times 10^8\ \dot{T}^{-1}\mu m$ for Al and $\bar{d} = 1.5 \times 10^9\ \dot{T}^{-1}\mu m$ for Ti. Curved plots with a greater quench rate dependence of $\bar{d}$ on $\dot{T}$ were obtained for the alloys. Boswell and Chadwick calculated $\bar{d} = 3 \times 10^6\ \dot{T}^{-3/4}\ \mu m$ for Al. Their equation predicts a $3\mu m$ grain size in Al for $\dot{T} = 10^8$ K/s whereas ours predicts $6\mu m$ grains. The factor of two difference is hardly important. The difference in $\bar{d}$ is probably due to Boswell and Chadwick using a non-Arrhenius equation for D_l.

The finest grained crystalline material is not obtained by continuous cooling, but by isothermal transformation at a temperature near $T_r/3$, where $\Delta G^*/4kT$ is a minimum. In this range, grain sizes in the 10nm range should be achievable. Alloys with T_o between 600K and 1,500K will lie between 0.5 and 0.2 T_o at room temperature. For these materials, a fast enough quench to miss the nose of the TTT curve, followed by isothermal solidification at room temperature will give ultra-fine grained material.

The diffusion-coefficient must be on the order of 10^{-24}m^2/s, or greater, to give a reasonable rate of crystal growth, which implies a melting point below about 1,500K for the base metal. Higher melting metals which are quenched past the nose of the TTT curve
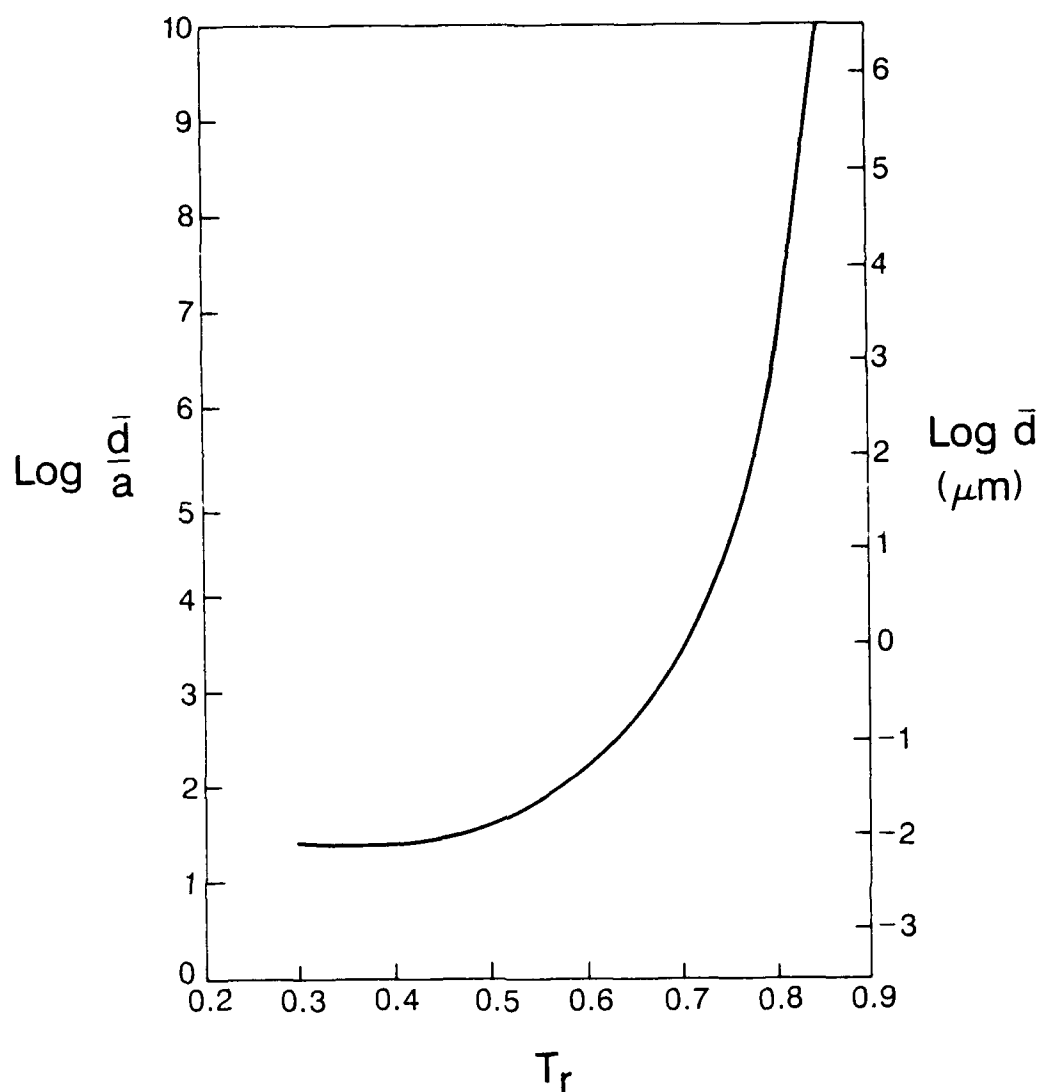
Figure 25   Predicted grain size vs. isothermal solidification temperature for
             the alloys in Fig. 24. The nose tempei ·ures of the isothermal
             transformation diagram are shown. The finest possible grains
             may be obtained in the pure metal, but only through presently
             unattainable cooling rates.

would tend to form glasses which could, in turn, be heat treated to form microcrystalline material.

    We may, short of computer calculations, examine the relevant equations to determine which factors will shift the isothermal transformation curve to longer times and give a lower solidification temperature and finer grain size. By far the most important material factor in determining T_c and the temperature of solidification is T_o. Nucleation

45
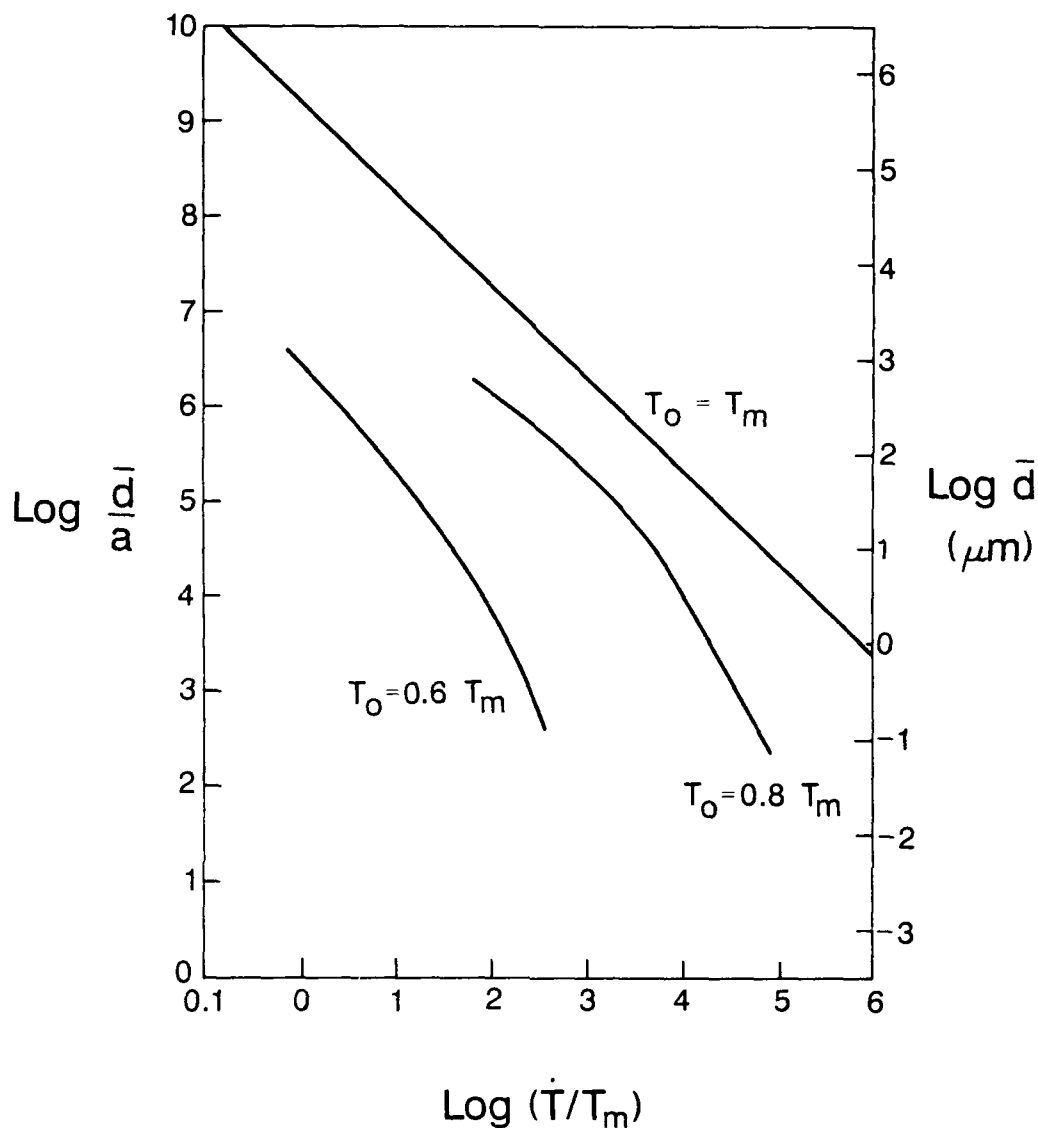
Figure 26   Calculated grain size vs cooling rate for melts based on pure Al
($T_o = T_m$) and Al with alloying additions to reduce T_o to $0.8 \, T_m$
and $0.6 \, T_m$. Surface energy, diffusivity, and enthalpy of fusion
are assumed to be unchanged by alloying.

rates scale roughly with $T_r = T/T_o$, where T_o is the temperature at which $G_l = G_s$. The 1% transformation curve is therefore shifted to the right by lowering T_o without changing D_l, so that rapid nucleation occurs at lower temperatures where growth rates are slower.

Eq. (10) shows that T_o for an alloy is the composition weighted average of the melting points of the elements, modified by a term proportional to $\Omega_\alpha - \Omega_l$. Thus, a low melting solute and a large positive value of $\Omega_\alpha - \Omega_l$ both reduce T_o and depress the onset

46

of nucleation to lower temperatures. The electronic interactions between dissimilar atoms do not differ much between liquid and solid. As such, the best way to obtain a large positive $\Omega_\alpha - \Omega_l$ is to have a large misfit in the solid solution.

We may also estimate T_0 for alloys from the phase diagram. Generally T_0 lies at a composition about halfway between those of the liquidus and solidus. Eq. (8) shows that low solute solubilities in α at the eutectic temperature indicates a large $\Omega_\alpha - \Omega_l$ and a rapidly decreasing T_0. Alloys systems in which the T_0 line (see Figure 1) drops rapidly with solute content are thus good candidatates for obtaining a fine grained solid or a glass by rapid solidification.

Examination of Eq. (42) shows that the time for 1% transformation is inversely proportional to D_l. Clearly, reducing the diffusion coefficient without changing T_0, γ_{sl} or L_m will shift the 1% transformation curve to the right and promote fine grain size. Eq. (37) shows that for a given solvent, ΔH_{lv} for the alloy is increased and D_l decreased by addition of an element with a large ΔH_{lv} in the pure liquid state. Eq. (37) may be used to calculate ΔH_{lv}. However, as ΔH_{lv} for elemental metals generally scales with T_m, a high-melting solute would tend to have a large ΔH_{lv} and retard diffusion in the liquid alloy.

An increase in γ_{sl} or decrease in L_m makes nucleation more difficult and lowers the solidification temperature. However, these changes also give a higher $\Delta G^*/kT$ (at a given temperature) which tends to increase the grain size. The grain size obtained by solidification during continuous cooling is thus affected very little by the values taken for γ_{sl} and L_m. Of course a large enough γ_{sl} or a low enough L_m may make it possible to miss the nose of the TTT curve and form a glass.

2. COMPARISON OF THEORY AND EXPERIMENT

Several investigators have measured grain sizes in RS foils. We now compare these measurements summarized in Table 1 to the predictions of theory.

Figure 26 shows that a 10^8K/s cooling rate would give a 6μm grain size in pure Al. Jones (3) alluded to a 0.1μm grain size in pure RS Al but also reported a 2.6μm grain size for pure Al in a study of piston - quenched Al-Zr alloys. In the absence of any description of the experiment leading to a 0.1μm grain size, we accept the 2.6μm grain size as characteristic of piston - quenched Al.

The 2.6μm grain size after a 10^8K/s quench lies very close to both the 3μm grain size predicted by Boswell and Chadwick and the 6μm predicted herein. The disagreement with either calculation is minor and certainly within the uncertainties in the model, material parameters, and quench rate.

Appropriate adjustments in L_m, γ_{sl}, and D_l will give solidification at a lower temperature and produce a finer grain size. A 15% increase in γ_{sl} would cause solidification to begin at approximately 500K, where isothermal solidification would

Table 1

Grain Size in Rapidly Solidified Alloys

Alloy	Observation	Reference
Aℓ	$\bar{d} = 3 \times 10^6 \, \dot{T}^{-3/4}$ μm (Theoretical)	7
Aℓ	$\bar{d} = 6 \times 10^8 \, \dot{T}^{-1}$ μm (Theoretical)	This report
Ti	$\bar{d} = 1.5 \times 10^9 \, \dot{T}^{-1}$ μm (Theoretical)	This report
Aℓ	$\bar{d} = 2.6$ μm (Piston Quench)	3
Aℓ -2.7 a/o Zr	$\bar{d} = 0.6$ μm (Piston Quench)	3
Aℓ -2 a/o Fe	$\bar{d} = 0.3$ μm, $\dot{T} \cong 10^8$ K/s	61
Aℓ -33 a/o Ge	$\bar{d} = 10$ μm, $\dot{T} \cong 10^8$ K/s	60
Ag-50 a/o -Cu	$\bar{d} = 3$ μm, $\dot{T} \cong 10^8$ K/s	7
Ti-22 w/o Fe	$\bar{d} = 3 \times 10^4 \, \dot{T}^{-62}$ μm, 10^5 K/s $< \dot{T} < 10^7$ K/s	65
Ti-28 w/o W	$\bar{d} = 3.3 \times 10^5 \, \dot{T}^{-79}$ μm, 10^5 K/s $< \dot{T} < 10^7$ K/s	65
Ti-11.5Mo-6.5Zr-4.5Sn (w/o)	$\bar{d} = 135$ μm at $\dot{T} - 10^3$ K/s, $\bar{d} = 7$ μm at $\dot{T} = 10^5$ K/s	63
Ti-6Aℓ -4V (w/o)	$\bar{d} = 3.1 \times 10^6 \, \dot{T}^{-93\pm.12}$ μm, 10^4 K/s $< \dot{T} < 10^7$ K/s	62

produce a 0.1μm grain size. However, the 10^8K/s cooling trajectory would intersect the TTT curve very near the nose, resulting in incomplete solidification.

An arbitrary 20 fold reduction in D_l would cause solidification to commence at 650K, where isothermal solidification would give a 0.1μm grain size. However, again, 650K is very near the nose of the TTT curve, and incomplete solidification would again occur. There is thus no adjustment of material parameters which would give an 0.1μm grain size in pure Al quenched at 10^8K/s.

Boswell and Chadwick concluded that the minimum grain size attainable under RS was about 0.4μm. They did not calculate T_o and ΔG_v, as was done herein. They may well have assumed implicitly that ΔH_{1v} scales with T_o, which Miedema has shown generally not to be the case.

Boswell and Chadwick (7) report a 3nm grain size in a RS Ag - 50 at % Cu alloy and Ramachandrarao et al (60) report a 10nm grain size in a RS Al-33 at % Ge alloy. Let us compare these results with theoretical predictions.

Eq. (8) for $\Omega_\alpha - \Omega_l$ may be evaluated for Ag-Cu assuming either Ag or Cu to be the solute. Taking an Ag solute gives $\Omega_\alpha - \Omega_l = 11.5$ kJ/mol, whereas taking Cu to be the solute gives $\Omega_\alpha - \Omega_l = 19.5$ kJ/mol. Substituting the average of these values into Eq. (10) gives $T_o = 906$K (1,172F) , or $T_o/T_m = 0.67$ based on Cu or 0.73 based on Ag.

In the case of the Al-Ge alloy, Eqs (13,14) were used to calculate $T_m' = 338$K and $L_m' = 10$kJ/mol for metallic Ge. The low T_m' reflects the thermodynamic instability of the metallic Ge phase. Based on Eqs. (8,13,14) $\Omega_\alpha - \Omega_l = -4.1$ kJ/mol for Al-Ge. Eq (10) then predicts $T_o = 672$ K, or $T_o/T_m{}^{Al} = 0.72$. Figure 4 shows that $n_{ws}^{1/3}$ is nearly the same for Al and Ge. Then assuming Ge is the larger atom in the liquid as it is in the solid, we would predict ΔH_{1v}, hence D_l would be approximately the same in Al-Ge alloys as in pure Al.

Figure 24 shows that a 10^8K/s quench would completely miss the nose of the TTT curve for $T_o = 0.6$ T_m, and would probably only graze the nose of the TTT curve for $T_o = 0.7$ T_m. Thus, either the Ag-Cu or Al-Ge alloy would be largely or totally a glass immediately after the quench and would crystallize at or near room temperature. Figure 25 shows that room temperature crystallization would give about a 10nm grain size, as compared to the experimental values of 3nm for the Ag - 50 at % Cu and 10nm for the Al - 33 at % Ge alloy. Agreement between theory and experiment is certainly satisfactory.

Jones (3) reported that a 2.7 at. % Zr addition to Al reduced the grain size in piston quenched material from 2.6μm to 0.6μm. The Al-Zr phase diagram shows that the Zr addition changed T_o hardly at all. Miedema calculated that ΔH_{1v} is nearly three times higher in Zr than in Al. Eq. (37) shows that ΔH_{1v} for the alloy is a composition and molar volume weighted average of the constituents. As such, ΔH_{1v} should be significantly

higher in the alloy than in pure Al. This increase is predicted to give a significant decrease in the RS grain size, in agreement with experiment.

Jones (61) shows a micrograph of a gun-quenched Al - 2 at % Fe extended solution with 0.3μm grains. The phase diagram indicates that the 2 at % Fe addition would decrease significantly T_0 below T_m^{Al}. Addition of the higher melting Fe would decrease D_l. The predicted result of the Fe addition is a significant decrease in grain size, as observed.

Figure 26 gives $\bar{d} = 1.5 \times 10^9 \ \dot{T}^{-1}$μm for Ti, which predicts a 150μm grain size for pure Ti quenched at 10^7/s. Several studies (62-65) have measured the grain size in RS Ti alloys quenched at rates from 10^3 K/s to 10^7 K/s. Krishramurthy, et al (64) determined $\bar{d} = 3.3 \times 10^5 \ \dot{T}^{-.79}$ for Ti - 28 w/o W and Baeslack, et al (65) determined $\bar{d} = 3 \times 10^4 \ \dot{T}^{-.62}$ for Ti-22 w/o Fe. Both alloys would yield grain sizes in the 1μm range after a 10^7 K/s quench, two orders of magnitude lower than theory predicts for pure Ti.

The phase diagram shows that T_0 for Ti - 22 w/o Fe is near 1,400K (2,061F), so that $T_0/T_m \approx 0.7$. Miedema calculates nearly the same ΔH_{1v} for Fe and Ti. However, in the liquid state $V_{Fe}/V_{Ti} \approx 0.7$. The enthalpy to create a hole the size of the Ti atom is slightly increased by the Fe addition. However, ΔH_{1v} for a hole the size of the Fe atom is only about 2/3 that for the Ti atom. If D_l for the smaller Fe atom controls nucleation and growth, a grain size in the 100μm range is predicted. If D_l for the Ti atom is operative, a 10^7K/s quench should intersect the TTT curve modestly above the nose and give a grain size in the micron range, as observed.

The Ti = 28 wt. % (~10 at. %)W alloy has $T_0 \approx 2125$ K, so that $T_0/T_m = 1.06$. However ΔH_{1v} for W is 3/2 that for Ti. Smithells Reference book (39) gives $V_m^W/V_m^{Ti} \approx 0.9$. The net result of the W addition would be a significant decrease in D_l. Theory would predict that $\bar{d}$ would be reduced significantly below the 150μm characteristic of pure Ti quenched at 10^7 K/s, but probably not to the ≈ 1μm grain size observed.

Broderick, et al (62) found $\bar{d} = 3.1 \times 10^6 \ \dot{T}^{-.93\pm.12}$μm for Ti-6 Al-4V, which gives $\bar{d} \approx 1$μm at $\dot{T} = 10^7$K/s. The alloy additions give $T_0/T_m \approx 0.98$, which would have a minor effect on the grain size. The addition of the low melting Al and the smaller V to Ti should give a modest increase in D_l. The net result of the alloy addition would be to give a modest increase in grain size over the 150μm predicted for pure Ti quenched at 10^7K/s. Theory and experiment in this case differ by a factor of over 100.

Broderick, et al (62) quenched Ti - 11.5M_0 - 6Zr - 4.5Sn and determined $\bar{d} = 40$μm at $\dot{T} = 10^3$K/s and $\bar{d} = 2$-4μm at $\dot{T} = 10^5$K/s. The alloy additions should give $T_0 \approx 1.02 \ T_m$ and would have only a modest effect on D_l, so at $\dot{T} = 10^5$K/s the predicted grain size is in the cm range, 10^4 times the observed value.

The Ti-6Al-4V alloy is a near-α alloy which presumably solidified as β phase, then transformed to α. The final grain size is that produced by the solid-state β to α phase transformation, and not by rapid solidifications. The Ti-11.5 Mo-6Zr-4.5 Sn alloy is β-phase at room temperature and presumably solidifies in that structure. The fine grain size obtained at a relatively low cooling rate remains a mystery.

It is clear that the theory developed herein is effective in predicting RS grain size in Al-based and Ti-based alloys except for Ti-6Al-4V and Ti-11.5 Mo-6Zr-4.5Sn. In those two alloys, the alloying elements reduce the grain size far below that expected in pure Ti quenched at the same rate, but do so without changing significantly T_o and D_l, the two parameters which most strongly affect the grain size.

SECTION V

DISPERSOIDS IN ALLOYS

1. BOUNDARY PINNING

We know that a fine dispersoid is highly effective in limiting grain growth and thereby stabilizing a fine grain size. Not surprisingly, various authors have developed theories to explain and predict this phenomenon.(66)

We may, for simplicity, consider a spherical particle of diameter d lying on a grain boundary. Pulling the grain boundary away from the stationary particle (steps a,b,c in Figure 27) requires "filling" a hole in the grain boundary of area $\pi d^2/4$ of surface energy γ_b. The driving force for grain growth must be great enough to supply this energy; otherwise the grain boundary is immobile and grain growth stops.

Growth of a grain at the expense of the surrounding grains involves three free energy charges:

1. An increase in the grain boundary energy of the growing grain.
2. A decrease in the grain boundary energy of the surrounding grains.
3. Creation of grain boundary energy as the boundary is pulled away from second phase particles.

Let us approximate the growing grain as a sphere. Then the variation of area with grain volume is $dA_1 / dV = 4 / D$. The change in grain boundary area of the surrounding grains is hard to calculate directly. We note, however, that grain growth will not occur if $D = \bar{D}$, where $\bar{D}$ is the average grain size. Therefore, $dA_2 / dV = 4 / \bar{D}$ and,

$$\frac{d(G_1 + G_2)}{dV} = -4\gamma \left(\frac{1}{D} - \frac{1}{\bar{D}}\right)$$

If the free energy increased linearly as the boundary moved from the particle equator to the south pole, $dG_3 / dV = 2f\gamma_b/D_p$, where D_p = second phase particle diameter. There is, however, a maximum in dG_3 / dV, so that $dG_3 / dV \approx 3f\gamma_b/D_p$. Setting $d(G_1 + G_2 + G_3) / dV = 0$, we may write for D_m, the limiting grain size:

$$D_m / D_p = 4(\alpha - 1) / 3f \qquad (52)$$

where $\alpha = D_m / \bar{D}$ and f = volume fraction dispersoid.
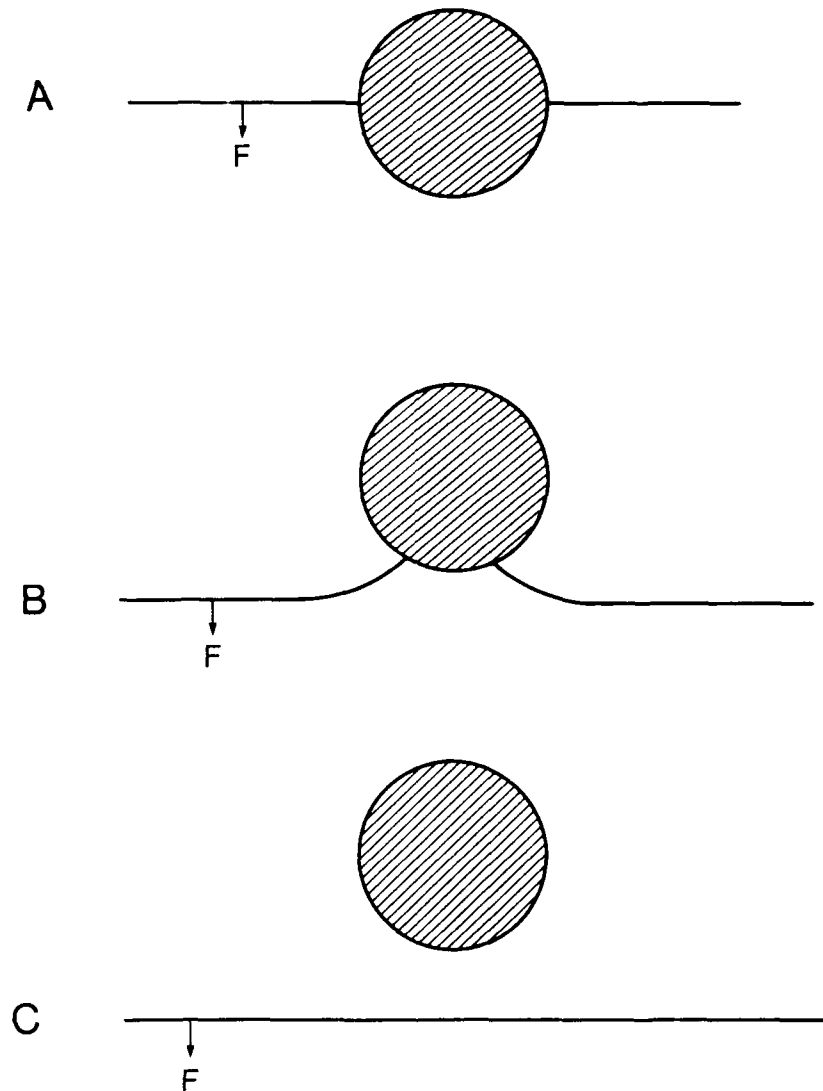
Figure 27   Schematic illustration of grain boundary pinning by a particle.
The boundary is (a) at equilibrium, (b) on the verge of breaking
away, (c) free after breaking away.

Hillert (67) derived an identical expression by a different route. The original expression of Smith (68) was $D_m / D_p = 3/4f$ which is equivalent to Eq. (52) if $\alpha = 25/16$. Hillert has shown that in normal grain growth α may take values up to 2. The value of $\alpha = 25/16$ is thus not unreasonable. As written, however, the Smith expression gives the diameter of the smallest isolated particle which would not spontaneously shrink to nothing.

Rios (69) recently took a different approach to particle pinning. He ignored the energy to fill the hole (Figure 26) and assumed that each passing grain boundary deposited a layer of interface on the particle with energy $\pi D_p^2 \gamma_b$. Rios considered the energy change as the grain size increased to obtain $D_m / D_p = 1/6f$ which again does not involve $\bar{D}$. Certainly the spread in grain size must have an important role in determining D_m.

The idea that the particle, matrix interfacial energy, γ_{pm} increases as the grain boundary passes is interesting and has some merit if the particle originally has a low energy coherent interface with the original grain. Certainly this coherency will be lost as the first grain boundary passes and γ_{pm} will increase. However, passage of the second and succeeding interfaces will not further increase γ_{pm}. Matrix and pinning may then only occur by the mechanism shown in Figure 27. This requirement of "filling in" grain boundary holes was ignored by Rios. In addition, if the the particle: matrix interface is largely incoherent, γ_{pm} will not be changed by passage of even the first grain boundary.

Pulling a grain boundary away from a pore also involves creation of $\pi D_p^2 \gamma_b / 4$ grain boundary energy. By the models of Smith and Hillert, pores should be as effective as particles in limiting grain growth. Rios' model, on the other hand, predicts that pores would have no effect in limiting grain growth, a prediction contrary to experience.

Certainly one pore or particle will not stop the growth of a grain. Effective pinning requires approximately one pore or particle per face, which has been shown to occur if

$$D_m / D_p \gtrsim f^{-0.5} \tag{53}$$

For a typical volume fraction $f = .01$, the inequality is satisfied by $D_m / D_p \gtrsim 10$. The inequality may in fact be somewhat too stringent. If, for instance, only 1/3 - 1/2 of the 14 faces of a cube-octahedron were pinned, the grain could only grow by taking on a high surface to volume ratio and a higher than minimum free energy.

2. FORMATION

We first consider the conditions required for precipitation of a few volume percent of a dispersoid compound AB in a solid alloy, M. Introduction of the needed amounts of A and B into solution in liquid M requires the following:

- A and B each are soluble to several percent in the liquid M.

- Neither A nor B forms a compound with the constituents of M which is more stable than AB.

- A and B do not react with one another in liquid M to form AB or another compound of A and B.

54

Dissolving significant amounts of A and B into solution in the liquid requires first that the heats of solution of both A and B in M not be too positive or too negative. A large positive heat of solution would prevent A or B from dissolving. A large negative heat of solution of A or B would lead to compound formation with one or more of the constituents of M, so that the second condition would not be satisfied.

The tendency toward compound formation in the liquid is primarily determined by ΔH_{net}, the enthalpy change on forming the compound from elements in solution.

$$\Delta H_{net} = \Delta H_f - \Delta \overline{H}_A - \Delta \overline{H}_B \tag{54}$$

where ΔH_f is the enthalphy change on forming AB from elemental A and B, and $\Delta \overline{H}_A$ and $\Delta \overline{H}_B$ are the partial molar heats of solution of A and B in M, respectively. The interpretation of Eq. (54) is straightforward: the enthalpy of formation of AB from A and B in solution is the enthalpy of formation of AB from the elements minus the enthalpy change on dissolving elemental A and B in the solution.

A large, negative ΔH_{net} will tend to cause AB formation in the liquid, producing a coarse, heterogeneously distributed dispersoid of no benefit in the alloy. However, we will see later that a large, negative ΔH_f in solid M is needed both to give a high nucleation rate and to produce a coarsening-resistant dispersoid. The only way to prevent formation in the liquid of a dispersoid with a large, negative ΔH_f is for $\Delta \overline{H}_A + \Delta \overline{H}_B$ in the liquid to be negative and fairly large. At the same time, neither $\Delta \overline{H}_A$ nor $\Delta \overline{H}_B$ may be so negative as to give a reaction of A or B with one or more of the constitutents of M.

Formation of a fine particle dispersion in the solid requires first of all that A and B be distributed uniformly in the solid at the end of solidification. This objective usually can only be obtained by solidification rapid enough to give terminal solid solubility extension and little segregation (2-5). Slow solidification would tend to lead to segregation, producing coarse, inter-dendritic AB in the liquid and coarse, heterogeneously distributed AB formed during cooling of the solid. Neither kind of particle is likely to be beneficial in either strengthening or grain size control.

Formation of a fine, uniform distribution of dispersoid in the solid requires a high homogeneous nucleation rate, which in turn requires a high enthalpy of compound formation. The relevant enthalpy is given by Eq. (54), except $\Delta \overline{H}_A$ and $\Delta \overline{H}_B$ now refer to the enthalpies of solution of A and B in solid M. We are now faced with a dilemma: we earlier required the enthalpies of solution of A and B in liquid M to be significantly negative, and now we want the same elements to have positive, or at least less negative enthalpies of mixing in solid M.

The electronic interactions which govern the enthalpies of mixing liquids and in solids are essentially the same (12). However, solid solutions usually have a contribution to the enthalpy missing in liquids, namely a positive strain energy due to atomic misfit. Then if A or B, or preferably both, do not fit well into the solid M lattice, $\Delta \overline{H}_A$ and $\Delta \overline{H}_B$ in

the solid may be substantially less negative than in the liquid. Then $\Delta\overline{H}_{net}$ will be considerably more negative for AB formation in the solid than in the liquid.

Formation of a high number density of fine dispersoid particles requires a high homogeneous nucleation rate. It is enough to note here that any phase which is thermodynamically stable enough to have a large enough $\Delta\overline{H}_{net}$ to resist high temperature coarsening will have a large enough driving force for precipitation to exhibit very rapid homogeneous nucleation from solid solution. A time-temperature cycle may then be chosen to give the desired combination of particle number density and mean particle size.

3. THERMAL STABILITY

Dispersoids formed in situ will usually be produced in rapidly solidified (RS) alloys which typically solidify in the form of fine powders, flakes, or thin strip or ribbon (70). These products are consolidated into bulk form by various combinations of cold and hot pressing and hot extrusion. The dispersoid particles thus must be stable against coarsening not only during service, but during hot working operations.

Particle coarsening is driven by differences in solubility between large and small particles (71). The solubility of a small elemental particle of radius r is elevated over that of the bulk phase according to

$$C^r = C^e \exp\frac{2\gamma V_m}{rRT} \tag{55}$$

where

- C^r and C^e are solubility of the particle and of the bulk phase, respectively
- γ is particle: matrix interfacial energy
- V_m is molar volume in the particle
- RT is gas constant times absolute temperature.

Coarsening of a distribution of particles occurs as shown in Figure 28. The matrix concentration of solute will be fixed at sor e value corresponding to the average particle size, $\bar{r}$, and particles such as (2), with $r < \bar{r}$ will shrink by losing solute into the matrix. Particles such as (1) with $r > \bar{r}$ will grow by capturing solute from the matrix.

Solute may follow several different diffusion paths in producing coarsening; we consider these in turn.

A. Volume Diffusion Control

Wagner (72) and Lifshitz and Slyozov (73) presented detailed analyses of the evolution of particle distributions because of volume diffusion controlled coarsening. The two studies concluded that the mean particle radius, $\bar{r}$, varied as

56
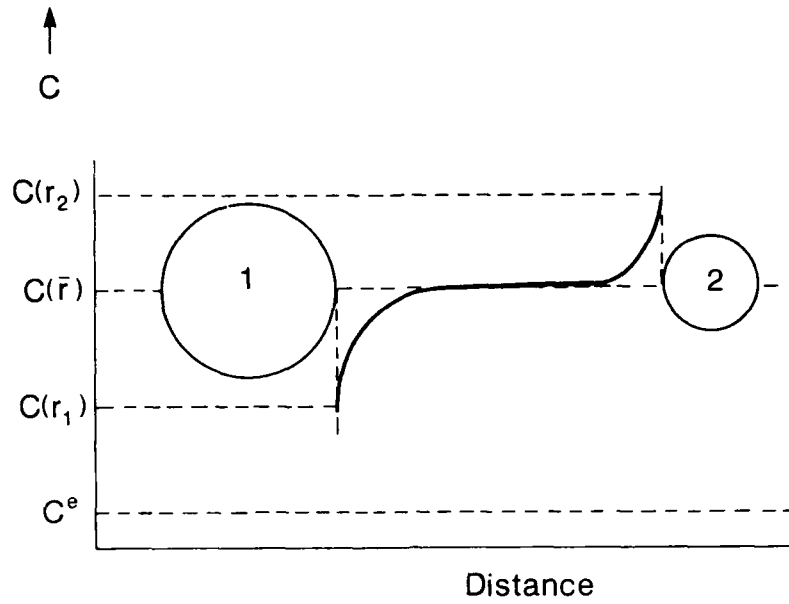
Figure 28   Schematic representation of particle coarsening. The small particle (2) with r<r̄ dissolves into the matrix and the large particle (1) with r>r̄ grows.

$$\bar{r}^3 - \bar{r}_0^3 = \frac{8\,\gamma\,DC^e V_m^2\,t}{9RT} \qquad (56)$$

where

$\bar{r}_0$ = mean radius at $t = 0$

D = diffusivity of solute in the matrix, in m^2/s

C^e = equilibrium solubility of bulk particle phase in the matrix in mol/m^3

t = time, sec.

The other variables were defined earlier. The coefficient of t in Eq. (2) may be defined as a coarsening rate constant, K.

$$\bar{r}^3 - \bar{r}_0^3 = Kt \qquad (57)$$

Inserting typical values for γ, V_m, and T gives:

57

$$K \cong 4 \times 10^{-15} \, DC^e \, m^3/s \tag{58}$$

We note here that in volume diffusion controlled coarsening, $\bar{r}^3 \alpha t$, whereas for growth, $\bar{r}^2 \alpha t$. Coarsening is thus a much slower process. Equation (56) has been tested in a number of alloy systems and found generally valid, though some details are yet in question (71).

Equation (56) for elemental precipitates was modified by Bhattacharyya and Russell (74) to describe compound dispersoid AB particles which add or lose A and B atoms only in stoichiometric proportions. The dependence of solubility on particle size is given by:

$$C_A^r C_B^r = C_A^e C_B^e \left(\frac{2\gamma V_m}{rRt} \right) \tag{59}$$

where the equilibrium solubility product is given by

$$C_A^e C_B^e \, \alpha \, \exp(\Delta H_{net}/kT) \tag{60}$$

with

C_A^e, C_B^e = matrix concentrations of A and B in equilibrium with bulk AB
ΔH_{net} is defined by Eq. (54).
C_A^r, C_B^r = concentrations of A and B in equilibrium with an AB particle of radius, r.

It is important to note that in both solubility products, one concentration may be set arbitrarily, but then the other is fixed by the requirement of a constant product.

Bhattacharyya and Russell (74) showed that transport of one component would usually be much more difficult than the other; the harder to transport, or rate controlling component would then have a concentration gradient as shown in Figure 28. The matrix concentration of the other species would then be constant right up to the particle:matrix interface. The coarsening equation for AB particles in M then becomes:

$$\bar{r}^3 - \bar{r}_o^3 = \frac{8 < DC > \gamma V_m^2 t}{9RT} \tag{61}$$

where

$$<DC> = \frac{D_A C_A^e D_B C_B^e}{D_A C_A^e + D_B C_B^e} \tag{62}$$

58

The quantity $<DC>$ is equal to the smaller of $D_A C_A^e$ and $D_B C_B^e$, except for rare cases where the two are nearly equal.* In most cases the matrix concentrations of A and B are not in stoichiometric proportion. The matrix concentration of the more abundant element (say A) fixes C_A^e, and the solubility product fixes C_B^e. The coarsening law for compound particles thus differs significantly from the elemental case in a different choice for diffusion coefficient and solubility.

Eq. 61 may be used to select an optimum dispersoid for stability against volume diffusion controlled coarsening. First, ΔH_{net} should be as negative as possible, to minimize solubility. Either A or B, or preferably both should be slow diffusers in the matrix. Then the coarsening rate in the system is minimized (at a given temperature) by adding a large excess of the faster diffusing element (say A). This excess A greatly depresses the concentration of the slower diffusing B atoms and gives the lowest possible value of $<DC>$ and thereby of the coarsening rate.

B. Short Circuit Diffusion Control

Particles may be located on grain boundaries or dislocation lines, both of which are usually high diffusivity paths. Diffusive processes, including coarsening, may then occur at an accelerated rate by taking place in the high diffusivity region. Figure 29 shows a particle of radius, r, located on a grain boundary of thickness, δ, where δ is the order of the lattice spacing. Mass transport along the grain boundary gives solute addition only on a belt of thickness, δ, around the particle equator.
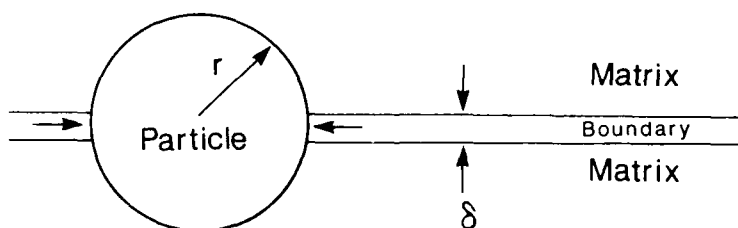
Figure 29   Representation of growth of a particle by diffusion of solute along a grain boundary of thickness, δ.

Speight (75) derived an equation for coarsening of particles on grain boundaries. His expression depended on particle shape and volume fraction of the particulate phase, but for the present case of spherical or near spherical particles present at 1-10 vol %, the equation reduces to

---

* Eq. (62) is modified by factors not far from unity for compounds which are not 1:1 in A and B. Eqs. (61,62) are adequate for describing any but the most precise experiments.

$$\bar{r}^4 - \bar{r}_0^4 \approx \frac{D_b \delta C_b \gamma}{RT} V_m^2 t \tag{63}$$

where D_b = diffusivity in the grain boundary and C_b = particle solubility in the grain boundary.

Thus, $\bar{r}^4$ is proportional to t for grain boundary coarsening. Kirchner (76) and Ardell (77) later derived similar but more complicated expressions for grain boundary coarsening of elemental precipitates.

Equation (63) may be modified by the method of Bhattacharyya and Russell (74) to describe coarsening of compound precipitates on grain boundaries to give

$$\bar{r}^4 - \bar{r}_0^4 = \frac{<D_b\, C_b>\delta\gamma V_m^2 t}{RT} \tag{64}$$

where $<D_bC_b>$ is given by a relationship equivalent to Eq. 62, except written in terms of boundary concentrations and diffusivities.

We may now compare the rates of coarsening by volume diffusion and by boundary diffusion to see which is more rapid and will therefore dominate. Differentiating Eqs. (61,64) with respect to time gives two expressions for the rate of average particle growth by the two diffusion mechanisms. Equating the two growth rates gives

$$\bar{r} = \delta\frac{<D_b\, C_b>}{<D\, C>} \tag{65}$$

as the crossover radius where the two rates are equal. Boundary diffusion will control the coarsening rate at smaller particle sizes and volume diffusion at larger. Boundary diffusion controls at small sizes because solute can add onto a larger fraction of the particle surface.

Figure 30 plots Eq. (65) with the assumption that $\delta = 3 \cdot 10^{-10}$m. Boundary diffusion will dominate for 30-nm particles if

$$\frac{<D_b\, C_b>}{<D\, C>} \gtrsim 10^2,$$
and for 3-μm particles if

$$\frac{<D_b\, C_b>}{<D\, C>} \gtrsim 10^4$$

Such ratios should certainly obtain at processing or service temperature of ca. $T_m/2$ or below. We show in Section II that for substitutional solutes at $T_m/2$ where D is the order of 10^{-20} m^2/s, very roughly $D_b \approx 10^{-12}$ m^2/s. The ratio
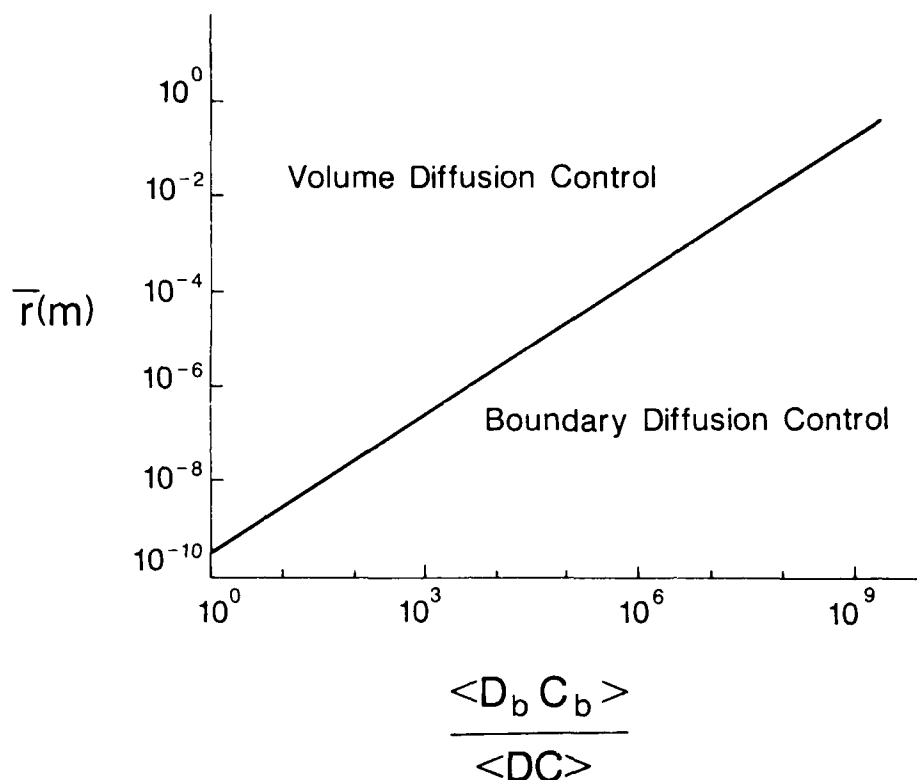
Figure 30   Plot showing the conditions of particle radius, diffusivity, and concentration giving volume diffusion control vs boundary diffusion control.

$$\frac{< D_b \ C_b >}{D \ C} \gtrsim 10^8$$

even if $C_b = C$. Since in most cases $C_b > C$ or $C_b \gg C$ (see Section II), particles on boundaries should undergo accelerated coarsening unless they are very large. Even near the melting point $D_b/D \approx 10^4$, so that submicron particles on grain boundaries would undergo accelerated coarsening even near T_m.

Diffusion may also be accelerated by enhanced diffusion along dislocation lines, which may, in turn, alter coarsening in two different ways. In the first case, atoms move many times between dislocation and matrix, and the diffusion coefficient is the weighted average of the two (78).

The result of Hart (78) may be written as

$$D = D_v + A_p \rho_p D_p$$

61

where D is the operative diffusion coefficient. Here

D_v = volume diffusion coefficient

D_p = diffusivity in pipe

P_p = dislocation density, m/m^3

A_p = area of dislocation pipe.

The dislocation lines will accelerate coarsening if

$$D_p/D_v > \frac{1}{A_p P_p}$$

An annealed material will have $P_p \approx 10^{10}/m^2$ and a cold worked material will have $P_p \approx 10^{14}/m^2$. The high diffusivity path should be a few atoms in cross section, giving $A_p \approx 10^{-19}m^2$, so that pipe diffusion will enhance coarsening in annealed material if $D_p/D_v > 10^9$ and in cold worked material if $D_p/D_v > 10^5$. Section II shows that typically $D_p/D_v \approx 10^8$ at $T_m/2$ and $D_p/D_v \approx 10^4$ at T_m. Therefore, a high dislocation density, as might exist during such a thermomechanical treatment as extrusion, could give greatly enhanced coarsening even at temperatures above half the absolute melting point. Movement of dislocations as occurs during extrusion greatly facilitates meeting the requirement that the atoms move many times between dislocation and matrix. The dislocations in annealed material, on the other hand, probably would give appreciably enhanced coarsening only at temperatures well below $T_m/2$.

Coarsening may also be accelerated by diffusion down dislocation lines which intersect the particle surface. However, the concentration of solute in the dislocation cores will usually be very small so that solute exchange with the matrix would be needed for appreciable coarsening. Solute would then diffuse from the surrounding matrix into the dislocation, then diffuse rapidly along the dislocation to a growing particle. The reverse process would occur for a shrinking particle. This "collector line" mechanism is analogous to the "collector plate" mechanism postulated by Aaron and Aaronson (79) for growth or dissolution of particles located on grain boundaries. The needed analysis has not yet been done to permit calculation of coarsening rates by the collector line mechanism.

4. DRAGGING BY GRAIN BOUNDARIES

Dispersoid particles are sometimes observed on only one side of grain boundaries after grain boundary migration during high temperature deformation (80). Such denuded zones suggest that particles were dragged along by the moving grain boundaries during deformation. Such dragging would be deleterious to the material properties as the boundary would sweep up particles, which could then undergo accelerated coarsening due to boundary diffusion. The denuded zone would also constitute a weakened region in the material.

Several authors have analyzed particle dragging. Shewmon (81) derived an expression for the migration rate of bubbles in a temperature gradient. Ashby and Palmer (82) and Koch and Aust (83) discussed early observations of particle dragging by migrating grain boundaries. Ashby and Centamore (84) made an experimental and theoretical study of the dragging of small oxide particles by migrating grain boundaries in copper. Noncrystalline oxides (B_2O_3, GeO_2, SiO_2) moved by viscous flow of the particle. Crystalline Al_2O_3 did not move; Ashby and Centamore concluded that diffusion through the particle was needed to give migration. Diffusion in Al_2O_3 is extremely slow even at the melting point of copper, so the particles could not be expected to move by that mechanism. The solubility of Al_2O_3 in Cu is probably too low to give migration by Al_2O_3 dissolution from the back of the particle and re-precipitation at the front. Ashby and Centamore noted that Al_2O_3 was partly coherent with the Cu matrix. The presence of such coherency is presumably the reason why they did not consider the possibility of migration of the particle by diffusion of copper from in front of the particle to the rear. Noncrystalline particles could move by such matrix diffusion, but crystalline particles almost always have some coherency with a crystalline matrix (85). Such coherency would almost always preclude sliding at the particle:matrix interface and thereby prevent particle movement by atom-by-atom migration of the matrix material.

This report is concerned with dragging of crystalline dispersoid particles which certainly have some coherency with the matrix. Our concern is therefore with particle migration by dissolution of material from the rear of the particle, diffusion through the particle:matrix interface, and deposition onto the particle front. Ashby (86) calculated the velocity for the simpler case of dragging a pure, one-component particle by a migrating boundary by such dissolution, boundary diffusion, and reprecipitation.

Pulling the grain boundary from the particle equator to the south pole (see Figure 31) involves creation of grain boundary energy. The grain boundary initially had a "hole" of area πr^2; pulling the boundary to the particle south pole requires filling this hole with grain boundary of energy $\Delta G = 4\pi r^2 \gamma_b$, where γ_b is grain boundary energy.

Creation of the boundary energy causes the boundary to exert a force on the particle; atoms in the particle may respond to this force by diffusing from the back and sides of the particle to the front. Diffusion could be either through the matrix, the particle, or the interface; the last path is considered more probable due to much higher diffusivities.

The free energy difference may be converted in a straightforward way to a solubility difference between rear and front of:

$$\Delta C_b = C_b^e \cdot \frac{3\gamma_b V_m}{2rRT} \tag{68}$$

where C_b^e = equilibrium solubility in the interface given by the solubility product and the other terms were defined earlier.
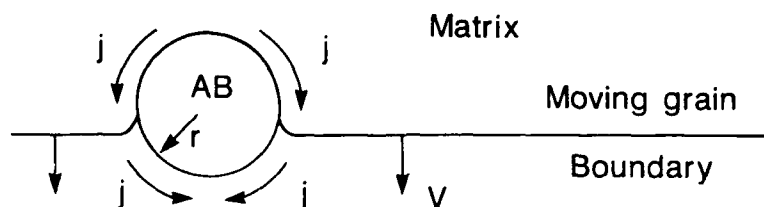
Figure 31   Representation of particle dragging by a moving grain boundary. The particle moves by dissolution of material from the rear, which diffuses along the interface and reprecipitates on the front.

The flux in the interface is

$$J = -D_b \frac{\Delta C_b}{\Delta x} = \frac{D_b \Delta C_b}{\pi r}$$

where the concentration gradient has been linearized over the πr path length between poles. The rate of mass transport is $\dot{q}= J\cdot A$ where $A = 2\pi r \delta$ represents the cross-sectional area of interface through which mass transport occurs. Then:

$$\dot{q} = \frac{3\gamma V_m \delta <D_b C_b>}{rRT} \text{mol/sec.}$$

Dividing $\dot{q}$ by the number of mols/particle gives the rate at which the particle translates one diameter, and multiplying by the diameter gives the particle velocity (87):

$$V_{max} = \frac{9\gamma <D_b C_b> V_m^2 \delta}{2\pi r^3 RT} \text{m/s} \tag{69}$$

Eq. (69) is the desired equation: if simplified to describe the elemental case by setting $C_b V_m = 1$, it and Ashby's equation differ by the trivial factor of $9/2\pi$.

V_{max} is the maximum velocity the particle can maintain while being dragged by a grain boundary. As $V_{gb} \rightarrow V_{max}$, the boundary will be on the verge of breaking away from the particle. For $V_{gb} > V_{max}$ the particle must be left behind. For $V_{gb} << V_{max}$, the grain boundary will be near the particle equator and the particle can follow easily at a very low driving force.

The boundary diffusivity, D_b, is expected to be the order of 10^{-12} m²/s at $T_m/2$ (see Section II). The particle solubility in the interface is not well known, and could even be hard to define. However, an upper limit to C_b^e is the concentration in the particle itself,

approximately 10^5 mol/m³. Figure 32 is a plot of Eq. (69) with $D_b = 10^{-12}$m²/s and C_b^e of 10^5 mol/m³, 10^2 mol/m³, and 0.1 mol/m³ as representative of high, intermediate, and low solubilities, respectively, and typical values for V_m, T, and γ. The plot gives the upper limits for the rate at which a crystalline particle may be dragged at $T_m/2$ when migration is by boundary diffusion of substitutional solute.

Figure 32 shows that a maximum dragging velocity of 1 μm/hr is possible for 1, 10, and 100 nm radius particles of low, intermediate, and high solubility, respectively. Such a migration rate should give observable boundary dragging of particles during thermomechanical treatment. The low and intermediate solubilities should roughly bracket the solubilities of most dispersoid particles at $T_m/2$.
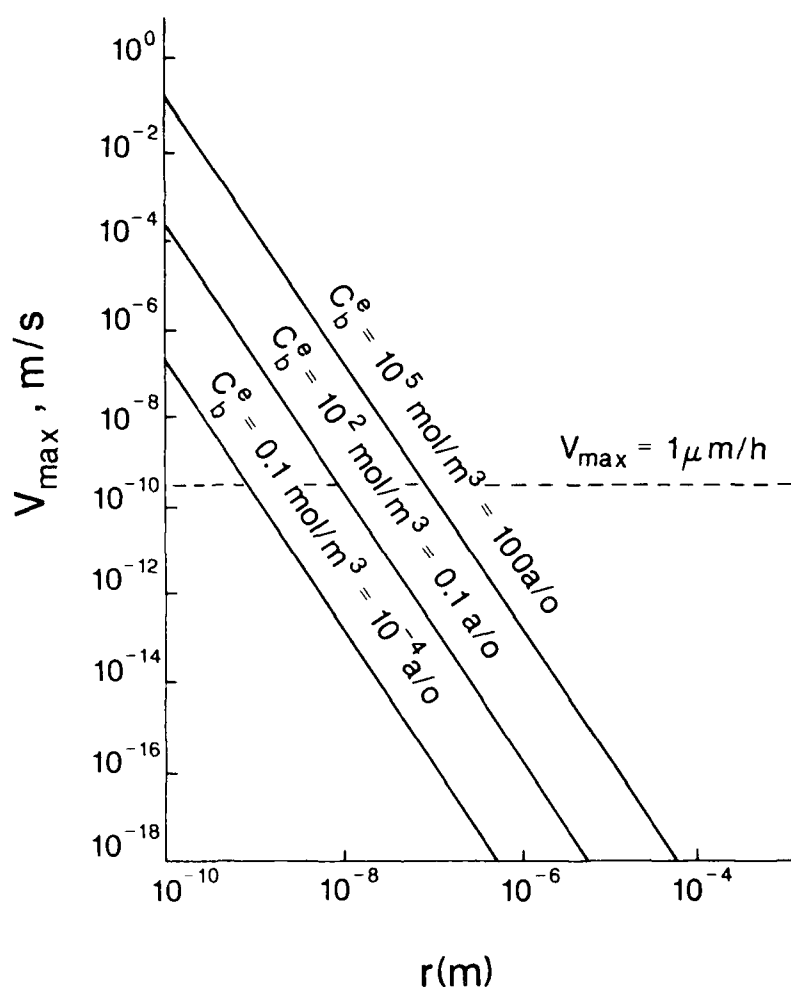

Figure 32   Plot of maximum dragging velocity vs particle size for several particle solubilities. A temperature of $T_m/2$ is assumed.

65

5. COMPARISON OF THEORY WITH EXPERIMENT

We here compare the theoretical predictions of this section with experimental studies on grain size limitation and on particle coarsening and dragging.

Froes, et al (88) recently studied grain growth in Ti-6Al-4V samples produced by blending of the powdered elements (BE) and in conventional wrought plate. The plate had an initial grain size of 4.7μm compared to 9.5μm for the BE material. Annealing at 1,310K (1,900F) or 1,477K (2,200F) gave very extensive grain growth in the plate while the grain size in the BE material remained unchanged.

The major microstructural difference in the starting materials was 1 vol.% of approximately 0.5μm diameter pores in the BE stock. The spread in grain size in the BE stock was very small, giving $\alpha \approx 1.1$. Eq. (52) predicts a limiting grain size to pore diameter ratio of $D_m / D_p = 13$, compared to the measured $D_m / D_p = 20$, which is certainly satisfactory agreement. However, since no grain growth occurred in the BE material, the pore dispersion might have been capable of stabilizing an even finer grain size. All we may in fact conclude is that experimentally $D_m / D_p \leq 20$. The actual value could be determined by experiments with finer grained material or material with a larger spread in grain size.

A number of authors have studied particle coarsening and dragging. Here we restrict ourselves to studies involving α - Ti based and Ti_3Al based alloys because these systems are of particular current interest. Table 2 summarizes the coarsening measurements from a number of investigations. The experiments were conducted in several ways: Whang, et al (89,90) and Konitzer and Fraser (91) studied coarsening in heat treated foils, whereas Rowe, Sutliff and Koch (92, 93) and Sutliff and Rowe (94) studied coarsening which occurred during extrusion or hot isostatic pressing. Coarsening in the foils should be controlled by volume diffusion. The other studies involve grain boundary migration and creation of dislocations, so the particles could exhibit enhanced coarsening rates by grain boundary and dislocation pipe diffusion.

Figure 33 shows a microstructure produced by HIP, extrusion, and aging. Denuded zones and enhanced coarsening of particles on grain boundaries are clearly visible. Whang (90) studied the coarsening of Ti_5Si_3 particles in a Ti-Al-Si matrix and of La_2Sn particles in a Ti-Sn-La matrix. The La_2Sn particles were extremely small, with diameters in the 10 nm range, and the Ti_5Si_3 particles were about 10 times larger. A $\bar{r}^3 \alpha t$ relationship was found in both cases, which in the absence of a high dislocation density indicated matrix diffusion controlled coarsening. The 2.1×10^{-27} m^3/s constant for coarsening Ti_5Si_3 at 973K (1,292F) corresponds to $C \approx 0.5$ mol/m^3, or about 0.5×10^{-3} at. %, which is reasonable for sparingly soluble dispersoid particles.

Whang found that at 1,073K (1,472F), La_2Sn coarsened much slower than did Ti_5Si_3. The rate constant was approximately 300 times smaller, so that $<DC>$ for La_2Sn is 1/300 that for Ti_5Si_3. Whang, Lu, and Giessen (96) had estimated from coarsening data that the Si diffusion coefficient in α -Ti was about an order of magnitude higher than the self diffusion coefficient in α -Ti. Whang attributed the high coarsening rate to this high

66

Table 2 Thermal Stability Ti and Ti3Aℓ Based Alloys

Alloy	Phase	T,K(F)	K(m³/s)	Comment	Reference
Ti-5Aℓ-2Si	Ti5Si3	973 (1292)	2.1×10^{-27}	Study of Heat-Treated Foils	(90)
Ti-5Aℓ-2Si	Ti5Si3	1073 (1472)	3.4×10^{-26}	Study of Heat-Treated Foils	(90)
Ti-5Sn-4.5La	La2Sn	1073 (1472)	9.4×10^{-29}	Study of Heat-Treated Foils	(90)
Ti3Aℓ-.4Er-.2O	Er2O3	1073 (1472) 1173 (1652)	$< 2 \times 10^{-29}$	Study of Heat-Treated Foils	(91)
Ti3Aℓ-.4Er-.2O	Er2O3	1273 (1832)	2×10^{-28}	Study of Heat-Treated Foils	(91)
Ti-Er-O	Er2O3	1173 (1652)	Coarsens	Study of Heat-Treated Foils	(91)
Ti3Aℓ-Nb-Er-O	Er2O3	1173 (1652)	$< 2 \times 10^{-29}$	Little coarsening during HIP	(94)
Ti3Aℓ-Nb-Er-O	Er2O3	1143 (1598)		Heavy coarsening during extrusion	(94)
Ti3Aℓ-Er-O, Ti3Aℓ-Nb-Er	Er2O3	1123 (1562)		Severe coarsening on G.B. during HIP	(93)
Ti3Aℓ-Er-O, Ti3Aℓ-Nb-Er	Er2O3	1198 (1692)	10^{-20}	Very severe coarsening during extrusion	(93)
Ti3Aℓ-Ce-S, Ti3Aℓ-Nb-Ce-S	Ce2S3 + Ce4O4S3	1198 (1692)		Limited grain boundary coarsening during HIP	(93)
Ti3Aℓ-Ce-S, Ti3Aℓ-Nb-Ce-S	Ce2S3 + Ce4O4S3	1200 (1701)		Little coarsening, some particle dragging during extrusion	(93)
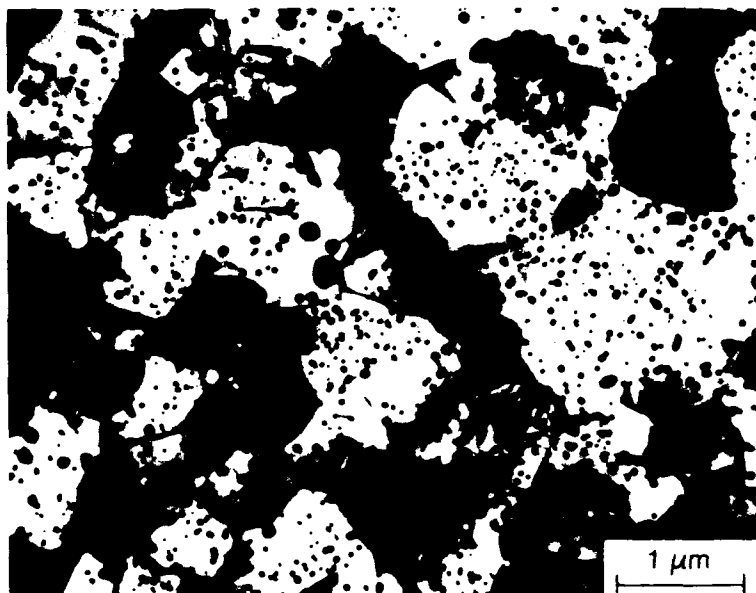
Figure 33   Denuded zones and enhanced coarsening of particles on a
grain boundary in melt extracted Ti-8.9 Al-1Sn - 1.5 Zr-1 Er
(a/o) after HIP and extrusion at 1,113K (1,545F) and aging at
1,023K (1,382 F) for 2 hours. (Figure from Ref. (95)).

Si diffusivity. However, at 1,073K La_2Sn has a 300 times lower coarsening rate than does Ti_5Si_3. Unless La and Sn are anomalously slow diffusers in α-Ti, it is more likely that the decreased coarsening rate is due in large part to La_2Sn being less soluble than Ti_5Si_3. This disagreement could be settled by obtaining values for heats of formation of Ti_5Si_3 and La_2Sn and for heats of solution of Si, La, and Sn in α-Ti and calculating the appropriate solubility products.

The remainder of the coarsening studies are of a more approximate nature wherein the authors usually only state whether coarsening occurred not at all, moderately, or to a large extent. Konitzer and Fraser (91) observed that a distribution of ~10 nm radius Er_2O_3 particles in a Ti_3Al matrix did not coarsen in 10 hr at 1,073K (1,472F) or 1,173K (1,652F). Appreciable coarsening did occur in 10 hr at 1,273K (1,832F), with $\bar{r}$ going from about 10 nm to 50 nm.

"No coarsening" may be interpreted roughly as less than ~20% increase in the initial 10 nm particle radius in the 10-hr heat treatment or a coarsening constant of $K \lesssim 2 \times 10^{-29}$ m^3/s. Coarsening of the Er_2O_3 particles from 10 nm to 29 nm radius in 10 hr at 1,273K (1,832F) (just above the β transus) indicates a coarsening rate constant of about 2×10^{-28}

m^3/s. Most solutes diffuse faster in β-Ti than in α-Ti, so the particles would tend to coarsen faster above the β-transus than below.

Sutliff and Rowe (94) studied alloys of Ti_3Al and 0.5 at. % Er to which additions of 0,5,6 and 7.5 at. % Nb had been made. Ribbons were melt-spun and aged and consolidated by hot isostatically pressing (HIP) and HIP plus extrusion. The as-spun ribbons contained a fine dispersion of 20-40 nm Er_2O_3 particles. Aging of the ribbons for 1 hr at 1,023K (1,382F) resulted in further Er_2O_3 precipitation, with particles 5-20 nm in diameter. Particles in the grain interior did not coarsen during aging of the 5 at. % Nb ribbons at 1,173K (1,652F) for 1 hr. This stability at 1,173K (1,652F) is consistent with the results of Konitzer and Fraser (91). Particles at or near the grain boundaries coarsened, and a particle-depleted zone was observed. Figure 33 shows an example of such depleted zones and enhanced coarsening at grain boundaries. This observation is consistent with enhanced coarsening by grain boundary diffusion, as discussed earlier. The denuded zones are probably due to large particles on the grain boundary consuming smaller, less stable particles in the matrix. Grain boundary dragging of particles is unlikely to have been a factor during the purely thermal anneal.

HIP at 1,173K (1,652F) did not give particle coarsening, so the coarsening constant is less than about 2×10^{-29} m^3/s, consistent with the results of Konitzer and Fraser (91). Alloys HIP at 1,123K (1,562F) and extruded at 1,143K (1,598F) showed marked coarsening. Most particles were located near grain boundaries, and the average particle size was 500 nm. Extrusion at 1,198K (1,698F) gave even heavier coarsening. Niobium content did not affect coarsening during extrusion.

Analyzing the coarsening data obtained for 1,143K (1,598F) extrusion on the basis of volume diffusion control gives $K \approx 10^{-20}$ m^3/s, a value some nine orders of magnitude greater than determined during thermal annealing on material HIP at 1,173K (1,652F), a 30K (54F) higher temperature.

Rowe, Sutliff, and Koch (92, 93) studied the coarsening of dispersoids in Ti_3Al based alloys to which 0,5,6,7.5 and 10.5 at. % Nb had been added. Erbium was added to some of the alloys to produce an Er_2O_3 dispersoid while in others cerium and sulfur additions produced a dispersoid of Ce_2S_3 and possibly $Ce_4O_4S_3$ particles. The alloys were solidified by melt spinning; the as-spun Nb-bearing alloys had the β_2 ordered BCC structure, whereas the Ti_3Al was α_2, ordered HCP. The as-spun ribbons contained 10-50 nm diameter particles; aging for 1 hr at 1,023K (1,382F) produced a second distribution of particles one third to one fifth this size.

HIP of the alloys at 1,123K (1,562F) gave severe coarsening of the Er_2O_3 particles located on or near grain boundaries. Addition of niobium diminished the degree of particle coarsening. Some grain boundaries showed dispersoid coarsening on one side but not the other, an effect attributed to boundary dragging. The Er_2O_3 particles in the study were less than 50 nm diameter, and according to Eq. (69) could be dragged by moving grain boundaries.

Extrusion of the HIP alloys at temperatures near 1,198K (1,692F) caused severe coarsening to an average Er_2O_3 particle diameter approaching 0.5 µm. Such heavy coarsening during the brief extrusion implies a coarsening constant of $K \approx 10^{-20}$ m³/s. Clearly something occurred during extrusion which promoted coarsening so powerfully as to overcome the higher temperatures and longer times of coarsening during HIP. The pressures exerted during HIP are not high enough to significantly retard diffusion. The authors suggested that adiabatic heating may have heated the alloy above the estimated extrusion temperature. The coarsening rate increases rapidly with temperature (Eq. 61), so a temperature excursion could give greatly increased coarsening. However, a simple energy balance shows that a 100 MPa (15,000 psi) extrusion pressure could give at most a 50K (90F) temperature rise. The associated ca. five fold increase in volume diffusion coefficient would be significant, but the temperature increase would last only a few seconds so little extra coarsening would occur. A higher extrusion pressure, say 1 GPa (150,000 psi) could give a 500K (900F) temperature increase and a ca. 10^5 increase in diffusivity. Such adiabatic heating could sharply increase the degree of coarsening. However, the presence of almost all the particles on grain boundaries indicates that the enhanced coarsening is due to a combination of grain boundary dragging and boundary diffusion enhanced coarsening. An extrusion temperature of 1,143K (1,598F) corresponds to 0.64 T_m, so that grain boundary dragging of the particles is certainly possible.

The Ce_2S_3 dispersoid showed much less coarsening than did the Er_2O_3, under identical HIP and extrusion conditions. HIP of the Ce_2S_3-bearing alloys at 1,173K (1,652F) gave only limited grain boundary coarsening. Extrusion of the Ce_2S_3 bearing alloys at about 1,198K (1,692F) gave little coarsening, though there was evidence of a small amount of particle dragging by grain boundaries.

Rowe, et al (92,93) gave the following qualitative interpretation of their results, which is generally consistent with the more quantitative treatment in this section. The presence of denuded regions and large particles near grain boundaries were attributed to particle dragging and to coarsening enhanced by boundary diffusion. The coarsening resistance of the Ce_2S_3 as compared to Er_2O_3 was attributed not to a more negative enthalpy of formation of the Ce_2S_3, but to oxygen having a more negative heat of solution in Ti_3Al than does sulfur. The very negative heat of solution of oxygen leads to easy dissolution of Er_2O_3, and thereby a high solubility and rapid coarsening.

Niobium additions were found to strongly suppress Er_2O_3 coarsening in the grain boundary. Rowe, et al attributed this effect to either a decreased diffusivity or interfacial energy. The former is far more likely. Addition of Nb could easily give a large decrease in diffusivity or in solubility, either of which would strongly suppress coarsening. A greater than about 50% decrease in interfacial energy is most unlikely, and even a 50% reduction would have only a modest effect on the coarsening rate.

SECTION VI

CONCLUSIONS

1. TSSE in Al-based alloys is predicted well by the Miedema crystal chemistry coordinates.

2. A theory was developed for coarsening and dragging of compound precipitates and found to agree with experiment.

3. A theory was developed which predicts that a fine grain size in RS alloys is obtained by solute additions which sharply depress T_0. Good agreement with most experimental results was found.

4. Conditions for forming a high number density of fine dispersoid particles conflict with conditions for thermal stability.

5. Ancillary data needed for the calculation of nucleation, growth, and coarsening rates may be calculated from the Miedema macroscopic atom model.

SECTION VII

REFERENCES

1. Proc. Second Bolton Landing Conference on Oxide Dispersion Strengthening, G. S. Ansell, Editor, Gordon & Breach, New York, 1968.

2. F. Hehmann and H. Jones, "The Status and Potential of Rapid Solidification of Magnesium Alloys," Rapidly Solidified Materials and Their Mechanical and Magnetic Properties, Editors, B.C. Giessen, D.E. Polk, and A.I. Taub, Materials Research Society, Pittsburgh, Pa.,1986, p. 259-274.

3. H. Jones, Rapid Solidification of Metals and Alloys, The Institution of Metallurgists, London, 1982.

4. F. H. Froes, Y.-W. Kim and F..J. Hehmann, "Rapid Solidification of Al, Mg, and Ti," Journal of Metals, Vol. 39, No. 8, 1987, pp. 14-21.

5. H. Jones, "Some Aspects of the Rapid Solidification of Light Alloys," in Rapidly Solidified Metastable Materials, Editors, B.H. Kear and B. C. Giessen, North Holland, New York, 1984, pp. 303-315.

6. A.K. Sinha, Ferrous Physical Metallurgy, Butterworths, Boston, 1989, pp. 14-16.

7. P. G. Boswell and G.A. Chadwick, "The Grain Size of Splat-Quenched Alloys," Scripta Met., Vol 11, 1977, pp. 459-465.

8. R.E. Reed-Hill, Physical Metallurgy Principles, 2nd ed., D. Van Nostrand, New York, 1973, pp. 358-377.

9. J. W. Martin, Micromechanisms in Particle Hardened Alloys, Cambridge University Press, Cambridge, 1980.

10. S. Wolf and N. J. Grant, "Structure-Property Relationships in Oxide-Dispersed Iron-Beryllia Alloys," Powder Metallurgy International, Vol. 9, 1971, pp. 57-64.

11. M.A. Meyers and K.K. Chawla, Mechanical Metallurgy, Prentice-Hall, Inc., Englewood Cliffs, NJ, 1989, pp. 402-433.

12. A. R. Miedema, P.F. de Chatel, and F.R. de Boer, "Cohesion in Alloys-Fundamentals of a Semi-Empirical Model," Physica, Vol 100B, 1980, pp.1-28.

13. A. K..Niessen., F.R. de Boer, R. Boom, P.F. de Chatel, W.C.M. Matter A.R. Miedema, "Model Predictions for the Enthalpy of Formation of ..... .on Metal Alloys II," Calphad, Vol. 7, 1983, pp. 1-70.

14. A. R. Miedema, A. K. Niesen, and K. H. J. Buschow, "Some Notes on Diffusion in Alloys Containing Rare Earth Metals," Met., Vol. 100, 1984, pp. 71-84.

15. A. R. Miedema, "The Formation Enthalpy of Monovacancies in Metals and Intermetallic Compounds," Z. Metallk., Vol 70, 1979, pp. 345-353.

16. A. K. Niessen and F.R. de Boer, "The Enthalpy of Formation of Solid Borides, Carbides, Nitrides, Silicides, and Phosphides of Transition and Noble Metals," J. Less Comm.Met., Vol. 82, 1981, pp. 75-80.

17. F.R. de Boer, R. Boom, W.C.M. Mattens, A.R. Miedema, and A.K. Niessen, Cohesion in Metals: Transition Metal Alloys, North Holland, Amsterdam, 1988, xvi + 758pp.

18. R. A. Swalin, Thermodynamics of Solids, John Wiley & Sons, New York, 1967.

19. L. E. Murr, Interfacial Phenomena in Metals and Alloys, Addison-Wesley, Reading, Mass., 1975.

20. S. H. Overbury, P. A. Bertrand and G. A. Somorjai, "The Surface Composition of Binary System. Prediction of Surface Phase Diagram of Solid Solution," Chem Rev., Vol. 75, 1975, pp. 547-560.

21. J.R. Smith and A. Banerjia, "A New Approach to Calculation of Total Energies of Solids with Defects: Surface-Energy Anisotropies," Phys. Rec. Lett., Vol. 59, 1987, pp. 2451-2454.

22. A. S. Skapski, " A Theory of Surface Tension of Solid - I. Application to Metals," Acta Metall., Vol. 4, 1956, pp. 576-582.

23. N. D. Lang and W. Kohn, "Theory of Metal Surfaces: Charge Density and Surface Energy," Phys. Rev. B, Vol. 1, 1970, pp. 4555-4568.

24. W. R. Tyson, "Surface Energies of Solid Metals," Can. Met Quart., Vol. 14, 1975, pp. 307-314.

25. A. M. Stoneham, "Ceramic Surfaces: Theoretical Studies," J. Am. Ceram. Soc., Vol. 64, 1981, pp. 54-60.

26. A. R. Miedema and R. Boom, "Surface Tension and Electron Density of Pure Liquid Metals," Z. Metallk., Vol. 69, 1978, pp. 183-190.

27. E. Chacon, F. Flores and G. Navascues, "A Theory for Liquid Metal Surface Tension," J. Phys. F, Vol. 14, 1974, pp. 1587-1601.

28. G. E. Nash and M. E. Glicksman, "A General Method for Determining Solid-Liquid Interfacial Free Energies," Phil. Mag., Vol. 24, 1971, pp. 577-592.

29. R. H. Ewing, "The Free Energy of the Crystal-Melt Interface from the Radial Distribution Function," J. Crystal Growth, Vol. 11, 1971, pp. 221-224.

30. F. Spaepen and R. B. Meyer, "The Surface Tension in a Structural Model for the Solid-Liquid Interface," Scripta Met., Vol. 10, 1976, pp. 257-263.

31. Y. Waseda and W. A. Miller, "Calculation of the Crystal-Melt Interfacial Energy from the Experimental Radial Distribution Function Data," Trans. JIM, Vol. 19, 1978, pp. 546-552.

32.   A. R. Miedema and F. J. A. den Broeder, "On the Interfacial Energy in Solid-Liquid and Solid-Solid Metal Combinations," Z. Metallk., Vol 70, 1979, pp. 14-20.

33.   R. Warren, "Solid-Liquid Interfacial Energies in Binary and Pseudo-Binary Systems," J. Mat. Sci., Vol. 15, 1980, pp. 2489-2496.

34.   R. Tognato, "Some Considerations on the Interfacial Free Energy between Dislocation Core and Bulk Material at High Temperatures," Phys. Stat Sol., Vol. 82, 1984, pp. K17-K19.

35.   T. H. Faber, Introduction to the Theory of Liquid Metals, Cambridge University Press, Cambridge, 1972.

36.   J. Askill, Tracer Diffusion Data for Metals, Alloys, and Simple Oxides, ITF/Plenum, New York, 1970.

37.   A. M. Brown and M. F. Ashby, "Correlations for Diffusion Coefficients," Acta Metall., Vol. 28, 1980, pp. 1085-1101.

38.   E. D. Hondros, "Interfacial Energies and Composition in Solids," Precipitation Processes in Solids, Editors, K. C. Russell and H. I. Aaronson, Warrendale, PA, 1978, pp. 1-30.

39.   Smithells Metals Reference Book, 6th ed., Editor, E. A. Brandes, Butterworths, London, 1983.

40.   Handbook of Chemistry and Physics, 50th ed., Editor, R. C. Weast, The Chemical Rubber Co., Clevelend, Ohio, 1969.

41.   American Institute of Physics Handbook, D.E. Gray, Editor, McGraw-Hill, New York, 1963.

42.   J. C. Baker and J. W. Cahn, "Solute Trapping by Rapid Solidification," Acta Metall., Vol 17, 1969, pp. 575-578.

43.   T. R. Anantharaman, P. Ramachandrarao, C. Suryanarayana, S. Lele, and K. Chattopadhyay, "Structure and Constitution of Rapidly Solidified Aluminum Alloys," IIM Review No. 6, Trans. Indian Inst. of Metals,Vol. 30, No. 6, Dec. 1977, pp. 1-13.

44.   S. P. Midson and H. Jones, "On the Absolute Stability Criterion in Relation to Predicting Extension of Solid Solubility," Rapidly Quenched Metals, Editors, T. Masumoto and K. Suzuki, Japanese Institute of Metals, 1982, pp. 1539-1544.

45.   W. J. Boettinger, S.R. Coriell, and R.F. Sekerka, "Mechanisms of Microsegregation-free Solidification," Mats. Sci. & Eng., Vol 65, 1984, pp. 27-36.

46.   W. J. Boettinger, D. Shechtman, R.J. Schaefer, and F.S. Biancaniello, "The Effect of Rapid Solidification Velocity on the Microstructure of Ag-Cu Alloys," Metall. Trans., Vol. 15A, 1984, pp. 55-66.

47. J. A. Juarez-Islas. and H. Jones , "Conditions for Growth of Extended Al-Rich Al-Mn Alloy Solutions and Al-Al$_6$Mn Eutectic During Rapid Solidification," Acta Metall., Vol. 35, 1987, pp. 499-507.

48. K. H. J. Buschow, "Stability of Amorphous Alloys," Solid State Comm., Vol. 43, 1982, pp. 171-174.

49. L. Darken and R.W. Gurry, Physical Chemistry of Metals, McGraw-Hill, New York, 1952.

50. J. R. Chelikowsky, "Solid Solubilities in Divalent Alloys," Phys. Rev. B Vol. 19 1979, pp. 686-701.

51. Metals Handbook, Vol. 8, 8th Edition, American Society for Metals, Metals Park, OH, 1973, pp. xiv + 466.

52. M. Hansen, Constitution of Binary Alloys, McGraw-Hill, New York, 1958.

53. R. P. Elliott, Constitution of Binary Alloys, First Supplement, McGraw-Hill, New York, 1965.

54. F. A. Shunk, Constitution of Binary Alloys, Second Supplement, McGraw-Hill, New York 1969.

55. H. Jones, Aluminum, Vol 54, 1978, pp. 274-281.

56. J. L. Murray, "Thermodynamic Factors in the Extension of Solid Solubility in Al-Based Alloys," Alloy Phase Diagrams, Editors, L. H. Bennett, T. B. Massalski and B. C. Giessen, North Holland, New York, 1983, pp. 249-262.

57. H. Jones, "Extent of Solid Solubility in Magnesium and Aluminum," Mater. Sci. & Eng, 1983, Vol 57, pp. L5-L8.

58. D. R. Uhlmann, "A Kinetic Treatment of Glass Formation," J. Noncrystal. Solids, Vol. 7, 1972, pp. 337-348.

59. R. A. Grange and J.M. Kiefer, "Transformation of Austenite on Continuous Cooling and its Relation to Transformation at Constant Temperature," Trans. ASM, Vol 29, 1941, pp. 85-116.

60. P. Ramachandrarao, M.G. Scott and G. Chadwick, Phil Mag. Vol. 25, 1972, p. 961.

61. H. Jones, "Splat Cooling and Metastable Phases," Rep. Prog. Phys. Vol. 36, 1973, pp. 1425-1497.

62. T. F. Broderick, A. G. Jackson, H. Jones and F. H. Froes, "The Effect of Cooling Conditions on the Microstructure of Rapidly Solidified Ti-6Al-4V," Metall. Trans., Vol. 16A, 1985, pp. 1951-1959.

63. T. F. Broderick, F.H. Froes and A.G. Jackson, "Cooling Rate Effects on Ti-6Al-4V and Beta III Titanium Alloys," Mat. Res. Soc. Symp. Proc., Vol. 28, Elsevier Science Pubs, 1984, pp. 345-351.

64. S. Krishnamurthy, R. G. Vogt, D. Eylon and F.H. Froes, "Microstructures of Rapidly Solidified Titanium-Eutectoid Former Alloys," Mat Res. Soc. Symp. Proc., Vol. 28, Elsevier Science Pubs., New York, 1984, pp. 361-366.

65. W. A. Baeslack, III, L. Weeter, S. Krishnamurthy and P. Smith, "Rapidly Solidified Microstructures in a Ti-22 wt% Fe Alloy," Mat. Res. Symp. Proc., Vol. 28, Elsevier Science Pubs., New York, 1984, pp. 375-379.

66. R. Smallman, Modern Physical Metallurgy, 4th ed., Butterworths, London, 1985, p. 374.

67. M. Hillert, "On the Theory of Normal and Abnormal Grain Growth," Acta. Metall., Vol.13, 1965, pp. 227-238.

68. C. S. Smith, "Grains, Phases, and Interfaces: An Interpretation of Microstructure," Trans. Am. Inst. Min. Engrs., Vol. 175, 1948, pp. 15-51.

69. P. R. Rios, "A Theory for Grain Boundary Pinning by Particles," Acta Metall., Vol. 35, 1987, pp. 2805-2814.

70. S. J. Savage and F. H. Froes, "Production of Rapidly Solidified Metals and Alloys", Journal of Metals, Vol. 36, (No. 4), 1984, pp. 20-23.

71. M. Kahlweit, "Ostwald Ripening of Precipitates," Adv. Coll. Int. Sci., Vol. 5, 1975, pp. 1-35.

72. C. Wagner, "Theorie der Alterung von Niederschlagen durch Umlosen," Z. Elektrochem., Vol. 65, 1961, pp. 581-591.

73. I. M. Lifshitz, and V. V. Slyozov, "The Kinetics of Precipitation from Supersaturated Solid Solutions," J. Phys. Chem. Solids, Vol. 19, 1961, pp. 35-56.

74. S. K. Bhattacharyya and K. C. Russell, "Activation Energies for the Coarsening of Compound Precipitates," Met. Trans., Vol. 3, 1972, pp. 2195-2199.

75. M. V. Speight, "Growth Kinetics of Grain Boundary Precipitates," Acta Metall., Vol. 16, 1968, pp. 133-135.

76. H. O. K. Kirchner, "Coarsening of Grain Boundary Precipitates," Metall. Trans., Vol. 2, 1970, pp. 2861-2864.

77. A. J. Ardell, "On the Coarsening of Grain Boundary Precipitates," Acta Metall., Vol. 20, 1972, pp. 601-609.

78. E. Hart, "On the Role of Dislocations in Bulk Diffusion," Acta Metall, Vol. 5, 1957, p. 597.

79. H. B. Aaron and H. I. Aaronson, "Growth of Grain Boundary Precipitates in Al-4% Cu by Interfacial Diffusion," Acta Metall, Vol. 16, 1968, pp. 789-798.

80. F.. H. Froes and R. G. Rowe, Rapidly Solidified Titanium, in Rapidly Solidified Alloys and Their Mechanical and Magnetic Properties, Vol. 58, Editors, B. C. Giessen, D. E. Polk and A. I. Taub, Materials Research Society, Pittsburgh, PA, 1986, pp. 309-334.

81. P. G. Shewmon, "The Movement of Small Inclusions in Solids by a Temperature Gradient," Trans Met. Soc. AIME, Vol. 230, 1964, pp. 1134-1137.

82. M. F. Ashby and I. G. Palmer, "The Dragging of Solid Particles Through Metals by Migrating Grain Boundaries," Acta Metall., Vol. 15, 1968, pp. 420-423.

83. E. F. Koch and K. T. Aust, "The Movement of Solid Particles in a Solid," Acta Metall., Vol. 15, 1967, pp. 405-409.

84. M. F. Ashby and R. M. A. Centamore, "The Dragging of Small Oxide Particles by Migrating Grain Boundaries in Copper," Acta Metall., Vol. 16, 1968, pp. 1081-1092.

85. H. I. Aaronson and K. C. Russell, "Nucleation-Mostly Homogeneous and in Solids," Editors, H. I. Aaronson, D. E. Laughlin, R. F. Sekerka and C. M. Wayman, TMS-AIME, Warrendale, PA, 1983, pp. 371-397.

86. M. F. Ashby, "The Influence of Particles on Boundary Mobility," in Recrystallization and Grain Growth of Multiphase and Particle Containing Materials, Editors, N. Hansen, A. R. Jones, and T. Leffers, Risφ Laboratory, Roskilde, Denmark, 1978, pp. 325-336.

87. K. C. Russell and F. H. Froes, "Compound Dispersoid Stability on Grain Boundaries," Scripta Met., Vol. 22, 1988, pp. 495-499.

88. F. H. Froes, C. M. Cooke, D. Eylon and K. C. Russell, "Grain Growth in Blended Elemental Ti-6 Al-4V Powder Compacts," 1988, in Titanium, Science, Technology and Applications, Les Editions de Physique, 1988 (In press).

89. Y. Z. Lu, C.S. Chi, and S.H. Whang, "Second Phase Coarsening in Rapidly Solidified Ti-5Sn-4.5 La System," in Rapidly Solidified Metals, Editors, S. Steeb and H. Warlimont, Elsevier Science Publications, Amsterdam, 1985, pp. 950-952.

90. S. H. Whang, "Rapidly Solidified Ti Alloys for High Temperature Applications," J. Mat. Sci., Vol. 21, 1986, pp. 2224-2238.

91. D. G. Konitzer and H. L. Fraser, "The Production and Thermal Stability of a Refined Dispersion of Er_2O_3 in Ti_3Al Using Rapid Solidification Processing," Plasma Processing and Synthesis of Materials, Editors, J. Szekely and D. Apelian, Elsevier Publishing, New York, 1985, pp. 437-442.

92. R. G. Rowe, J. A. Sutliff and E. F. Koch, "Comparison of Melt Spun and Consolidated Ti_3Al-Nb Alloys With and Without a Dispersoid," Titanium Rapid Solidification Technology, Editors, F. H. Froes and D. Eylon, TMS-AIME, Warrendale, PA, 1986, pp. 239-248.

93. R. G. Rowe, J. A. Sutliff and E. F. Koch, "Dispersoid Modification of Ti_3Al-Nb Alloys," Rapidly Solidified Alloys and Their Mechanical and Magnetic Properties, Editors, B. C. Giessen, D. E. Polk and A. I. Taub, Materials Research Society, Pittsburgh, PA, 1986, pp. 359-364.

94.   J. A. Sutliff and R. G. Rowe, "Rare Earth Oxide Dispersoid Stability and Microstructural Effects in Rapidly Solidified Ti₃Al and Ti₃Al-Nb," _Rapidly Solidified Alloys and Their Mechanical and Magnetic Properties_, Editors, B. C. Giessen, D. E. Polk and A. I. Taub, Materials Research Society, Pittsburgh, PA, 1986, pp. 371-376.

95.   M. F. X. Gigliotti, R. G. Rowe, G. E. Wasielewski, G. K. Scarr and J. C. Williams, "Tensile and Creep Properties of Rapidly Solidified Titanium Alloys Containing Complex Matrices and Fine Dispersoids," _Rapidly Solidified Alloys and Their Mechanical and Magnetic Properties_, Vol. 58, Editors, B. C. Giessen, D. E. Polk and A. I. Taub, Materials Research Society, Pittsburgh, PA, 1986, pp. 343-351.

96.   S. H. Whang, Y. Z. Lu and B. C. Giessen, "Thermal Stability of Precipitates in a Rapidly Quenched Ti-Al-Si Alloy," _Rapidly Solidified Materials_, Editors, B. H. Kear and B. C. Giessen, Elsevier Publishing, New York, 1984, pp. 367-373.